



**POLITECNICO  
DI TORINO**

**Politecnico di Torino**

---

DIMEAS  
Aerospace Engineering

# **Multi-purpose rotor model for a real-time flight simulator**

Master Thesis

Candidate:  
**Simone Godio**

Thesis advisor:  
**Giorgio Guglieri**

Research supervisors:  
**Pierluigi Capone**  
**Federico Barra**

---

2019

# Acknowledgments

*A special thanks goes to Giorgio Guglieri, the advisor of this thesis, who distinguished himself for his great trust in me, providing on every occasion all the material and support necessary to do the work at best. I believe he gave a great contribution to this work, especially under a motivational point of view.*

*I also desire to thank my supervisors, Federico Barra, Pierluigi Capone and their staff, for the patience and dedication with which they supported me during my stay in Winterthur. They taught me much more than I could hope, and without them, the thesis wouldn't undoubtedly be the same.*

*A thought goes to the staff and services of the Politecnico di Torino, which allowed me to grow considerably not only in the educational aspect, but also in the human one.*

*I would also like to thank all my friends, in particular Lorenzo and Pietro, who always encouraged, supported and motivated me over the years. A special thought goes to Lodovico, Alessandro and Andrea; I am grateful to them for having always believed in my path and for the several study sessions faced together.*

*A special thanks goes to Francesca, my partner, for guiding and supporting me on this arduous journey along which she found in me the light that I could not find. If I was able to give the best of myself in these years and get great results, it is largely her merit.*

*Finally, a special thanks goes to all my relatives. To all my cousins, uncles and aunts who supported me in these years, to my grandparents, for their extreme experience and educational capacity and especially to my parents and brothers, who were always at my side rising me up in the darkest moments.*

## **Abstract**

In this thesis is analyzed a multi-purpose rotor model for a real time flight simulator. The discussion starts with writing the elementary aerodynamic forces acting on the single blade through the definition of each parameter involved. During the formulation of these elementary forces every speed contribution is considered, starting from the rotation induced speed, the flight speed, the aircraft's rotations induced speed, and the inflow. What is more, a third order taper and twist laws are adopted to make the most complete and realistic the model. In order to maintain an acceptable computational speed for the real-time application and to make the treatment as explicit and linear as possible the major part of mathematical passages are made in symbolic using the software Maple. The numerical integration of the forces and moments is realized with a numerical method in order to increase the efficiency of the code reducing the simulation time per frequency. Later, it is analyzed and solved the flapping equation of each blade, considering all the contributions of accelerations and moments acting on the hinge (Coriolis, rotational and translational speeds and accelerations, the hinge spring stiffness, the gravity force..). In this second order system's solution is also highlighted the results obtained with two different time integration methods, analyzing their limits, advantages and disadvantages. This dynamic, as it is solved for each blade, needs the introduction of two states for each one, that will be solved in the following treatment of the trim not developed in this thesis. Once solved the flapping dynamic, all the forces and moments acting on the hub of the rotor are evaluated, and subsequently the stress acting on the center of gravity of the aircraft are computed taking into account all the inertial contributions. In order to validate the model stress and flapping results, geometrical and physical data are taken from XV-15 tilt-rotor and UH-60 helicopter . For the inflow contribution the dynamic model proposed by Pitt Peter is adopted, and its formulation is proposed and explained later in this work. This model is built for a tilt-rotor flight simulator application, but it is shaped with the idea to be easily adaptable, in fact, just with changing different setting parameter it is possible to simulate other several typologies of rotors. Since a real time simulation model is already developed at the University of ZHAW (Winterthur, Switzerland), it was possible to incorporate the developed model into it and test its performance by means of flight simulator tests conducted by the institute in collaboration with pilots with hundreds hours of flight time behind them.

# Contents

<b>1</b>	<b>Introduction</b>	<b>15</b>
1.1	Rigid rotor . . . . .	16
1.2	Semi-Rigid rotor . . . . .	16
1.3	Articulated rotor . . . . .	17
1.4	Functions and machines . . . . .	18
1.4.1	XV-15 Tilt rotor . . . . .	18
1.4.2	UH-60 Blackhawk . . . . .	19
1.4.3	V-22 Osprey . . . . .	20
1.4.4	Dufour Aerospace tilt-wing concept . . . . .	21
1.4.5	Bell V-280 . . . . .	22
<b>2</b>	<b>Development of the mathematical model</b>	<b>23</b>
2.1	Assumptions . . . . .	24
2.2	References systems and rotating matrices . . . . .	26
2.3	Speeds and aerodynamic incidence . . . . .	28
2.4	Aerodynamic forces and moments . . . . .	31
2.5	Accelerations contributions . . . . .	34
2.6	Flapping dynamics solution . . . . .	35
2.7	Pitt/Peters Inflow Dynamics . . . . .	37
2.8	Projection and sum of loads . . . . .	40
2.9	Body-Hub moments transportation . . . . .	42
<b>3</b>	<b>Implementation of the Rotor Model</b>	<b>43</b>
3.1	Model structure and Time sequence . . . . .	43
3.2	Flapping dynamics implementation . . . . .	45
3.2.1	Forward Euler and Tustin methods . . . . .	46
3.2.2	Results and conclusions . . . . .	49
3.3	Aerodynamic implementation . . . . .	53
3.3.1	XV-15 Aerodynamics . . . . .	53
3.3.2	UH-60 Aerodynamics . . . . .	55
3.4	Tip loss and Mach correction Factors . . . . .	56
3.5	Multiblade trasformation . . . . .	58
3.5.1	Simulink® implementation . . . . .	59
3.5.2	Results . . . . .	60

<b>4</b>	<b>Results and Validation</b>	<b>62</b>
4.1	XV-15 test and validation . . . . .	62
4.1.1	Rotor inputs . . . . .	62
4.1.2	Results and validation . . . . .	63
4.1.3	XV-15 Rotor Efficiency . . . . .	69
4.2	XV-15's longitudinal cyclic response . . . . .	71
4.3	UH-60 test and validation . . . . .	78
4.3.1	Rotor inputs . . . . .	79
4.3.2	Equivalence of the scaled model . . . . .	80
4.3.3	Results and Validation in Hover . . . . .	82
4.4	UH-60 in Advanced Flight . . . . .	86
4.5	UH-60's longitudinal cyclic response . . . . .	88
4.6	XV-15 Flight simulator testing . . . . .	93
4.6.1	Introduction to the simulator . . . . .	93
4.7	XV-15 flight simulator test in helicopter mode . . . . .	95
4.7.1	Flight test time sequences . . . . .	95
4.7.2	First overview of results . . . . .	97
4.7.3	Take-off . . . . .	99
4.7.4	Hover condition . . . . .	100
4.7.5	Straight and level flight . . . . .	102
4.7.6	180-degree turn . . . . .	104
4.7.7	Lateral repositioning . . . . .	105
4.7.8	Longitudinal repositioning . . . . .	107
4.7.9	Landing . . . . .	109
<b>5</b>	<b>Conclusions, developments and applications</b>	<b>110</b>

# List of Figures

1.1	Leonardo da Vinci rotor sketch . . . . .	15
1.2	Rigid rotor model . . . . .	16
1.3	Robinson R-22 semi-rigid rotor . . . . .	17
1.4	UH-60 articulated rotor . . . . .	17
1.5	Bell/Boeing XV-15 prototype in helicopter mode . . . . .	18
1.6	UH-60 Blackhawk helicopter . . . . .	19
1.7	V-22 tilt-rotor . . . . .	20
1.8	Dufour Aerospace tilt-wing concept . . . . .	21
1.9	V-280 tilt-rotor . . . . .	22
2.1	Reference systems adopted . . . . .	26
2.2	V-22 $\phi_m$ nacelle angle . . . . .	27
2.3	V-22 $\beta_m$ nacelle angle . . . . .	27
2.4	Speed and forces acting on the blade element . . . . .	28
2.5	Trapezoids rule . . . . .	33
2.6	Simplified blade flapping sketch . . . . .	35
2.7	Flapping forcing contributions . . . . .	36
2.8	Disk rotor inflow sketch . . . . .	38
2.9	Hub-disk reference system transformation . . . . .	39
2.10	Forces and Moments on the single blade . . . . .	40
2.11	Body-Hub transformations . . . . .	42
3.1	Rotor Model resolution flowchart . . . . .	43
3.2	Rotor Model Simulink implementation . . . . .	44
3.3	Rotor Model and Conversions blocks . . . . .	45
3.4	Forward Euler scheme . . . . .	47
3.5	Franklin Powell Tustin' method implementation scheme (Ref. [8]) . . . . .	48
3.6	Simulink Tustin' implementation for the flapping dynamics . . . . .	48
3.7	1st comparison Tustin-Euler . . . . .	49
3.8	2nd comparison Tustin-Euler . . . . .	50
3.9	3rd comparison Tustin-Euler . . . . .	50
3.10	Forward Euler-Tustin $w_n$ and $\zeta$ comparison . . . . .	51
3.11	XV-15 Hover flapping dynamics ( $\Omega = 589rpm$ , Sea Level) . . . . .	52
3.12	NACA 64-208, XV-15 aerodynamic profile . . . . .	53
3.13	$C_l-\alpha$ NACA 64-208, XV-15 . . . . .	53
3.14	$C_d-\alpha$ NACA 64-208, XV-15 . . . . .	54
3.15	SC 1095, UH-60 aerodynamic profile . . . . .	55

3.16	$Cl_\alpha$ SC-1095, UH-60	55
3.17	$Cd_\alpha$ SC-1095, UH-60	56
3.18	Tip Loss Factor Law	57
3.19	$Cl_\alpha$ Mach correction factor	57
3.20	$Cd0$ correction factor	58
3.21	Multiblade tranformation Simulink® structure	59
3.22	Multiblade tranformation Simulink® structure detail	60
3.23	Multiblade tranformation coefficients	61
3.24	Multiblade tranformation comparison	61
4.1	XV-15 Blade twist	62
4.2	XV-15 rotor in Langley test center	63
4.3	XV-15 rotor $Cp$ - $Ct$ curve in Hover conditions	64
4.4	XV-15 $Ct$ -Collective curves in Hover conditions	65
4.5	XV-15 rotor $FM-\frac{Ct}{\sigma}$ curve in Hover conditions	66
4.6	Bell XV-15 in airplane mode	69
4.7	XV-15 rotor efficiencies	70
4.8	Tilt-rotors efficiencies	70
4.9	Turboprop efficiencies	71
4.10	XV-15 Hover	73
4.11	XV-15 in advanced flight $u_h = 30m/s$	74
4.12	XV-15 in advanced flight $u_h = 30m/s$ , 5deg of side-slip angle	75
4.13	XV-15 in advanced flight $u_h = 40m/s$	76
4.14	XV-15 in advanced flight $u_h = 50m/s$	77
4.15	UH-60 Black Hawk scaled rotor in Langley Wind Tunnel	78
4.16	UH-60 Blade twist law	79
4.17	Blade's simplified scheme	81
4.18	UH-60 $Ct$ -Collective curve	82
4.19	UH-60 $Cp$ - $Ct$ curve	83
4.20	UH-60 $FM-\frac{Ct}{\sigma}$ curve	83
4.21	UH-60 $Ct$ -Collective TDA Comparison	84
4.22	Disk inclination $\alpha_s$	86
4.23	UH-60 $Cp$ - $\mu$ curve	87
4.24	UH-60 in advanced flight $u_h = 40m/s$	89
4.25	UH-60 in advanced flight $u_h = 40m/s$ , 5deg of side-slip angle	90
4.26	UH-60 in advanced flight $u_h = 50m/s$	91
4.27	UH-60 in advanced flight $u_h = 60m/s$	92
4.28	ZHAW flight simulator cockpit	93
4.29	ZHAW flight simulator graphic	94
4.30	Translational speeds and roll rate	97
4.31	Flight test results: translational speeds and pitch rate	98
4.32	Speeds and position during take-off	99
4.33	Translational speeds in hover	100
4.34	Vector position's components in hover	100
4.35	Pitch instability in hover	101
4.36	Euler angles during pitch instability in Hover	102

4.37	Translational and rotational speeds in uniform straight flight . . . .	103
4.38	Euler angles curves in uniform straight flight . . . . .	104
4.39	Euler angles and speed rates during 180-deg turn . . . . .	105
4.40	Horizontal positioning's translational speeds and rotational rates .	106
4.41	Euler angles during horizontal positioning . . . . .	106
4.42	Translational speeds and x-position during longitudinal positioning	107
4.43	Euler angles during longitudinal positioning . . . . .	108
4.44	Euler angles and speeds during landing . . . . .	109

## List of Tables

3.1	10KHz (Tus), 1KHz (Eu) and 500Hz (Eu) data comparison . . . . .	52
4.1	XV-15 Hover Flight test-Part 1, Ref. [12] . . . . .	67
4.2	XV-15 Hover Flight test-Part 2, Ref. [12] . . . . .	68
4.3	UH-60 Hover Flight test, Ref. [21] . . . . .	84
4.4	UH-60 TDA Test Results . . . . .	85
4.5	UH-60 Advanced Flight test input, Ref. [21] . . . . .	86
4.6	UH-60 Advanced Flight test results . . . . .	87

# Nomenclature

$\alpha$	Aerodynamic blade element's incidence ( <i>rad</i> )
$\alpha_0$	Zero lift profile incidence ( <i>rad</i> )
$\alpha_s$	Aerodynamic disk's incidence ( <i>rad</i> )
$\beta$	Flapping angle ( <i>rad</i> )
$\beta_0$	Fourier' constant coefficient ( <i>rad</i> )
$\beta_h$	Side-slip angle ( <i>rad</i> )
$\beta_m$	Longitudinal nacelle's angle ( <i>rad</i> )
$\beta_{1c}$	Fourier' lateral coefficient ( <i>rad</i> )
$\beta_{1s}$	Fourier' longitudinal coefficient ( <i>rad</i> )
$\chi$	Disk's skew angle ( <i>rad</i> )
$\ddot{\beta}$	Flapping angular acceleration ( <i>rad/s<sup>2</sup></i> )
$\Delta t$	Temporal step ( <i>s</i> )
$\Delta x$	Radial element's length ( <i>m</i> )
$\delta$	Bramwell' profile drag coefficient ( <i>n/d</i> )
$\dot{\beta}$	Flapping angular speed ( <i>rad/s</i> )
$\dot{\theta}$	Unsteady angular speed's effect ( <i>rad/s</i> )
$\dot{u}_h$	Speed's time variation along x-hub ( <i>m/s<sup>2</sup></i> )
$\dot{v}_0$	Pitt/Peters inflow's constant component derivative ( <i>1/s</i> )
$\dot{v}_h$	Speed's time variation along y-hub ( <i>m/s<sup>2</sup></i> )
$\dot{v}_{1c}$	Pitt/Peters inflow's lateral component derivative ( <i>1/s</i> )
$\dot{v}_{1s}$	Pitt/Peters inflow's longitudinal component derivative ( <i>1/s</i> )
$\dot{w}_h$	Speed's time variation along z-hub ( <i>m/s<sup>2</sup></i> )

$\dot{x}$	States derivative's vector
$\epsilon$	Blade's hinge offset factor ( $n/d$ )
$\gamma$	Lock number ( $n/d$ )
$\lambda$	Bramwell' mean inflow ratio ( $n/d$ )
$\lambda_0$	Inflow's constant component ( $n/d$ )
$\lambda_{1c}$	Lateral cyclic inflow's component ( $n/d$ )
$\lambda_{1s}$	Longitudinal cyclic inflow's component ( $n/d$ )
$\lambda_{zh}$	Dimensionless inflow along z-blade ( $n/d$ )
$\mu$	Advancing ratio ( $n/d$ )
$\mu_z$	Vertical ratio ( $n/d$ )
$\Omega$	Rotor's angular speed ( $rad/s$ )
$\phi$	Euler roll angle ( $rad$ )
$\phi$	Inflow blade angle ( $rad$ )
$\Phi_m$	Lateral nacelle's angle ( $rad$ )
$\psi$	Azimuth angle ( $rad$ )
$\rho$	Density ( $kg/m^3$ )
$\sigma$	Rotor solidity ( $n/d$ )/dynamic system's parameter = $-\zeta w_n$
$\theta$	Euler pitch angle ( $rad$ )
$\theta_0$	Collective (without considering twist) ( $rad$ )
$\theta_{coll}$	Incidence contribution due to the $\theta_0$ , $A1$ and $B1$ ( $rad$ )
$\theta_{twist}$	Twist angle ( $rad$ )
$\vec{W}_h$	Hub's angular speed time variations of the hub ( $rad/s^2$ )
$\vec{a}'$	Acceleration vector of a point in the mobile system ( $m/s^2$ )
$\vec{a}_b$	Total acceleration vector expressed in the blade system ( $m/s^2$ )
$\vec{a}_h$	Acceleration vector of a point expressed in the hub system ( $m/s^2$ )
$\vec{a}_{tr}$	Translational acceleration vector ( $m/s^2$ )
$\vec{d}$	Vector hub center-hinge ( $m$ )

$\vec{g}_g$	Gravitational acceleration contribution expressed in the aircraft body system ( $m/s^2$ )
$\vec{g}_h$	Gravitational acceleration contribution expressed in the hub system ( $m/s^2$ )
$\vec{M}$	Aircraft's pitching moment vector ( $Nm$ )
$\vec{r}_{chxb}$	Vector hub center-radial point of the blade ( $m$ )
$\vec{r}_{tot}$	Vector center of gravity of the aircraft-rotor center ( $m$ )
$\vec{V}'$	Speed vector of a point in the mobile system ( $m/s$ )
$\vec{V}_\lambda$	Vector inflow's speed expressed in the blade system ( $n/d$ )
$\vec{V}_b$	Body aircraft's speed vector ( $m/s$ )
$\vec{V}_h$	Hub's speed vector ( $m/s$ )
$\vec{V}_{pqOb}$	Vector speed induced in a blade point expressed in the blade system ( $m/s$ )
$\vec{V}_{pqOh}$	Vector speed induced on the blade point expressed in the hub system ( $m/s$ )
$\vec{W}_h$	Hub's angular speed vector ( $rad/s$ )
$\vec{X}$	Aircraft's longitudinal force vector ( $N$ )
$\zeta$	Dimensionless damping
$A$	Rotor Area ( $m^2$ )
$a$	Sound speed/ $Cl_\alpha$ ( $1/rad$ )
$A, B, C, D$	Dynamics system's matrices
$A1$	Lateral cyclic ( $rad$ )
$a1$	Bramwell' longitudinal flapping coefficient ( $rad$ )
$a_1$	Tustin' denominator $z$ coefficient
$a_2$	Tustin' denominator independent coefficient
$a_z$	Total acceleration along z-blade ( $m/s^2$ )
$a_{yb}$	Inertial acceleration along y-blade ( $m/s^2$ )
$a_{z1}$	Total acceleration $\beta$ component ( $m/(rads^2)$ )
$a_{z2}$	Total acceleration independent component ( $m/s^2$ )

$a_{zb}$	Inertial acceleration along z-blade ( $m/s^2$ )
$B1$	Longitudinal cyclic ( $rad$ )
$b_0$	Tustin' numerator $z^2$ coefficient
$b_1$	Tustin' numerator $z$ coefficient
$b_2$	Tustin' numerator independent coefficient
$c$	Blade element's chord/Dynamic system's damping
$c^*$	Equivalent chord's length in the scaled model ( $m$ )
$c.g.$	Aircraft's center of gravity
$c.r.$	Rotor center
$c_0$	Chord distribution's constant coefficient ( $m$ )
$c_1$	Chord distribution's 1st order coefficient ( $n/d$ )
$c_2$	Chord distribution's 2nd order coefficient ( $1/m$ )
$c_3$	Chord distribution's 3rd order coefficient ( $1/m^2$ )
$C_t$	Thrust coefficient ( $n/d$ )
$C_{la}$	Aerodynamic rolling moment's coefficient ( $n/d$ )
$C_{ma}$	Aerodynamic pitching moment's coefficient ( $n/d$ )
$CD$	Disk's drag coefficient ( $n/d$ )
$Cd$	Drag coefficient ( $n/d$ )
$Cd+$	Hoerner' Cd function for positive incidence ( $n/d$ )
$Cd-$	Hoerner' Cd function for negative incidence ( $n/d$ )
$Cd_0$	Zero lift drag coefficient( $n/d$ )
$ch$	Hub center
$CL$	Disk's lift coefficient ( $n/d$ )
$Cl$	Lift coefficient ( $n/d$ )
$Cl+$	Hoerner' Cl function for positive incidence ( $n/d$ )
$Cl-$	Hoerner' Cl function for negative incidence ( $n/d$ )
$Cl_\alpha$	Cl gain compared to $\alpha_0$ ( $1/rad$ )

$C_p$	Power coefficient ( $n/d$ )
$C_{p_{id}}$	Ideal power coefficient ( $n/d$ )
$C_Q$	Power coefficient ( $n/d$ )
$df$	Generic elementary force ( $N$ )
$dfa$	Elementary blade element's force along z-blade ( $N$ )
$dfa_1$	Elementary force's along z-blade $\dot{\beta}$ component ( $Ns/rad$ )
$dfa_2$	Elementary force's along z-blade $\beta$ component ( $N/rad$ )
$dfa_3$	Elementary force's along z-blade constant component ( $N$ )
$dl$	Elementary blade element's lift ( $N$ )
$dm$	Elementary blade element's flapping moment ( $Nm$ )
$dm_1$	Elementary flapping moment's $\dot{\beta}$ component ( $Nms/rad$ )
$dm_2$	Elementary flapping moment's $\beta$ component ( $Nm/rad$ )
$dm_3$	Elementary flapping moment's constant component ( $Nm$ )
$dna$	Elementary blade element's moment along z-blade ( $Nm$ )
$dq$	Elementary blade element's force along y-blade ( $N$ )
$e$	Dimensional hinge offset ( $m$ )
$e$	Output's vector
$etha_p$	Rotor efficiency ( $n/d$ )
$F$	Generic force ( $N$ )
$f$	Frequency ( $1/s$ )
$F_\beta$	Flapping dynamics system's forcing
$FM$	Figure of Merit ( $n/d$ )
$g_0$	Earth gravitational's constant = $9.80665m/s^2$
$g_{hz}$	Gravitational acceleration's z-hub component ( $m/s^2$ )
$H$	Aircraft's longitudinal force ( $N$ )
$h$	Vertical rotor distance center of gravity of the aircraft-rotor center/z-body coordinate ( $m$ )
$hc$	Aircraft's longitudinal force coefficient ( $n/d$ )

$I$	Identity matrix
$I_\beta$	Blade's flapping inertia ( $kgm^2$ )
$I_{\beta^*}$	Equivalent flapping inertia in the scaled model ( $kgm^2$ )
$k$	Dynamics system's stiffness/temporal instant
$K_1$	Hinge's misalignment: $\tan(\delta_3)$ ( $n/d$ )
$K_\beta$	Spring flapping stiffness [ $Nm/rad$ ]
$k_{Cd+}$	Hoerner' Cd constant for positive incidences ( $n/d$ )
$k_{Cd-}$	Hoerner' Cd constant for negative incidences ( $n/d$ )
$k_{Cl+}$	Hoerner' Cl constant for positive incidences ( $n/d$ )
$k_{Cl-}$	Hoerner' Cl constant for negative incidences ( $n/d$ )
$L_g$	Aircraft's rolling moment ( $Nm$ )
$L_h$	Rotor moment's along x-hub ( $Nm$ )
$l_m$	Must length ( $m$ )
$M$	Blade flapping integrated moment ( $Nm$ )
$m$	Dynamics system's mass
$M_1$	Integrated flapping moment's $\dot{\beta}$ component ( $Nms/rad$ )
$M_2$	Integrated flapping moment's $\beta$ component ( $Nm/rad$ )
$M_3$	Integrated flapping moment's constant component ( $Nm$ )
$M_\beta$	Blade's mass inertia ( $kgm$ )
$M_{\beta^*}$	Equivalent mass inertia in the scaled model ( $kgm$ )
$M_a$	Aerodynamic flapping moment ( $Nm$ )
$m_b$	Blade's mass ( $kg$ )
$m_{b^*}$	Equivalent blade's mass in the scaled model ( $kg$ )
$M_g$	Aircraft's pitching moment ( $Nm$ )
$M_h$	Rotor moment's along y-hub ( $Nm$ )
$M_t$	Additional blade's torque moment ( $Nm$ )
$M_{tip}$	Mach speed in the tip section = $V_{tip}/a$ ( $n/d$ )

$N$	Number of instants computed in a rotor round ( $n/d$ )
$n_b$	Number of blades ( $n/d$ )
$N_g$	Aircraft's yaw moment ( $Nm$ )
$N_h$	Rotor moment's along z-hub ( $Nm$ )
$N_a$	Aerodynamic integrated blade moment along z-blade ( $Nm$ )
$N_{a_1}$	Integrated moment's along z-blade $\dot{\beta}$ component ( $Nms/rad$ )
$N_{a_2}$	Integrated moment's along z-blade $\beta$ component ( $Nm/rad$ )
$N_{a_3}$	Integrated moment's along z-blade constant component ( $Nm$ )
$p$	Aircraft's roll angular rate ( $rad/s$ )
$p_h$	Hub's rolling angular speed ( $rad/s$ )
$phi$	Euler roll angle ( $rad$ )
$Q$	Aerodynamic integrated blade force along y-blade ( $N$ )
$q$	Aircraft's pitch angular rate ( $rad/s$ )
$q_h$	Hub's pitch angular speed ( $rad/s$ )
$R$	Blade's radial extension ( $m$ )
$r$	Radial blade's coordinate ( $m$ )
$R^*$	Equivalent radial extension in the scaled model ( $m$ )
$r_h$	Hub's yaw angular speed ( $rad/s$ )
$r_q$	Aerodynamic blade's radial position ( $m$ )
$r_{cg}$	Blade center of gravity's radial position ( $m$ )
$S$	Centrifugal force of blade ( $Nm/rad$ )
$T$	Temperature ( $K$ )/generic temporal instant ( $s$ )
$t$	Simulation time ( $s$ )
$t_0$	Twist distribution's constant coefficient ( $rad$ )
$t_1$	Twist distribution's 1st order coefficient ( $rad/r$ )
$t_2$	Twist distribution's 2nd order coefficient ( $rad/r^2$ )
$t_3$	Twist distribution's 3rd order coefficient ( $rad/r^3$ )

$t_{round}$	Time for a rotor round ( $s$ )
$theta$	Euler pitch angle ( $rad$ )
$u$	Input vector/aircraft's axial speed
$u_h$	X-axis hub's speed component ( $m/s$ )
$V$	Blade element's total speed intensity ( $m/s$ )
$v$	Aircraft's lateral speed ( $m/s$ )
$v_0$	Pitt/Peters inflow's constant component ( $n/d$ )
$v_h$	Y-axis hub's speed component ( $m/s$ )
$v_m, v_t$	Mass flow parameters ( $n/d$ )
$V_P$	Blade's perpendicular speed ( $m/s$ )
$V_T$	Blade's tangential speed ( $m/s$ )
$v_{1c}$	Pitt/Peters inflow's lateral component ( $n/d$ )
$v_{1s}$	Pitt/Peters inflow's longitudinal component ( $n/d$ )
$V_{tip}$	Blade tip speed due to $\Omega \rightarrow \Omega r$ ( $m/s$ )
$V_{tot}$	Total aircraft's speed intensity ( $m/s$ )
$w$	Aircraft's vertical speed ( $m/s$ )
$w$	Dynamic system's pulsation ( $1/s$ )
$w_h$	Z-axis hub's speed component ( $m/s$ )
$w_n$	Dynamic system's natural pulsation ( $1/s$ )
$x$	States vector/Aircraft's axial position coordinate
$X_1$	First peak's height ( $rad$ )
$X_2$	Second peak's height ( $rad$ )
$x_b$	X-axis blade system's coordinate ( $m$ )
$x_g$	X-axis aircraft body system's coordinate ( $m$ )
$X_h$	Rotor's force along x-hub ( $N$ )
$x_h$	X-axis hub system's coordinate ( $m$ )
$x_r$	X-axis rotor system's coordinate ( $m$ )

$x_{uo}$	Unsteady aerodynamic's contribution offset
$y$	Aircraft's lateral position coordinate ( $m$ )
$y_b$	Y-axis blade system's coordinate ( $m$ )
$y_g$	Y-axis aircraft body system's coordinate ( $m$ )
$Y_h$	Rotor's force along y-hub ( $N$ )
$y_h$	Y-axis hub system's coordinate ( $m$ )
$y_r$	Y-axis rotor system's coordinate ( $m$ )
$z$	Laplace' coordinate
$z_b$	Z-axis blade system's coordinate ( $m$ )
$z_g$	Z-axis aircraft body system's coordinate ( $m$ )
$Z_h$	Rotor's force along z-hub ( $N$ )
$z_h$	Z-axis hub system's coordinate ( $m$ )
$z_r$	Z-axis rotor system's coordinate ( $m$ )
$[L]$	Pitt/Peters' gain matrix ( $n/d$ )
$[M]$	Pitt/Peters' apparent mass matrix ( $n/d$ )
$[T_\beta]$	$\beta_m$ nacelle transformation matrix ( $n/d$ )
$[T_\phi]$	$\phi$ nacelle transformation matrix ( $n/d$ )
$[T_{AH}]$	Disk-hub transformation matrix ( $n/d$ )
$[T_{hr}]$	Hub-rotor transformation matrix ( $n/d$ )
$[T_{rb}]$	Rotor-blade transformation matrix ( $n/d$ )

# Chapter 1

## Introduction

The present work is developed in order to solve one of the most complicated problems in the aeronautical field, the rotor system. In these systems, two or more blades are put into rotation around an axes with the aim to create forces and moments in order to sustain the aircraft. The blades of a rotor, which adopt an aerodynamic shape similar to the wings of an airplane and is born in accordance with the same principle, are inserted into a rotating mechanism. That allows the aircraft to flight in all directions, but especially at a fixed point, in fact, the rotation of the blades produces an upward thrust that overcomes the weight of the aircraft. By varying the blade's incidence angle, known as the pitch angle, the helicopter climb or lose height and by varying it cyclically is created a differential lift between the front and rear blades during the rotation according to the direction of flight desired. The first ideas on the concept of the rotating wing date back to the time of Leonardo da Vinci, who, as shown in the following figure, already outlined the idea in one of his various sketches, Ref. [22].

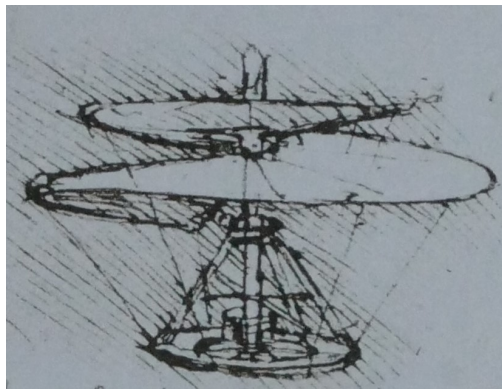


Figure 1.1: Leonardo da Vinci rotor sketch

In particular, the present work is focused on helicopters and tilt-rotors, even if the rotor model can be easily specialized for turbo-propellers airplane engines also. Most modern helicopters and tilt-rotors use one of the following main rotor types: rigid, semi-rigid and articulated.

## 1.1 Rigid rotor

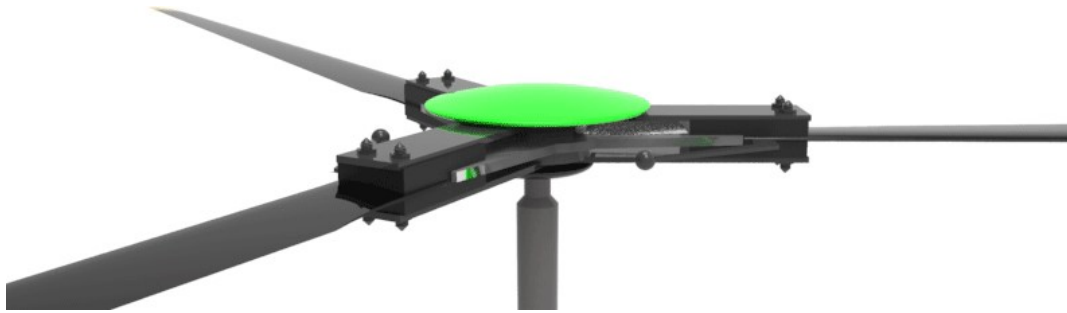


Figure 1.2: Rigid rotor model

The rigid rotor is one of the three main rotors types used in modern helicopters. A rigid rotor system has two or more main rotating blades. They are mechanically simple, but technologically complicated, as the stresses during operation must be absorbed only by the material from which the blades are made not having any hinge. In these configurations, the blades flap upwards or downwards due to their flexibility. The blades tilt up or down independently of each other to compensate for the asymmetric lift. In addition, the blades can independently change their angle of attack during rotation. What is more, unlike an articulated rotor, the rigid one adopt no joints. This type of rotors are the most expensive produced because of their complexity. In fact, they are normally made of composite material and titanium and have a tendency to cause a relatively uneven stroke. However, these rotors withstand ground resonance and require less maintenance than other rotor systems.

## 1.2 Semi-Rigid rotor

A semi-rigid rotor allows two different movements: flapping and changing the angle of incidence. This system normally consists of two blades rigidly connected to the rotor hub. The blades tilt up or down all at once, like a swing, to compensate for the asymmetric lift. The blades are also able to change their angle of attack solidly during rotation. The hub is in turn connected to the rotor shaft by a tilting hinge ("teetering hinge"). This structure allows the blades to "flap" as they swing: when one blade swings downwards, the other swings upwards. The rotation along the longitudinal axis is allowed through the connecting rods controlled by the oscillating plate, which control the variation of the angle of incidence according to what is required by the flight controls. The rotor system is also sprung to compensate for the Coriolis force, delay and advance of the main rotor blades caused by the oscillation of the center of gravity with respect to the axis of rotation. Semi-rigid rotor systems require relatively little maintenance, but their upward and downward displacement characteristics can generate hub's oscillations.



Figure 1.3: Robinson R-22 semi-rigid rotor

### 1.3 Articulated rotor



Figure 1.4: UH-60 articulated rotor

The articulated rotor has two or more main rotor blades that tilt up or down independently of each other to compensate for asymmetric lift. Each blade is connected to the rotor hub by a hinge, called a "flapping hinge", which allows free and independent upward or downward oscillations. The hinge can be placed at different distances from the center of the rotor and there can be more than one of these. The position is chosen by each manufacturer on the basis of factors that improve stability and control. The blades are also connected to the rotor by a vertical hinge called "retreat hinge" or "delay hinge" or also "swing hinge" ("drag or lag hinge") which allows each blade to move forward or backward along the plane designed by the disc of the rotor, independently of the others. Normally, shock absorbers are installed to avoid excessive movement in this direction. The purpose of this hinge-damping system is to absorb the accelerations and decelerations ("Coriolis effect") of the blades during rotation. The blades of the fully

articulated rotors can also rotate along their axis, that means changing the angle of incidence with the purpose to generate the lift necessary for the support of the aircraft. The production and maintenance of fully articulated rotor systems is more expensive than semi-rigid rotors. However, these systems are less affected by low gravity conditions and hub oscillations. In addition, these rotors are also less affected by ground resonance. The UH-60 articulated rotor is selected as a representative example of reference and is used for the validation of the rotor model as it is shown later.

## 1.4 Functions and machines

As a matter of facts, the employment of these type of aircraft (helicopter and tilt-rotors) grown up quite fast in the last decades, in fact, the flexibility and the high amount of functions which distinguishes them from a classical aircraft led to a notable development of these machines. Among the most meaningful examples of aircraft the following machines deserve to be mentioned.

### 1.4.1 XV-15 Tilt rotor



Figure 1.5: Bell/Boeing XV-15 prototype in helicopter mode

The Bell XV-15 is a tilt-turn-over convertiplane. Designed in the 1970s by the US company Bell Aircraft Corporation under the designation Model 301, it is considered to be the first successful tilt-rotor. The goodness of the project led to the development of the subsequent Bell-Boeing V-22 Osprey and Bell-Agusta BA609, the first two series-produced tilt-rotors at a time when the interest for the development of this type of aircraft was truly strong especially for their great

maneuverability near the ground (VTOL). It was modernized and improved compared to its predecessor, the XV-3, in order to meet FAA standard requirements and to provide better performances. The XV-15 has a bidirectional tail and a cantilever wing with rotating gondolas at the ends, each housing a turbo propeller driving a large propeller/rotor. The wing also incorporated flaps/ailerons and flaps; an advanced device was the system for increasing stability and control. Two were built; the first made an initial stationary flight in May 1977, while the second completed the full transition tests in July 1979. Since the University of ZHAW has a flight simulation model of the XV-15 already developed, but still not properly working for some issue connected to the previous rotor model, as shown in Ref. [1] it was possible to perform most of the validation tests on this aircraft. For these reasons, this particular tilt-rotor is the reference for the rotor model developed in the present work.

### 1.4.2 UH-60 Blackhawk



Figure 1.6: UH-60 Blackhawk helicopter

The Sikorsky UH-60 Black Hawk is an 'heavy', single rotor, multi-role or assault twin-turbine helicopter manufactured by the US company Sikorsky Aircraft Corporation since the 1970s. Derived from the civilian version Sikorsky S-70 is currently still in service in many armed forces worldwide in its most recent versions. UH-60 has four main blades and tail rotors, and is powered by two General Electric T700 turbo-shaft engines. The main rotor is fully articulated and has elastomeric rotor head bearings. The tail rotor is tilted and has a rigid cross-head. The helicopter has a long, low-profile shape to meet the army's demands for transportation on board a C-130 Hercules. It can carry 11 people with equipment, lift 2,600 pounds (1,200 kg) of cargo internally or 9,000 pounds (4,100 kg) of cargo (for UH-60L / M) externally by slinging. The Black Hawk helicopter series can perform a wide range of missions, including tactical troop

transport, electronic warfare, and aero-medical evacuation. A new version is currently being developed that will take the name UH-60M and will extend the service life of both UH-60A and UH-60L until at least the 2020s. Towards the end of the eighties the design was updated with the introduction of the UH-60L (first production model 89-26179) with greater power and increased payload following the passage of the General Electric engines to the 701C model. The variant under development has further enhanced engines capable of delivering increased power and payload as well as technologically advanced avionics and flight control systems. Since a lot of data on this aircraft is available in literature, this aircraft is also chosen as a reference point for the experimental validation of this work.

### 1.4.3 V-22 Osprey



Figure 1.7: V-22 tilt-rotor

Another example of tilt-rotor is the Bell V-22, which is among the rare examples currently in use. It is equipped with a three-blade prop-rotors. One of the special features of this aircraft is its ability to fully rotate the nacelles ( $90^\circ$ ) in just twelve seconds, thus making a truly rapid transition between helicopter and airplane mode. Its operating range is around 3900 Km and 954 km is the radius of action. The aircraft is equipped with relatively small wings, at the end of which are horizontally hinged the gondolas of turbine engines that move large diameter propellers as a function of load-bearing rotors, and dual-drift tail spikes. The engines are two Allison turboprop engines with 4970 hp of power on the shaft, power that can be pushed up to 5920 hp in case of emergency with an engine out of use. The three-blade rotors have a diameter of 11.58 m and blades in resin reinforced with fiberglass and graphite that develop a total bearing area

of 24.30 square meters. In addition, the two rotors shaft are interconnected to avoid the consequences that would occur in the event of failure of one of them. The wings, which are thick enough to support the rotor lift applied to the end, are specifically designed for low speed flight and allow a minimum speed in horizontal flight of 74 km/h. The rotor blades can be folded up by means of an automatic system and, in the Navy and Marine versions, the entire wing can be rotated until it is parallel to the fuselage, to facilitate stowage on board ships. The structure is made mainly of composite materials in epoxy resin reinforced with carbon fibers which, at the same weight, increase the mechanical and environmental resistance compared to a metal structure. Also, part of blades are made in composite materials. In order to increase the aircraft's ability to withstand adverse shocks, the steering, electrical and hydraulic systems are triple and completely independent. Furthermore, the Osprey is the only aircraft in the world equipped with an alarm system against the so-called 'Vortex Ring State', which occurs when a helicopter descends at a speed higher than that impressed on the air by the rotor blades and which manifests itself with a sudden, total and difficult to recover loss of lift with catastrophic consequences. A 17.4 m long aircraft with a wingspan of 17.4 m and a height of 6.73 m. When empty, the aircraft has a mass of 15032 kg but can be equipped up to a weight of 23892 kg in case of vertical take-off, and 27442 kg with a take-off in airplane mode. In this mode its peak speed reaches 510 km/h; while the vertical climb rate is 5.5 m/s. As altitude the tangency reaches 7620 m, 3400 m with only one engine running. The unit cost: 89 million US dollars in 2005.

#### 1.4.4 Dufour Aerospace tilt-wing concept



Figure 1.8: Dufour Aerospace tilt-wing concept

Another interesting example of a rotor application is the model of the Dufour Aerospace, a Swiss company, in collaboration with the University of ZHAW. The aircraft is still under development and it is designed to be electrically motorized and the most compact and efficient in order to accomplish short-to-medium

range missions. Its compact design and low emissions make it the ideal aircraft for future short-distance air transport, especially within inhabited areas. The main targets are the urban transportation but also for revolutionize mountain, rural transport and medical aid.

#### 1.4.5 Bell V-280

A more recent and optimized version of the V-22 is the V-280, which is capable of a cruising speed of 520 km/h, with a top speed of 560 km/h, a range of 3900 km) and an effective range of action of 1480 km. The MTO weight is around 14000 kg. The fuselage is visually similar to that of the UH-60 Black Hawk medium lift helicopter. Another improvement is the adoption of a 'V' tail that allows to save weight considerably, even if the aeroelastic control system of the rearing itself must be adapted to avoid instability phenomena such as the flutter, that are more frequent with this type of structure.



Figure 1.9: V-280 tilt-rotor

The wings are made of a large cell carbon core. The helicopter is designed to carry four crew members and 11 troops. It will feature two spacious 1.83 m side doors for convenient entry and exit of armed forces. The V-280 helicopter is equipped with triple redundant fly-by-wire flight control system for precision aircraft handling and improved safety. The system helps to reduce the workload of pilots and weight of the aircraft while minimizing the maintenance costs as compared to traditional flight control systems. The aircraft will offer greater fuel-efficiency, resulting in smaller logistical footprint compared to other aircraft.

## Chapter 2

# Development of the mathematical model

In order to realize a model that meets all the requirements of the real time simulation, it is appropriate to realize a new mathematical model starting from the aerodynamic and mechanical principles that govern the problem. Therefore, the first step is the definition of the reference systems, mobile and rotating, with the respective rotation matrices; that allows the passage from one triad to another. Later, it is appropriate to define all the speed contributions acting on the blade:

- *Speeds flight and wind contributions*
- *Inflow contribution*
- *Kinematic speeds due to the rotations of the aircraft around its axes*
- *Speed due to the rotational speed of the rotor*

Once the resulting aerodynamics are calculated with the blade element theory, before obtaining the total loads at the hub, it is opportune to estimate all the accelerations contributions acting at the center of gravity of the blade in order to obtain the inertial, gravitational and centrifugal loads also; then, these are added to the aerodynamic ones previously found. Therefore, all of the following accelerations are taken into account:

- *Centrifugal*
- *Gravitational*
- *Accelerations due to Coriolis contributions*
- *Due to translational accelerations of the body*
- *Due to rotational accelerations of the body*

Once all the estimated contributions are added, through the rotation matrices, it is possible to obtain the forces and moments acting on the hub reference system

attached to the aircraft. Finally, it is appropriate to take into account the position in space of the nacelle, with its angles and reference distances from the center of gravity of the aircraft, in order to obtain the loads transmitted by the rotors to the aircraft reference system.

## 2.1 Assumptions

The main aim of this work is to maintain as much as possible the truthfulness of the model and at the same time to comply with the requirements of real-time. For this particular reason, a trade-off between the level of detail of the model and its performance must be carried out. Thus, according to [11] and previous works such as [3] and [16], the rotor dynamics is limited to the only flapping degree of freedom, therefore lead-lag dynamics and torsion dynamics are neglected. On the other hand, the model implements the full, second-order flapping dynamics of each blade with no approximation to reduce the order of the tip-path-plane dynamics and a full calculation of the air-loads along the blade span as function of the azimuth position. Therefore, it is appropriate to make the following assumptions:

- Air-loads are expressed by exploiting the Blade Element Theory and integrating symbolically along each blade span; therefore, no numerical integration must be performed during the simulation, but mere algebraic calculations must be computed at each time step.
- The blade section's aerodynamics is expressed with no approximation about low angles and therefore extended to large inflow angles (which are generally typical for prop-rotors and propellers, [12]).
- The blade section's aerodynamic data are derived from conventional 2-D analysis based on equipotential methods for the linear part and then expanded for large angles of attack exploiting the semi-empirical formulation proposed by Hoerner in [13], where the coefficients are calibrated to match the trends of the experimental data. This method allows to properly tune the airfoil characteristics to better suit the real blade and reproduce stall and post-stall behaviours.
- Each blade is considered rigid in bending and torsion, an equivalent spring is placed at the flap hinge and it can be properly tuned to reproduce the behaviour of different rotor designs (rigid, fully articulated, hinge-less, gim-bals rotors).
- The blade twist distribution is expressed using a third-degree polynomial which can be tuned to well suit prop-rotor as well as conventional rotor designs.
- The chord distribution is also introduced using a third-degree polynomial so that a wider range of blade designs can be implemented.

- The approximation of small flapping angles  $\beta$  is used only in the mathematical formulation of the flapping dynamics. This assumption is needed to express the flapping dynamic analytically and it is believed to be acceptable based on previous literature [4] and safety limitations of tilt-rotor designs (XV-15 flapping is limited within  $\pm 12$  degrees, as reported in [6]).
- The effect of  $\dot{\beta}$  on the sectional angle of attack is assumed to be small and therefore linearized with a first order Taylor approximation to preserve the analytic formulation of the flapping dynamics. Therefore this term of aerodynamic incidence is simplified as  $\frac{\dot{\beta}r}{\Omega(e+r)}$  by neglecting, for this term only, the effect of the hub components of velocities (considerably smaller than the  $\Omega(e+r)$  contribution in the most aerodynamically significant sections of the blade) which might now lead to singularities in the model for blade stations close to the hub at which, in some translational flight regimes, the denominator might become zero.
- In the formulation of the speeds acting on the blade, the yaw's angular rate ( $r_h$ ) is neglected as not meaningful in comparison to the others terms, in accordance with Ref. [4] again.
- Terms in  $\ddot{\beta}$  and the Coriolis contribution due to  $\dot{\beta}$  are also considered small and neglected only when calculating the accelerations acting on the blade, as also referred in [4].
- To simplify the resolution of the flapping dynamics, in the mathematical treatment the term drag,  $C_d$ , is considered independent from the contribution in  $\dot{\beta}$ , as it is small compared to the other terms of the aerodynamic incidence.
- A dynamic inflow model is implemented based on Pitt-Peters formulation [5], as shown later;
- An analytic formulation of the tip loss factor is implemented according to what shown in [18].
- All the aeroelastic effects acting on the blade and of the rotor structure are neglected not to further increase the computational load.
- The rotational speed acceleration  $\dot{\Omega}$  is considered equal to zero, considering the rotor working always with the same value of  $\Omega$ , assumption valid for the the major part of the mission of helicopter and tilt-rotor.

## 2.2 References systems and rotating matrices

During the mathematical treatment it is appropriate to take into account three main reference systems: one attached to the aircraft centered in the hub system, another rotating with the rotor and a system attached to the blade also rotating, as reported in Ref. [19] and [9]. The body reference system for calculating the loads acting on the center of gravity of the aircraft is also considered below in the body-hub moments transportation.

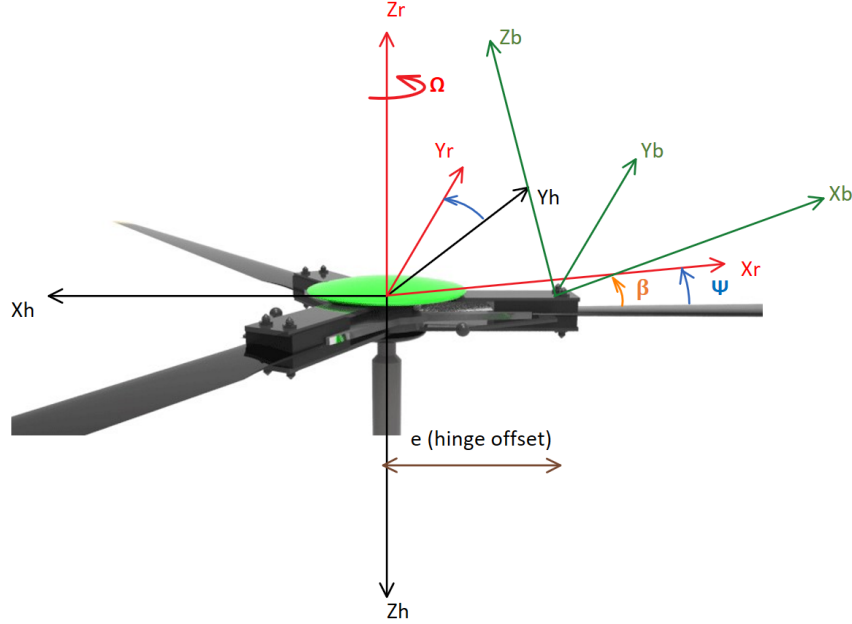


Figure 2.1: Reference systems adopted

In figure above are shown the three reference systems adopted with their orientation in the space. The subscript 'h', respectively, indicates the hub reference system, 'r', the rotor system and 'b' the blade system. The last one is centered in the flap hinge, instead, the previous have their origin in the center of the hub. The rotor system is turning around the  $z_r$  generating the azimuth angle, which origin is fixed as indicated in the figure. The value of this angle is easily computed as  $\psi = \Omega t$ , where  $t$  is the current simulation time. The blade system, instead, is turning around  $y_b$  axes of the flapping angle  $\beta$ . In order to pass from a reference system to another the following rotational matrices are used:

- Rotational matrix center of hub reference system-rotor system:

$$T_{hr} = \begin{bmatrix} -\cos(\psi) & \sin(\psi) & 0 \\ \sin(\psi) & \cos(\psi) & 0 \\ 0 & 0 & -1 \end{bmatrix} \quad (2.1)$$

- Rotational matrix rotor system-blade system:

$$T_{rb} = \begin{bmatrix} \cos(\beta) & 0 & -\sin(\beta) \\ 0 & 1 & 0 \\ \sin(\beta) & 0 & \cos(\beta) \end{bmatrix} \quad (2.2)$$

Also, it is important to consider two other transformation matrices, which take into account the two nacelle's angles:

- $\phi_m$ :

$$T_{\phi} = \begin{bmatrix} 1 & 0 & 0 \\ 0 & \cos(\phi_m) & \sin(\phi_m) \\ 0 & -\sin(\phi_m) & \cos(\phi_m) \end{bmatrix} \quad (2.3)$$

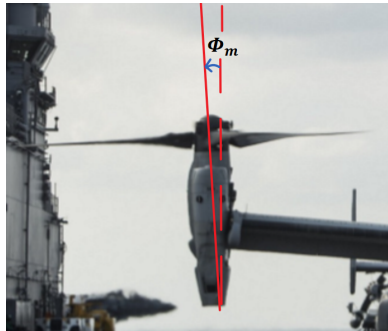


Figure 2.2: V-22  $\phi_m$  nacelle angle

- and  $\beta_m$ :

$$T_{\beta} = \begin{bmatrix} \cos(\beta_m) & 0 & \sin(\beta_m) \\ 0 & 1 & 0 \\ -\sin(\beta_m) & 0 & \cos(\beta_m) \end{bmatrix} \quad (2.4)$$

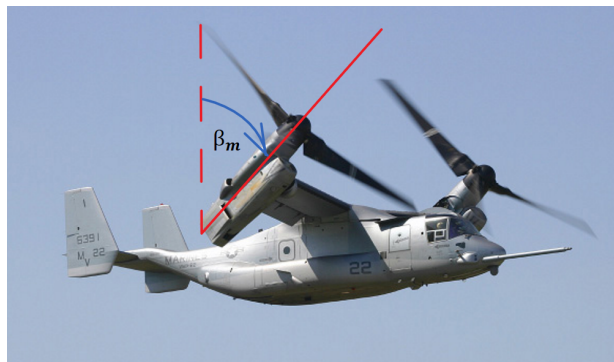


Figure 2.3: V-22  $\beta_m$  nacelle angle

Thanks to these last two rotation matrices it is possible to pass from a vector in the body reference system directly to the hub reference system. In fact, considering a generic vector  $\vec{f}_b$ , it can be transported in the hub reference system thanks to the relation:

$$\vec{f}_h = [T_\beta][T_\phi]\vec{f}_b \quad (2.5)$$

After that, since the length of the must ( $l_m$ ) is known as its distance from the body x-axis, it is possible to pass the quantities from the body reference system to the hub one.

## 2.3 Speeds and aerodynamic incidence

In order to elaborate the definition of the aerodynamic incidence and then all the forces and moments acting on each blade it is necessary to define all the contributions of tangential and transverse speed to the blade as predicted by the 'Blade element theory':

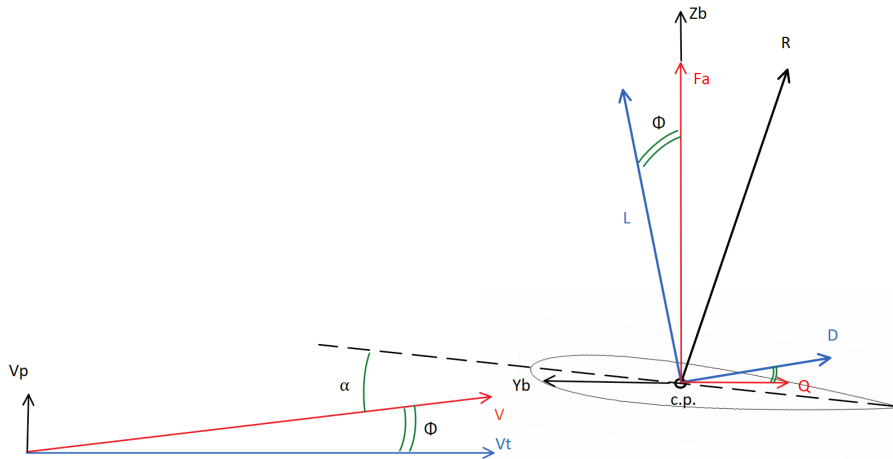


Figure 2.4: Speed and forces acting on the blade element

Introducing the speed components due to the translation of the aircraft and to the wind in the hub reference system as:

$$\vec{V}_h = [u_h, v_h, w_h] \quad (2.6)$$

Therefore, the speeds felt by the blade due to the latter contribution in the blade system after the transformation assume the shape:

$$\vec{V}_b = \begin{bmatrix} v_h \sin(\psi) - u_h \cos(\psi) \\ u_h \sin(\psi) + v_h \cos(\psi) \\ -w_h \end{bmatrix} \quad (2.7)$$

To define the contribution of the body angular speeds it is introduced the vector distance center of the rotor - flap hinge in the rotor system:

$$\vec{d} = [e, 0, 0] \quad (2.8)$$

Also, the vector center of the hub-point of the blade in the hub system is:

$$\vec{r}_{chxb} = \begin{bmatrix} -(e+r)\cos(\psi) \\ (e+r)\sin(\psi) \\ 0 \end{bmatrix} \quad (2.9)$$

Once defined the angular speeds of the aircraft in the center of gravity system as  $\vec{W}_h = [p_h, q_h, 0]$  disregarding the  $r_h$  contribution as announced before, it is possible to find the speed induced in a point of the blade by  $p_h$ ,  $q_h$  and  $\Omega$  in the center of gravity system:

$$\vec{V}_{pqOh} = \begin{bmatrix} \Omega(e+r)\sin(\psi) \\ \Omega(e+r)\cos(\psi) \\ (e+r)[p_h\sin(\psi) + q_h\cos(\psi)] \end{bmatrix} \quad (2.10)$$

Which, when transformed into the blade system, becomes:

$$\vec{V}_{pqOb} = [T_{hr}]\vec{V}_{pqOh} = \begin{bmatrix} 0 \\ \Omega(e+r) \\ -(e+r)[p_h\sin(\psi) + q_h\cos(\psi)] \end{bmatrix} \quad (2.11)$$

Then the dynamic inflow distribution along the blade from the Pitt/Peters Model is considered:

$$\lambda_{zh} = \lambda_0 + \frac{r}{R}\lambda_{1c}\cos(\psi) + \frac{r}{R}\lambda_{1s}\sin(\psi) \quad (2.12)$$

And, the dimensional speed due to the inflow in the blade system takes the following form:

$$\vec{V}_\lambda = \begin{bmatrix} 0 \\ 0 \\ -\lambda_0 - \frac{r}{R}\lambda_{1c}\cos(\psi) - \frac{r}{R}\lambda_{1s}\sin(\psi) \end{bmatrix} \quad (2.13)$$

Adding all the contributions, the perpendicular speed acting on the blade can be written as:

$$\begin{aligned} V_P = & \frac{[q_h(e+r)R - V_{tip}r\lambda_{1c}]\cos(\psi) + [p_h(e+r)R - V_{tip}r\lambda_{1s}]\sin(\psi)}{R} + \\ & + \frac{R(-V_{tip}\lambda_0 + w_h)}{R} + \\ & + x_{uo}[A1\Omega\sin(\psi) - B1\Omega\cos(\psi)] \end{aligned} \quad (2.14)$$

The last term of Eq. (2.14) is a first-order contribution which introduces an approximated unsteady component which is connected to  $\dot{\theta}$  through the offset  $x_{uo}$ ,

according to the formulation derived from Theodorsen's theory and reported by Johnson in [14]. Furthermore, the effect of the hub's rotational ( $p_h, q_h, 0$ ) and translational rates ( $u_h, v_h, w_h$ ) are also taken into account. Instead, adding the translational speed contributions and the rotational speed allows to find the complete definition of the tangential speed acting on the blade (considering  $\Omega$  positive in counterclockwise direction as in Fig. 2.1) which takes the following form:

$$V_T = \sin(\psi)u_h + \cos(\psi)v_h + \Omega(e + r) \quad (2.15)$$

Before enunciate the aerodynamic incidence of each blade element the collective, the lateral and longitudinal cyclic contributions are defined as:

$$\theta_{coll} = \theta_0 - A1\cos(\psi) - B1\sin(\psi) \quad (2.16)$$

And the twist law of the third order as anticipated before:

$$\theta_{twist} = t_3r^3 + t_2r^2 + t_1r + t_0 \quad (2.17)$$

Finally, adding the misalignment of the hinge  $K_1 = \tan(\delta_3)$  and the zero lift incidence, is now possible to define the aerodynamic incidence as:

$$\alpha = \theta_{twist} + \theta_{coll} - K_1\beta + \arctan\left(\frac{V_p}{V_t}\right) - \alpha_0 - \frac{\dot{\beta}r}{\Omega(e + r)} \quad (2.18)$$

And then explicating the terms:

$$\alpha = K_1\beta + \theta_0 - A1\cos(\psi) - B1\sin(\psi) + t_3r^3 + t_2r^2 + t_1r + t_0 + \arctan\left(\frac{V_p}{V_t}\right) - \alpha_0 - \frac{\dot{\beta}r}{\Omega(e + r)} \quad (2.19)$$

Where the term  $\frac{\dot{\beta}r}{\Omega(e+r)}$  is not considered in the arcotangent to facilitate the resolution of the flapping equation that follows. In fact, as announced in the initial hypotheses, for this term, Taylor's first order approximation is still valid. While, since all the other contributions of speed are contained in the arcotangent, and the denominator  $\Omega(e + r)$  can never be zero, all the possible discontinuities that can be obtained if these other terms would also be approximated with Taylor, are avoided. In fact, if this approximation wouldn't be made, in certain conditions of translated flight, where along the blade in some azimuth positions and for particular distances from the root, there could be values of tangential velocity close to zero, and therefore, discontinuities and malfunctions of the model would be recorded.

## 2.4 Aerodynamic forces and moments

Since, the aerodynamic incidence for each station of the blade is defined, is now possible to define the elementary forces and moments. First, however, it is necessary to make explicit the third order chord law as:

$$c(r) = c_3r^3 + c_2r^2 + c_1r + c_0 \quad (2.20)$$

Also, the tilt angle of the total speed felt by the blade is evaluated as:

$$\phi = \text{atan}\left(\frac{V_p}{V_t}\right) \quad (2.21)$$

Where the perpendicular and tangential speeds are defined in Eq. (2.14 , 2.15).

Therefore, the elementary aerodynamic lift can be written as:

$$dl = \frac{1}{2}\rho V^2 c(r) C_{l\alpha} \alpha dr \quad (2.22)$$

The elementary aerodynamic moment around  $y_b$  as:

$$dm = \frac{1}{2}\rho V^2 c(r) [C_d \sin(\phi) + C_{l\alpha} \alpha \cos(\phi)] r dr \quad (2.23)$$

The elementary aerodynamic force along  $z_b$  as:

$$dfa = \frac{1}{2}\rho V^2 c(r) [C_d \sin(\phi) + C_{l\alpha} \alpha \cos(\phi)] dr \quad (2.24)$$

The elementary aerodynamic force along  $y_b$  as:

$$dq = \frac{1}{2}\rho V^2 c(r) [C_d \cos(\phi) - C_{l\alpha} \alpha \sin(\phi)] dr \quad (2.25)$$

The elementary aerodynamic moment around  $z_b$  as:

$$dna = \frac{1}{2}\rho V^2 c(r) [C_d \cos(\phi) - C_{l\alpha} \alpha \sin(\phi)] r dr \quad (2.26)$$

Since in the definition of incidence the linearity in the terms in  $\beta$  and  $\dot{\beta}$  is preserved, and all the definitions of elementary forces and moments maintain the linearity in these terms. Then, manipulating the equations collecting these two terms, is possible to reach the generic form for each contribution:

$$df = df_1 \dot{\beta} + df_2 \beta + df_3 \quad (2.27)$$

After replacing the definition of incidence, speeds and the law of taper is possible

to specify the terms in  $\beta$ ,  $\dot{\beta}$  and the independent one of the collected form. Therefore, the aerodynamic moment along  $y_b$ , which is useful for the resolution of the second order flapping dynamics, is related to the terms:

$$\begin{aligned}
dm_1 &= -\frac{\rho(V_t^2 + V_p^2)r(c_3r^3 + c_2r^2 + c_1r + c_0)\cos(\phi)C_{l\alpha}}{2\Omega(e+r)} \\
dm_2 &= -\frac{1}{2}[\rho(V_t^2 + V_p^2)r(c_3r^3 + c_2r^2 + c_1r + c_0)\cos(\phi)C_{l\alpha}K_1] + \\
dm_3 &= \frac{1}{2}\{\rho(V_t^2 + V_p^2)r(c_3r^3 + c_2r^2 + c_1r + c_0)[C_d\sin(\phi) + \\
&\quad + C_{l\alpha}\cos(\phi)(t_3r^3 + t_2r^2 + t_1r + t_0 - A1\cos(\phi) - B1\sin(\phi) + \\
&\quad + atan(\frac{V_p}{V_t}) - \alpha_0 + \theta_0)]\}
\end{aligned} \tag{2.28}$$

And the elementary aerodynamic moment can be expressed as:

$$dm = dm_1\dot{\beta} + dm_2\beta + dm_3 \tag{2.29}$$

A similar shape is obtained for all other aerodynamic forces and moments, omitted for brevity. Therefore, is possible to find the elementary aerodynamic force along  $z_b$  as:

$$dfa = df_{a1}\dot{\beta} + df_{a2}\beta + df_{a3} \tag{2.30}$$

The elementary aerodynamic force along  $y_b$  as:

$$dq = dq_1\dot{\beta} + dq_2\beta + dq_3 \tag{2.31}$$

The elementary aerodynamic moment around  $z_b$  as:

$$dna = dna_1\dot{\beta} + dna_2\beta + dna_3 \tag{2.32}$$

As method of integration along the blade, the numerical method of the trapezoids over a number of 'n' intervals, at the discretion of the user, is chosen. Therefore, resuming the generic function in Eq. (2.33):

$$df = df_1\dot{\beta} + df_2\beta + df_3 \tag{2.33}$$

That, after using trapezoids, becomes:

$$F = \frac{\Delta x}{2}[df(x_1) + 2df(x_2) + 2df(x_3) + \dots + 2f(x_n) + f(x_{n+1})] \tag{2.34}$$

Then, by replacing the collected form in Eq. (2.33) is found that:

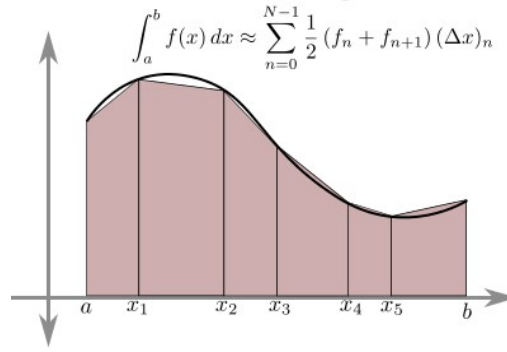


Figure 2.5: Trapezoids rule

$$F = \frac{\Delta x}{2} [df_1(x_1)\dot{\beta} + df_2(x_1)\beta + df_3(x_1) + 2(df_1(x_2)\dot{\beta} + df_2(x_2)\beta + df_3(x_2)) + 2\dots + df_1(x_{n+1})\dot{\beta} + df_2(x_{n+1})\beta + df_3(x_{n+1})] \quad (2.35)$$

And collecting again the terms in  $\dot{\beta}$  and  $\beta$  the following form is reached:

$$F = \frac{\Delta x}{2} [\dot{\beta}(df_1(x_1) + 2df_1(x_2) + 2\dots + df_1(x_{n+1})) + \beta(df_2(x_1) + 2df_2(x_2) + 2\dots + df_2(x_{n+1})) + (df_3(x_1) + 2df_3(x_2) + 2\dots + df_3(x_{n+1})))] \quad (2.36)$$

Which can be resumed as follow:

$$F = F_1\dot{\beta} + F_2\beta + F_3 \quad (2.37)$$

Following the same procedure for all aerodynamic contributions is found that the aerodynamic moment along  $y_b$  can be expressed as:

$$M = M_1\dot{\beta} + M_2\beta + M_3 \quad (2.38)$$

The integrated aerodynamic force along  $z_b$  as:

$$Fa = Fa_1\dot{\beta} + Fa_2\beta + Fa_3 \quad (2.39)$$

The integrated aerodynamic force along  $y_b$  as:

$$Q = Q_1\dot{\beta} + Q_2\beta + Q_3 \quad (2.40)$$

The integrated aerodynamic moment around  $z_b$  as:

$$Na = Na_1\dot{\beta} + Na_2\beta + Na_3 \quad (2.41)$$

## 2.5 Accelerations contributions

In order to define all the accelerations contributions acting on the center of gravity of each blade, the following kinematic equation (in accordance with Ref. [17]) is solved:

$$\vec{a}_h = \vec{a}_{tr} + \vec{a}' + \vec{W}_h \wedge (\vec{W}_h \wedge \vec{r}_{chxb}) + \dot{\vec{W}}_h \wedge \vec{r}_{chxb} + 2\vec{W}_h \wedge \vec{V}' + \vec{g}_h \quad (2.42)$$

In Eq. (2.42) all translational components, relative accelerations, centrifugal and Coriolis components are considered. The vector  $\vec{r}_{chxb}$  is already defined in Eq. (2.9). Instead, the vector containing the rotational rates in the hub reference system remains to be defined as:

$$\vec{W}_h = [p_h, q_h, r_h] \quad (2.43)$$

And the vector containing the rotational accelerations of the body reported in the hub reference system:

$$\dot{\vec{W}}_h = [\dot{p}_h, \dot{q}_h, \dot{r}_h] \quad (2.44)$$

The vector  $\vec{a}_{tr}$ , instead, represent the translational speed variations of the body reported in the hub reference system, and it is expressed as:

$$\vec{a}_{tr} = [\dot{u}_h, \dot{v}_h, \dot{w}_h] \quad (2.45)$$

Moreover,  $\vec{V}'$ , contains the speeds due to the rotation of the blade (speed of a point influenced by the rotation) expressed in the hub reference system, and is calculated as follows:

$$\vec{V}' = [T_{hr}][T_{rb}][0, \Omega(r\cos(\beta) + e), 0] \quad (2.46)$$

Instead,  $\vec{a}'$ , contains the accelerations due to the centripetal component and the  $\dot{\Omega}$  contribution which is still not considered in the model as we assumed to treat a constant rotor speed  $\Omega$ . Again, this vector is oriented in the hub reference system, and is written as:

$$\vec{a}' = [T_{hr}][T_{rb}] \begin{vmatrix} -\Omega^2[e + r\cos(\beta)]\cos(\beta) \\ \dot{\Omega}[e + r\cos(\beta)] \\ \Omega^2[e + r\cos(\beta)]\sin(\beta) \end{vmatrix} \quad (2.47)$$

Finally, it is important to consider also the effects of the gravitational acceleration, that influence also the flapping dynamics. Considering the definition of the gravitational contribution in the body reference system as:

$$\vec{g}_g = \begin{vmatrix} g_0 \sin(\theta) \\ g_0 \cos(\theta) \sin(\phi) \\ g_0 \cos(\theta) \cos(\phi) \end{vmatrix} \quad (2.48)$$

Where  $\phi$  and  $\theta$  in Eq. (2.48) represent the Euler angles useful in that case to consider a different orientation in space between the ground system and the aircraft system, and  $g_0$  on Earth is equal  $9.80665 \text{ m/s}^2$ . Then, to find the contribution due to gravity in the hub reference system the following transformation is used:

$$\vec{g}_h = [T_{hr}][T_{rb}]\vec{g}_g \quad (2.49)$$

The accelerations in the blade system are found summing up all the contributions listed above and switching from the hub system to the blade one:

$$\vec{a}_b = ([T_\beta][T_\phi])^{-1}\vec{a}_h \quad (2.50)$$

## 2.6 Flapping dynamics solution

Before obtaining the aerodynamic contributions, it is necessary to know the values of  $\beta$  and  $\dot{\beta}$ , both included in the definition of aerodynamic incidence. Therefore, in the first place, it is opportune to solve the second order flapping dynamic to know instantaneously the position of each blade in order to project the forces and the moments in the opportune way later on.

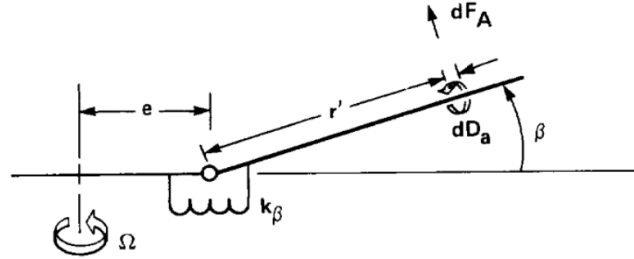


Figure 2.6: Simplified blade flapping sketch

Considering the problem of the second order flapping of the blades where the characteristic equation assumes the form:

$$m\ddot{\beta} + c\dot{\beta} + k\beta = F_\beta \quad (2.51)$$

Therefore, by replacing the inertial and aerodynamic effects for the individual blade is found that:

$$m\ddot{\beta} + c\dot{\beta} + k\beta = (M_1\dot{\beta} + M_2\beta + M_3) - m_b r_{cg}(g_{hz} + a_z) \quad (2.52)$$

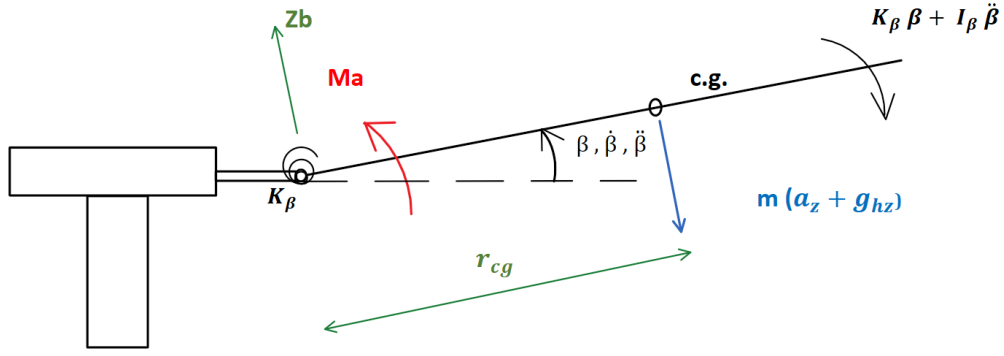


Figure 2.7: Flapping forcing contributions

While for the acceleration, after the simplification of small betas and collecting the terms in  $\beta$  is defined as:

$$a_{zblade} = a_{z1}\beta + a_{z2} \quad (2.53)$$

Where:

$$\begin{aligned} a_{z1} = & -[(p_h^2 - q_h^2)\cos(\psi)^2 - 2\sin(\psi)p_hq_h\cos(\psi) + (q_h + r_h - \Omega)(\Omega + q_h - r_h)]r_{cg} + \\ & + (-p_h^2 + q_h^2)e\cos(\psi)^2 + [2\sin(\psi)ep_hq_h + \dot{u}_h]\cos(\psi) - \dot{v}_h\sin(\psi) + \\ & + e[p_h^2 + (r_h - \Omega)^2] \end{aligned} \quad (2.54)$$

And:

$$\begin{aligned} a_{z2} = & 2r_{cg}(r_h - \Omega)[\cos(\psi)p_h - \sin(\psi)q_h] + \{-e[(2\Omega - r_h)p_h + \dot{q}_h]\cos(\psi) + \\ & - e[(r_h - 2\Omega)q_h + \dot{p}_h]\sin(\psi) - \dot{w}_h\} + \\ & - r_{cg}[(p_hr_h + \dot{q}_h)\cos(\psi) + \sin(\psi)(-q_hr_h + \dot{p}_h)] \end{aligned} \quad (2.55)$$

Replacing the forcing just described in the equation Eq. (2.53) is found that:

$$\begin{aligned} m &= I_\beta \\ c &= -M_1 \\ k &= K_\beta - M_2 + m_b a_{z1} r_{cg} \\ F &= M_3 - m_b a_{z2} r_{cg} - m_b g_{hz} r_{cg} \end{aligned} \quad (2.56)$$

Where in the contributions that force the dynamics there is the independent term of the forcing moment  $M_3$ , previously evaluated in Eq. (2.38), with the gravitational and inertial contributions. While, in the damping term (c) there is the aerodynamic contribution  $M_1$  previously collected, that multiplied  $\dot{\beta}$  always in Eq. (2.38). Instead, the contribution  $M_2$  that is linked to  $\beta$  goes to aggregate in the definition of the mass (k) of the system.

Referring to Eq. (2.56),  $I_\beta$  is the blade's flapping inertia,  $K_\beta$ , the equivalent flapping spring stiffness,  $r_{cg}$ , the distance of the flapping hinge from the center of gravity of the blade,  $m_b$ , the blade mass and  $g_{zh}$  is the gravity contribution. Depending on the type of rotor, these contributions may vary considerably. In fact, for an articulated rotor, ideally the  $K_\beta$ , is close to zero, in fact, the blade should be free from constraints. The situation is completely opposite for a rigid rotor where the stiffness of the equivalent spring rises to truly high values and essentially corresponds to the bending resistance of the material of which the blade is made. Moreover, for the rigid rotor there is no real flapping hinge, then even the position of the offset hinge becomes virtual; and the latter can vary greatly the results in the validation phase. The same applies to the semi-rigid rotor, which also does not have a flap hinge. However, it must be specified that in several cases in the articulated rotor there are also dampers to reduce vibrations and flapping oscillations; these vary the equivalent stiffness value. Naturally, the shape, the dimensions and the material of the blade influence  $I_\beta$  and the mass of the system.

## 2.7 Pitt/Peters Inflow Dynamics

The model elaborated by Pitt and Peters is a three states model of dynamic inflow governed by a differential equation of the first order, where it is assumed the trend of the dimensionless inflow formulated as follows:

$$\lambda = \lambda_0 + \frac{r}{R}\lambda_{1c}\cos(\beta) + \frac{r}{R}\lambda_{1s}\sin(\beta) \quad (2.57)$$

Therefore, in the definition a constant term,  $\lambda_0$  and two periodical contributions,  $\lambda_{1s}$  and  $\lambda_{1c}$ , are considered. However, this particular formulation is not defined directly in  $\lambda$ , but rather in  $\nu$ , in fact, the complete formulation of the Pitt/Peters model is expressed as:

$$\begin{Bmatrix} \dot{\nu}_0 \\ \dot{\nu}_{1s} \\ \dot{\nu}_{1c} \end{Bmatrix} = -[M]^{-1}[L]^{-1} \begin{Bmatrix} \nu_0 \\ \nu_{1s} \\ \nu_{1c} \end{Bmatrix} + [M]^{-1} \begin{Bmatrix} C_t \\ C_{la} \\ C_{ma} \end{Bmatrix}. \quad (2.58)$$

The semi-empirical matrices  $[M]$  and  $[L]$  are respectively the apparent mass matrix and the static gain matrix, as introduced in [5] and reported below in Eq. (2.59) and (2.60). In these formulation ' $\chi$ ' represents the 'wake skew angle', while  $v_m$  and  $v_t$  are the mass flow parameters, functions of the advance ratio and static inflow coefficient. Instead,  $C_t$ ,  $C_l$  and  $C_m$  are respectively the coefficients of thrust, rolling moment and pitching moment of the equivalent rotor disk generated by the rotation of the blades.

$$[M] = \begin{bmatrix} \frac{128}{75\pi} & 0 & 0 \\ 0 & -\frac{16}{45\pi} & 0 \\ 0 & 0 & -\frac{16}{45\pi} \end{bmatrix} \quad (2.59)$$

$$[L] = \begin{bmatrix} \frac{1}{2v_t} & 0 & \frac{15}{64v_m} \tan \frac{\chi}{2} \\ 0 & -\frac{4}{v_m(1+\cos\chi)} & 0 \\ \frac{15}{64v_m} \tan \frac{\chi}{2} & 0 & -\frac{4\cos\chi}{v_m(1+\cos\chi)} \end{bmatrix} \quad (2.60)$$

Where the variables contained in the static gain matrix are:

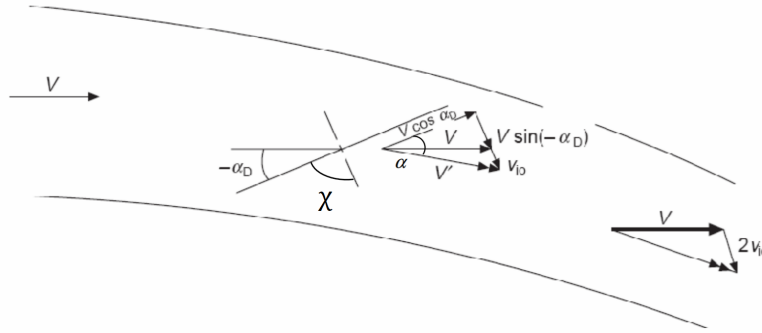


Figure 2.8: Disk rotor inflow sketch

- $$\chi = \arctan\left(\frac{\mu}{\lambda_0 - \mu_z}\right) \quad (2.61)$$

- $$v_t = \sqrt{\mu^2 + (\lambda_0 + \mu_z^2)} \quad (2.62)$$

- $$v_m = \frac{\mu^2 + (\lambda_0 + \mu_z)(2\lambda_0 + \mu_z)}{v_t} \quad (2.63)$$

Where:

- $$\mu_z = \frac{-w_h}{V_{tip}} \quad (2.64)$$

- $$\mu = \frac{\sqrt{u_h^2 + v_h^2}}{V_{tip}} \quad (2.65)$$

In order to connect the variables  $\lambda$  and  $\nu$  the following relations are used:

$$\begin{cases} \nu_0 = \lambda_0 \\ \nu_{1s} = \lambda_{1s}\cos(\beta_h) + \lambda_{1c}\sin(\beta_h) \\ \nu_{1c} = \lambda_{1c}\cos(\beta_h) - \lambda_{1s}\sin(\beta_h) \end{cases} \quad (2.66)$$

Where  $\beta_h = \text{atan}\left(\frac{v_d}{u_d}\right)$  is the side-slip angle of the entire actuator disk system. In order to find the speeds contributions in the disk actuator system, the following transformation matrix is used:

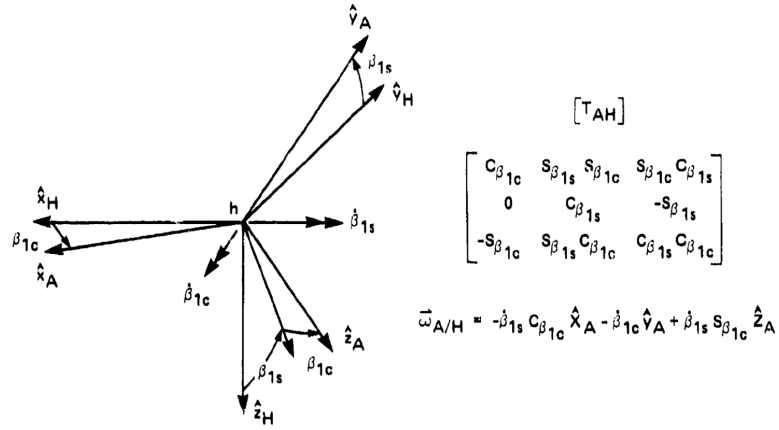


Figure 2.9: Hub-disk reference system transformation

Therefore, after solving the the system of equations in three unknowns, is possible to find:

$$\begin{cases} \lambda_0 = \nu_0 \\ \lambda_{1c} = \nu_{1s} \sin(\beta_h) + \nu_{1c} \cos(\beta_h) \\ \lambda_{1s} = \nu_{1s} \cos(\beta_h) - \nu_{1c} \sin(\beta_h) \end{cases} \quad (2.67)$$

## 2.8 Projection and sum of loads

Once solved the flapping and inflow dynamics, it is possible to focus on the blade and on the hub reference systems in order to sum up all the forces and moments transferred by each blade to the hub and then finding the resulting contributions adding up the effects of each blade.

Once the number of blades is selected by the user, the generic single blade is considered in its starting position,  $\psi_i(t = 0)$ , after which, in order to project the loads in a suitable way, it is necessary to take into account the two characteristic angles that define the position of the blade in time in the hub reference system,  $\psi$  and  $\beta$ , respectively azimuth and flapping angle of the single blade:

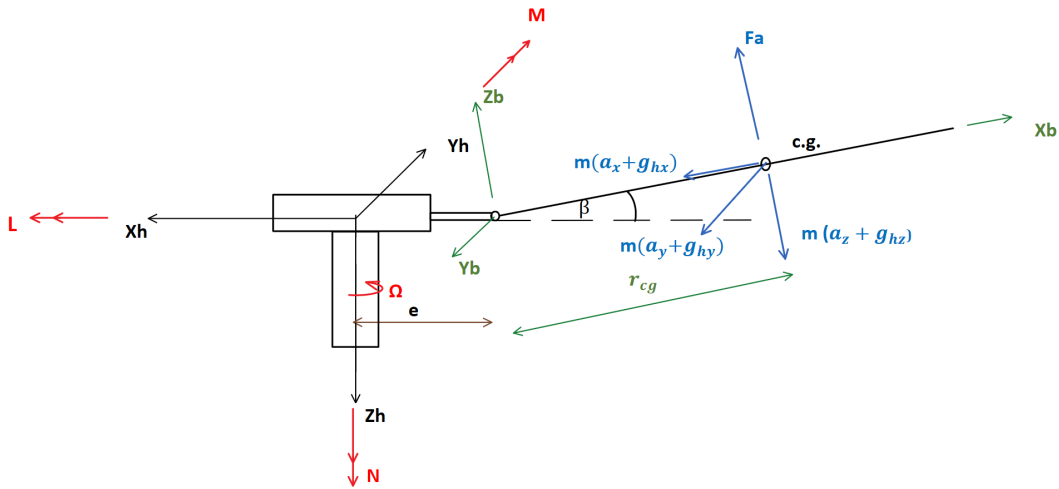


Figure 2.10: Forces and Moments on the single blade

In accordance with the conventions adopted, as shown in the Fig. 2.10, the forces transferred by a single blade to the hub can be expressed as:

$$X_{hi} = (F a_i - m_b a_{zbi}) \sin(\beta_i) \cos(\psi_i) - m_b a_{xbi} \cos(\beta_i) \cos(\psi_i) - (Q_i + m_b a_{ybi}) \sin(\psi_i) + m_b g_{xh} \quad (2.68)$$

$$Y_{hi} = -(F a_i - m_b a_{zbi}) \sin(\beta_i) \sin(\psi_i) - m_b a_{xbi} \cos(\beta_i) \sin(\psi_i) - (Q_i + m_b a_{ybi}) \cos(\psi_i) + m_b g_{yh} \quad (2.69)$$

$$Z_{hi} = -[(F a_i - m_b a_{zbi}) \cos(\beta_i) - m_b a_{xbi} \sin(\beta_i) - m_b g_{zh}] \quad (2.70)$$

Where:

$$\psi_i = \Omega t + \frac{2\pi}{n_b} (i - 1) \quad (2.71)$$

Instead, the moments transferred to the hub by a single blade are defined as:

$$L_{hi} = \sin(\psi_i)[Z_{hi}e - K_\beta\beta_i] - M_{ti}\cos(\psi_i) \quad (2.72)$$

$$M_{hi} = \cos(\psi_i)[Z_{hi}e - K_\beta\beta_i] + M_{ti}\sin(\psi_i) \quad (2.73)$$

$$N_{hi} = Q_i[r_{qi}\cos(\beta_i) + e] + ([T_{br}]_{\vec{a}_{bi}})_y m_b[r_{cg}\cos(\beta_i) + e] \quad (2.74)$$

Where  $r_q$  identifies the radial position of the overall pressure center of the blade, and it is measured as:

$$r_{qi} = \frac{N_{ai}}{Q_i} \quad (2.75)$$

It is possible to calculate the distance in the Eq. (2.75), already having at disposal from the integrals seen above both the aerodynamic moment along z-blade transmitted through the hinge of the single blade ( $N_{ai}$ ), and the aerodynamic force,  $Q_i$ , along the  $y_b$ -axis that generates it.

Instead,  $M_t$  represent an additional contribution due to a torque that arises because of the vertical offset between the center of gravity of the blade and the flapping hinge. It is calculated as:

$$M_{ti} = m_b r_{cg} \sin(\beta_i) (a_{ybi} + \frac{Q_i}{m_b}) \quad (2.76)$$

This moment is transferred through the hinge because of the hypothesis made that the blade is considered free only to flap, while the moments along the axes  $x_b$  and  $z_b$  are bound.

In order to find the overall forces and moments acting on the hub, it is sufficient to add the contributions due to each individual blade:

$$X_h = \sum_{i=1}^{n_b} X_{hi} \quad L_h = \sum_{i=1}^{n_b} L_i \quad (2.77)$$

$$Y_h = \sum_{i=1}^{n_b} Y_{hi} \quad M_h = \sum_{i=1}^{n_b} M_i \quad (2.78)$$

$$Z_h = \sum_{i=1}^{n_b} Z_{hi} \quad N_h = \sum_{i=1}^{n_b} N_i \quad (2.79)$$

## 2.9 Body-Hub moments transportation

Once calculated the stresses acting on the hub it is opportune to find those that are the loads acting on the center of gravity of the aircraft; to realize this, it is necessary to consider the vector that unites center of gravity and the hub of the respective rotor, and then, is also necessary to consider nacelle angles. The reference scheme used for the transportation is reported in Fig. 2.11.

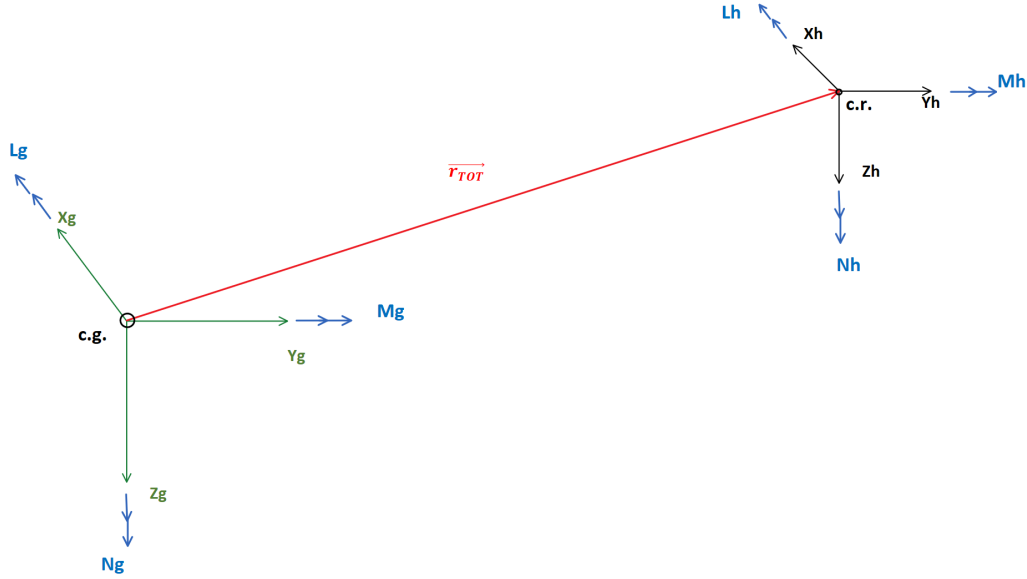


Figure 2.11: Body-Hub transformations

The forces acting on the hub are reported unchanged between the hub and the center of gravity, considering the aircraft as a rigid body. For the moments, instead, it is necessary to take into account those additional moments that arise because of the presence of the arm ( $\vec{r}_{tot}$ ) that connects the forces acting on the hub to the center of gravity. Therefore, once defined  $n_r$ , as the number of rotors present in the aircraft, the moments transmitted to the center of gravity can be made explicit as:

$$L_g = \sum_{i=1}^{n_r} L_{hi} - (\vec{r}_{tot})_{zi} Y_{hi} + (\vec{r}_{tot})_{yi} Z_{hi} \quad (2.80)$$

$$M_g = \sum_{i=1}^{n_r} M_{hi} + (\vec{r}_{tot})_{zi} X_{hi} - (\vec{r}_{tot})_{xi} Z_{hi} \quad (2.81)$$

$$N_g = \sum_{i=1}^{n_r} N_{hi} - (\vec{r}_{tot})_{yi} X_{hi} + (\vec{r}_{tot})_{xi} Y_{hi} \quad (2.82)$$

# Chapter 3

## Implementation of the Rotor Model

### 3.1 Model structure and Time sequence

During the implementation on MATLAB/Simulink<sup>®</sup> the same sequence of operations presented in the mathematical model is maintained:

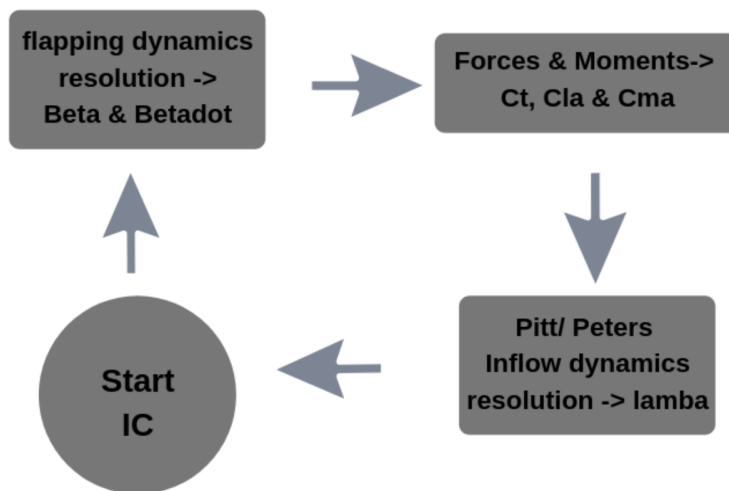


Figure 3.1: Rotor Model resolution flowchart

Once defined the initial conditions, equal to  $2n_b + 3$ :  $\beta$  and  $\dot{\beta}$  for each blade, and the three states of the inflow:  $\lambda_0$ ,  $\lambda_{1s}$  and  $\lambda_{1c}$ . It is opportune to define a sequential logic, in order to make the model work at best. Since the calculation of forces and moments is a function of  $\beta$  and  $\dot{\beta}$  values, it takes place downstream of the resolution of the flapping dynamics. The latter, in turn, is a function of the inflow dynamics, which appears in the definition of the aerodynamic incidence and then in the forcing of the system. Therefore, once known the initial conditions,

it is possible to solve the flapping dynamics, in order to calculate the forces and the moments, and therefore the coefficients  $C_t$ ,  $C_{la}$  and  $C_{ma}$ , that are necessary for the following resolution of the inflow dynamics. All this cycle is repeated for each temporal instant of the simulation in the discrete domain.

It is possible to see how the structure previously presented in the flowchart in Fig. 3.2 is reflected in the implementation in Simulink<sup>®</sup>:

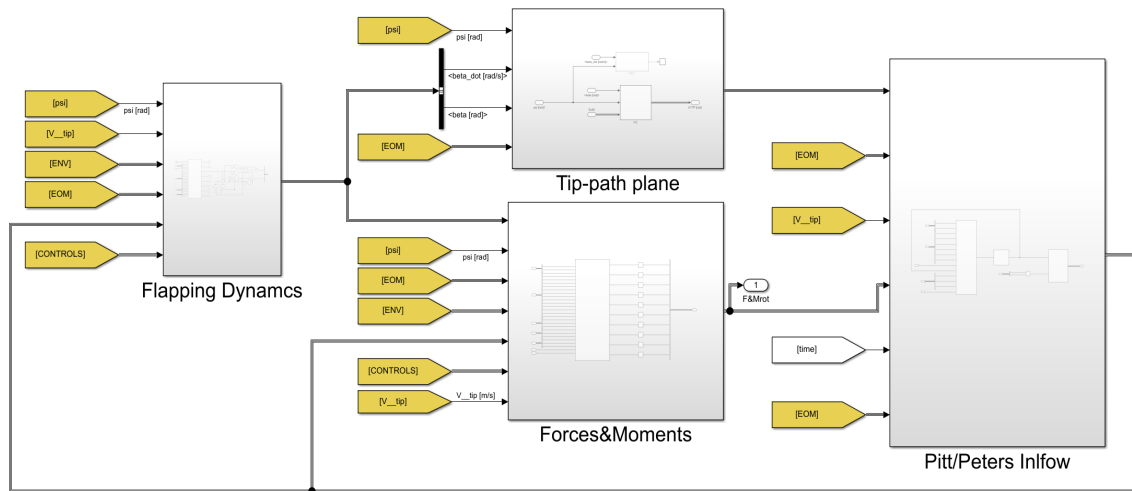


Figure 3.2: Rotor Model Simulink implementation

It is possible to notice the presence of a further block ('Tip-path plane') coming out from the flap block. It deals with mediating the angles of the blades on the round in order to define the mean cyclics flapping:  $\beta_0$ ,  $\beta_{1c}$  and  $\beta_{1s}$  that, according to the approximation of Fourier truncated at the 1st order, make up the relation:

$$\beta(\psi) = \beta_0 + \beta_{1c}\cos(\psi) + \beta_{1s}\sin(\psi) \quad (3.1)$$

$\beta_0$ ,  $\beta_{1c}$  and  $\beta_{1s}$  are useful for the projections from the Hub system to the actuator disk one as seen in Fig. 2.9 used for the resolution of the Inflow dynamic, as shown below.

As seen in the downstream of the rotor block represented in Fig. 3.3, there are conversion blocks useful to pass from the quantities in the center of gravity reference system of the aircraft to the one centered in the hub. While, upstream it is appropriate to have a block that allows to move from the forces and moments at the center of the hub to those directly transmitted to the center of gravity of the aircraft, in order to proceed directly to the resolution of the motion equations of the aircraft considering it as punctual and centered in its center of gravity. The implementation of these blocks is represented in the following figure:

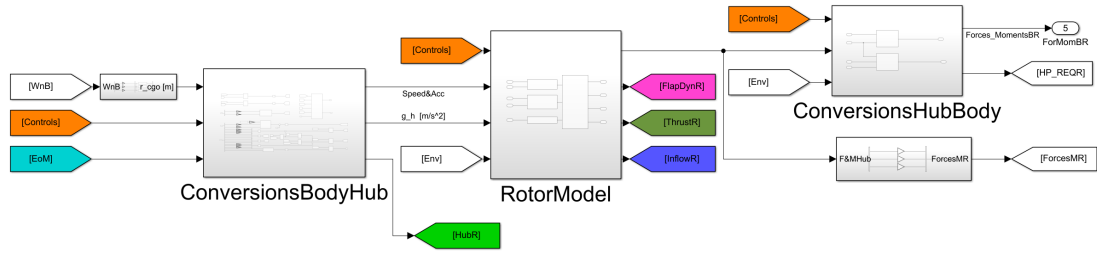


Figure 3.3: Rotor Model and Conversions blocks

## 3.2 Flapping dynamics implementation

Also, the implementation of the flapping dynamics follows the steps set out above in the mathematical treatment. However, it is interesting to see with which method it is chosen to proceed for the integration in time of the second degree dynamics in question. In the first approach, for the temporal integration, a simple method such as the 'forward Euler is adopted; but later, since the results are not satisfactory, for reasons shown below, passing to a higher order method of integration (Tustin) is necessary.

The discrete system that is analyzed in the formulation of the flapping is a dynamic one and, therefore, is described by the following equations:

$$\begin{aligned} \dot{x}(t) &= Ax(t) + Be(t) \\ u(t) &= Cx(t) + De(t) \end{aligned} \quad (3.2)$$

Where the variable  $x(t)$  indicates the states,  $\dot{x}(t)$  its derivative,  $u(t)$  the outputs of the system and  $e(t)$  the inputs. Let  $T$  be the sampling period of the digital control system. By integrating Eq. (3.2) between two sampling times  $kT$  and  $(k+1)T$  is obtained that:

$$x_{k+1} - x_k = A \int_{kT}^{(k+1)T} x(t)dt + B \int_{kT}^{(k+1)T} e(t)dt \quad (3.3)$$

Knowing the values of the integrated function in  $kT$  and  $(k+1)T$ , the integrals in Eq. (3.3) can be approximated using the convex combination:

$$x_{k+1} - x_k = A[(1 - \alpha)x_k + \alpha x_{k+1}]T + B[(1 - \alpha)e_k + \alpha e_{k+1}]T \quad (3.4)$$

Where it is used the approximation:

$$\int_{kT}^{(k+1)T} f(t)dt \simeq [(1 - \alpha)f_k + \alpha f_{k+1}]T \quad (3.5)$$

At the generic sampling time:

$$u_k = Cx_k + De_k \quad (3.6)$$

Adopting the Z-transformed of Eq. (3.4):

$$X(z) = \left[ \frac{1}{T} \frac{z-1}{\alpha z + 1 - \alpha} I - A \right]^{-1} B E(z) \quad (3.7)$$

Then, transforming Eq. (3.6) and exploiting Eq. (3.7) the following bond approximate between the Z-transformed signal input and the Z-transformed of the output is obtained:

$$U(z) = \left\{ C \left[ \frac{1}{T} \frac{z-1}{\alpha z + 1 - \alpha} I - A \right]^{-1} B + D \right\} E(z) \quad (3.8)$$

It follows that Eq. (3.8) can be seen as the transfer function of the continuous time domain  $R_c(s)$  estimated at:

$$s = \frac{1}{T} \frac{z-1}{\alpha z + 1 - \alpha} \quad (3.9)$$

Different approximations are possible depending on the value of  $\alpha$ . The approximations used in practice are:

- Forward Euler:

$$s = \frac{z-1}{T} \quad (3.10)$$

- Backward Euler:

$$s = \frac{z-1}{Tz} \quad (3.11)$$

- Tustin' method:

$$s = \frac{2(z-1)}{T(z+1)} \quad (3.12)$$

### 3.2.1 Forward Euler and Tustin methods

To develop a rotor model as efficient as possible, a comparison is made between two particular methods of integration over time, the Forward Euler and the Tustin method.

To analyze the various methods of integration, in time in this case, passing from the time domain to that of the frequencies is necessary.

Therefore:

$$\begin{cases} x(s) = \mathcal{L}(x(t)) \\ x(s)s^2 = \mathcal{L}(\dot{x}(t)) + IC \end{cases} \quad (3.13)$$

And, then the system of Eq. (2.53) can be written as:

$$x(s^2m + sc + k) = F \quad (3.14)$$

Now it is possible to define the transfer function as:

$$H(s) = \frac{F}{s^2m + sc + k} \quad (3.15)$$

The implementation of the Euler method is simply described by the following image:

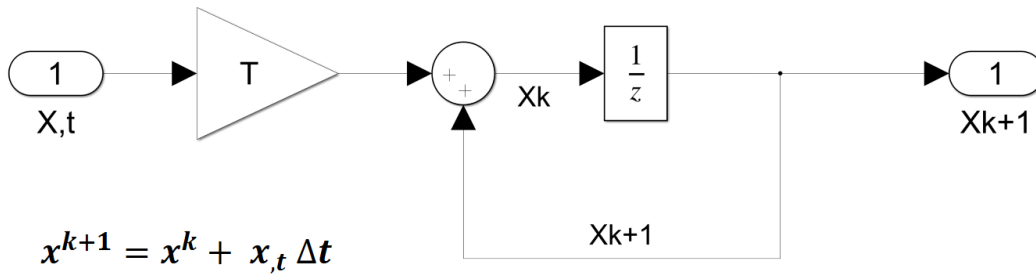


Figure 3.4: Forward Euler scheme

To implement the Tustin' method, instead, it is necessary to replace the Eq. (3.12) in the Eq. (3.15), in order to collect the following formulation:

$$H(s) = \frac{b_0z^2 + b_1z + b_2}{z^2 + a_1z + a_2} \quad (3.16)$$

Then, picking up the terms in the case of Tustin is found that:

$$\begin{aligned} b_0 &= \frac{T^2}{kT^2 + 2cT + 4m} & a_1 &= \frac{-(-2kT^2 + 8m)}{kT^2 + 2cT + 4m} \\ b_1 &= \frac{2T^2}{kT^2 + 2cT + 4m} & a_2 &= \frac{kT^2 - 2cT + 4m}{kT^2 + 2cT + 4m} \\ b_2 &= \frac{T^2}{kT^2 + 2cT + 4m} \end{aligned} \quad (3.17)$$

The reference Tustin' scheme is represented as:

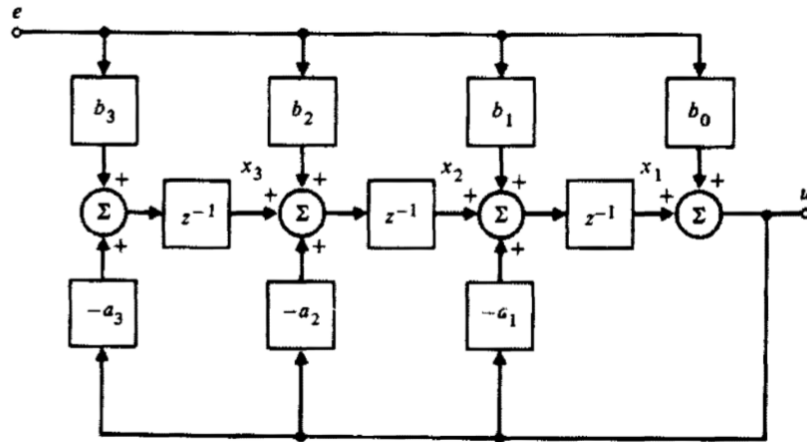


Figure 3.5: Franklin Powell Tustin' method implementation scheme (Ref. [8])

Therefore, the Simulink<sup>®</sup> model for the resolution of the flapping dynamics, is built as follow:

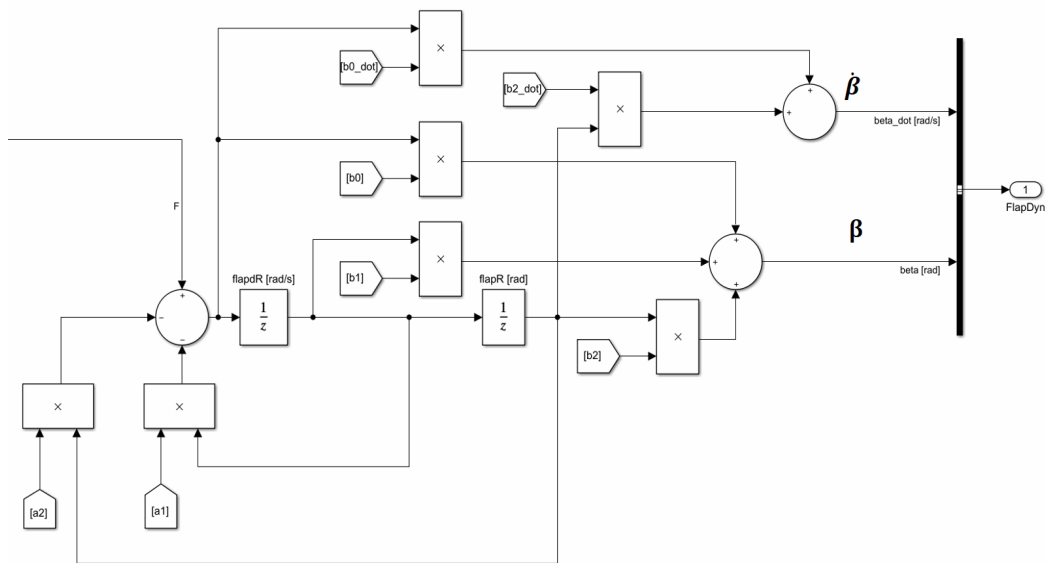


Figure 3.6: Simulink Tustin' implementation for the flapping dynamics

### 3.2.2 Results and conclusions

To compare the results returned by these two different methods, a characteristic condition of the XV-15 aircraft ( $\Omega = 589rpm$ ) is taken: the Hover a sea level in a standard day atmospheric condition.

And the response in terms of flapping of each rotor blade is analyzed. After that, as reference result, the one obtained with a high sampling frequency, 10KHz, with Tustin' method, is assumed. In fact, it is widely considered sufficient to describe this particular dynamics. Then, decreasing the sampling frequency, the following results are obtained.

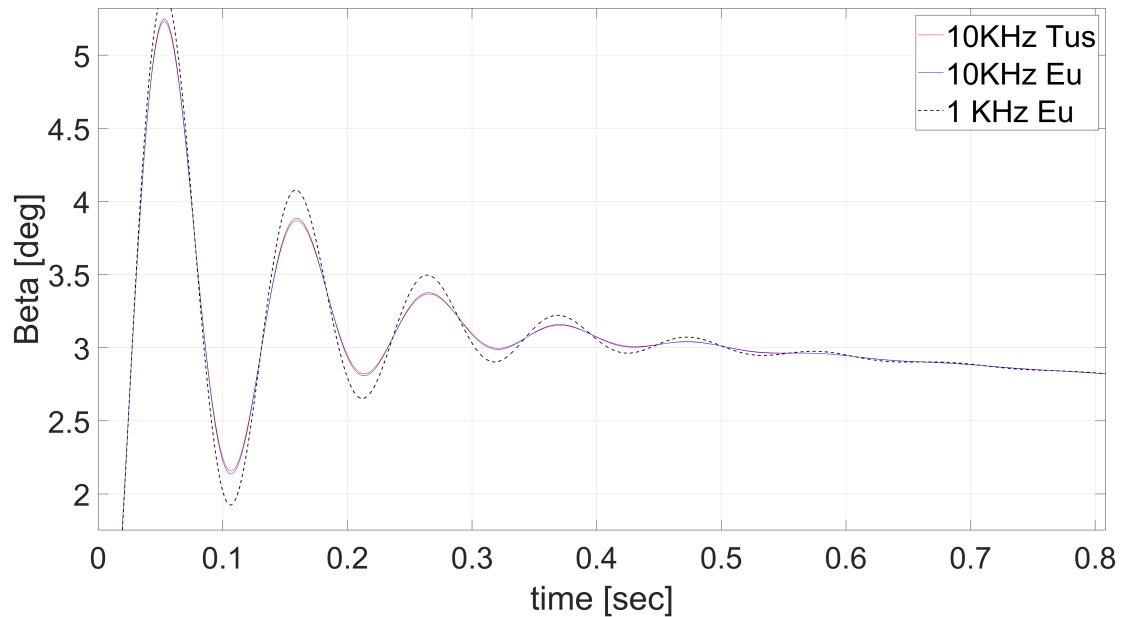


Figure 3.7: 1st comparison Tustin-Euler

In the figure above the trends of the flapping dynamics obtained with 10 KHz of Euler and Tustin, and 1 KHz of Euler are shown. It is possible to see, first of all, that there is only one blade represented, in fact, in this particular condition, the Hover, each blade, once reached the condition of regime, occupies the same position in every instant. For this reason this particular flight condition is chosen, in fact, in that way it is sufficient to represent the performance of a single blade to analyze the behavior of the entire rotor model. Moreover, from the graph above is also possible to notice that the results at 10KHz are perfectly superimposed, and this is a sign that the Euler dynamic at 10 KHz is also representative with this sampling frequency. Finally, it is shown how just by lowering the sampling frequency to 1KHz with the Euler method is already possible to notice a meaningful deviation from the reference dynamic. For this reason, the Euler 1KHz dynamics is not considered reliable and rather onerous from the computational point of view.

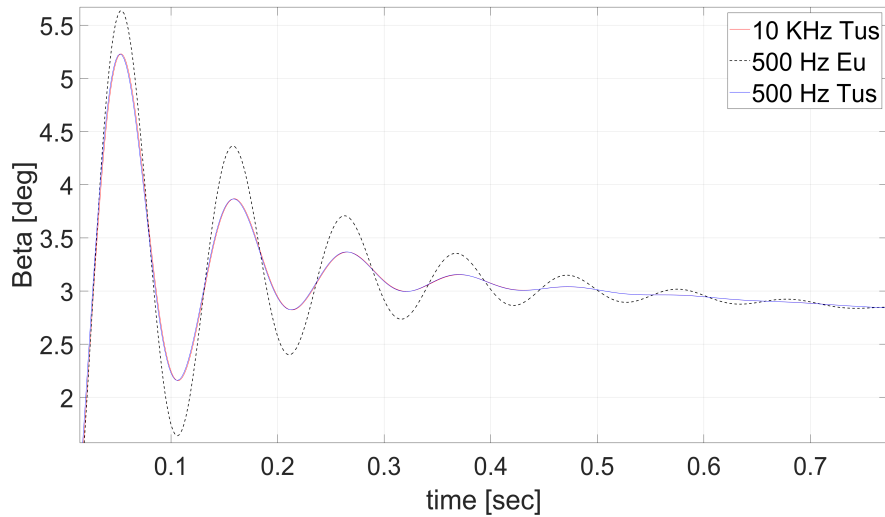


Figure 3.8: 2nd comparison Tustin-Euler

From the figure above, a profound difference between the two methods is already notable. In fact, it is shown that at 500 Hz the Tustin' method still truly faithfully represents the flapping dynamics, superimposing itself on the reference curve. Euler method, on the other hand, demonstrate its weakness by showing oscillations much wider than the real ones. This proves that the dynamics is too fast for this method at 500 Hz.

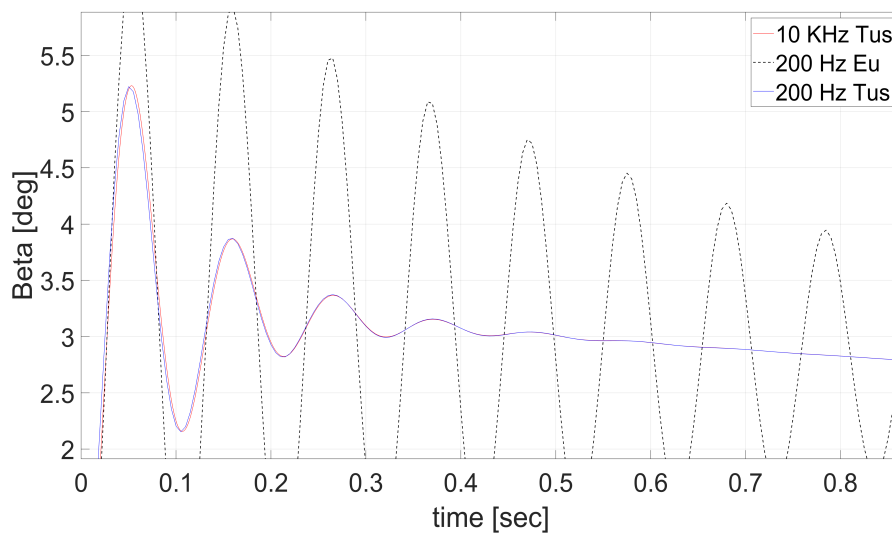


Figure 3.9: 3rd comparison Tustin-Euler

In the figure above it is shown how Tustin' method works surprisingly even at 200 Hz and still almost completely overlaps the reference. This highlights the power of the method. Instead, if the Euler method would be chosen, it may be problematic keeping the real time requirements, because of the aim to faithfully represent the flapping dynamics and therefore solving the other blocks; in fact, truly high sampling rates would be necessary in that case, and the whole code

would be slower.

For these reasons, and especially for the great savings in computational terms, it is decided to use and implement the method of Tustin in the model.

Proof of this can be shown considering a dynamic system of the classical second order not forced governed by the equation:

$$\ddot{\beta} + 2\zeta w_n \dot{\beta} + w_n^2 \beta = 0 \quad (3.18)$$

Moving to the frequency domain, replacing the appropriate transfer functions for Euler and Tustin of Eq. (3.10) and (3.12), and then with solving in 'z' the equation of second degree for a wide range of frequencies is found that:

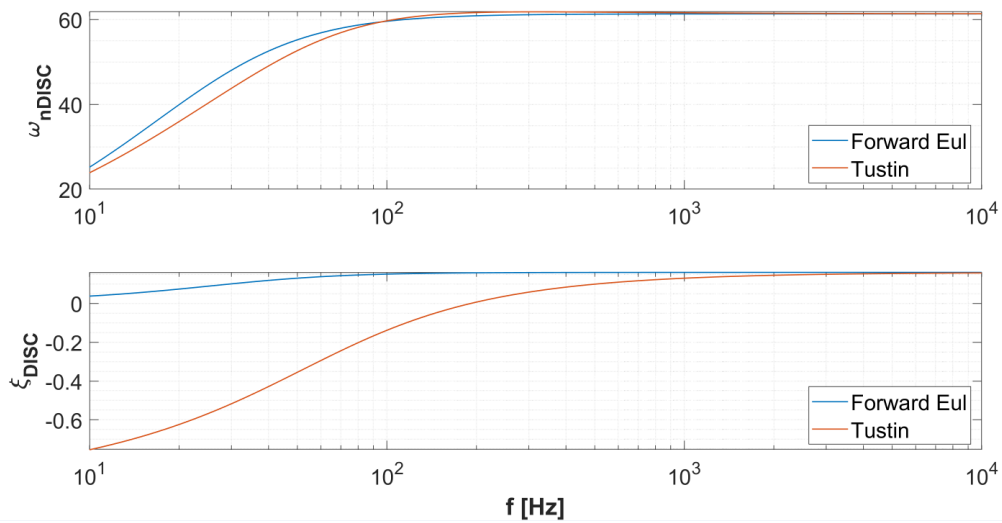


Figure 3.10: Forward Euler-Tustin  $w_n$  and  $\zeta$  comparison

From the figure above it is possible to notice, once again, the substantial difference between the two methods. In fact, it is possible to see that when the sampling frequency decreases, the Euler method shows a much lower damping than the reference one observed for the reference frequency at 10KHz, therefore, the amplified oscillations previously observed are triggered. Tustin' method, instead, up to 200 Hz remains faithful to the real dynamics, and then it appears a consistent error but always considerably less than the one obtained with the Euler method. However, it is interesting to note, that a sampling rate of 100 Hz would still not be sufficient even with the Tustin' method. In fact, in the upper graph it is shown that, although the  $w_n$  of the system is still well represented, the damping is not, and there is a risk to find a solution not faithful to reality. Therefore, a sample time of at least 200 Hz (the one adopted) is necessary to have a reliable solution and at the same time a computational efficient model.

In order to find the damping for this type of dynamic system, useful to process the previous graph, is possible to proceed graphically:

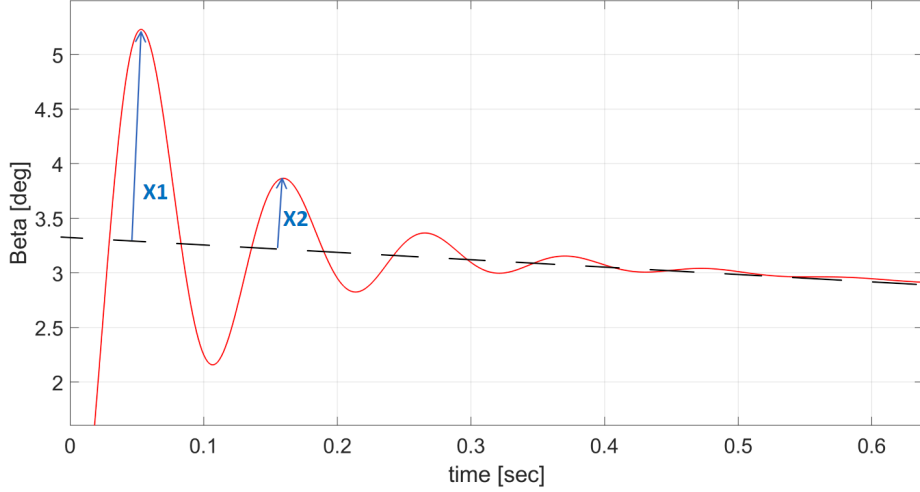


Figure 3.11: XV-15 Hover flapping dynamics ( $\Omega = 589rpm$ , Sea Level)

Where:

$$\sigma = -\frac{\ln(X_1/X_2)}{T_2 - T_1} \quad \text{and} \quad \sigma = -\zeta w_n \quad (3.19)$$

Once found  $\sigma$ ,  $\zeta$  can be derived by the simple relationship:

$$\zeta = \sqrt{\frac{1}{\frac{w^2}{\sigma^2} + 1}} \quad (3.20)$$

And therefore:

$$w_n = \frac{w}{\sqrt{1 - \zeta^2}} \quad (3.21)$$

Where  $w = \Omega = 589 \text{ rpm}$ . Therefore, collecting this data for the comparison between Tustin and Euler seen above is found that:

Case	$X_1[rd]$	$X_2[rd]$	$T_1[s]$	$T_2[s]$	$w[rd/s]$	$f[Hz]$	$\sigma[-]$	$\zeta[-]$
10KHz (Tus)	0.374	0.138	0.1553	0.2577	61.359	9.766	-9.736	0.157
1KHz (Eu)	0.494	0.219	0.1550	0.2570	61.600	9.800	-7.975	0.128
500Hz (Eu)	0.671	0.365	0.1540	0.2560	61.600	9.800	-5.969	0.097

Table 3.1: 10KHz (Tus), 1KHz (Eu) and 500Hz (Eu) data comparison

It is possible to notice how from considering data related to the forward Euler emerges that the dimensionless reference damping for the case analyzed of Hover is equal to 0.15672 and, by reducing the sampling frequency, the results of the same parameter vary greatly proving what saw previously.

### 3.3 Aerodynamic implementation

In order to implement a complete rotor model, it is advisable to enter the data concerning the complete aerodynamic polar. In fact, during the rotation, the blade, near the root finds incidences even close to  $90^\circ$  as the tangential speed can be almost zero. Moreover, during the advancement phase it is possible to have some points of the blade where the speed imposed by the  $\Omega$  angular rate is cancelled by the component due to the translation ( $u_h$  and  $v_h$ ) of the aircraft. Therefore, in these points it is necessary to have aerodynamic values of the blade not included in the canonical linear tract of the aerodynamic polar, usually defined between  $-20^\circ$  and  $20^\circ$ . For these reasons, it is necessary to extend the profile aerodynamic, and to realize it the approximation of Hoerner is chosen, as announced before (Ref. [13]).

#### 3.3.1 XV-15 Aerodynamics

The characteristic aerodynamic profile of XV-15 rotor blades is the NACA 64-208:

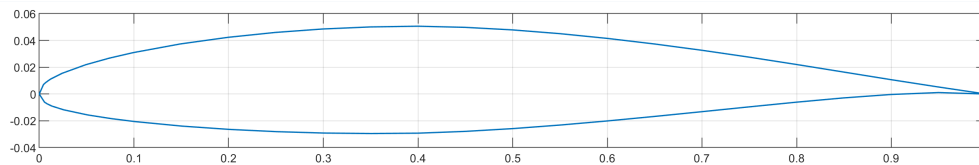


Figure 3.12: NACA 64-208, XV-15 aerodynamic profile

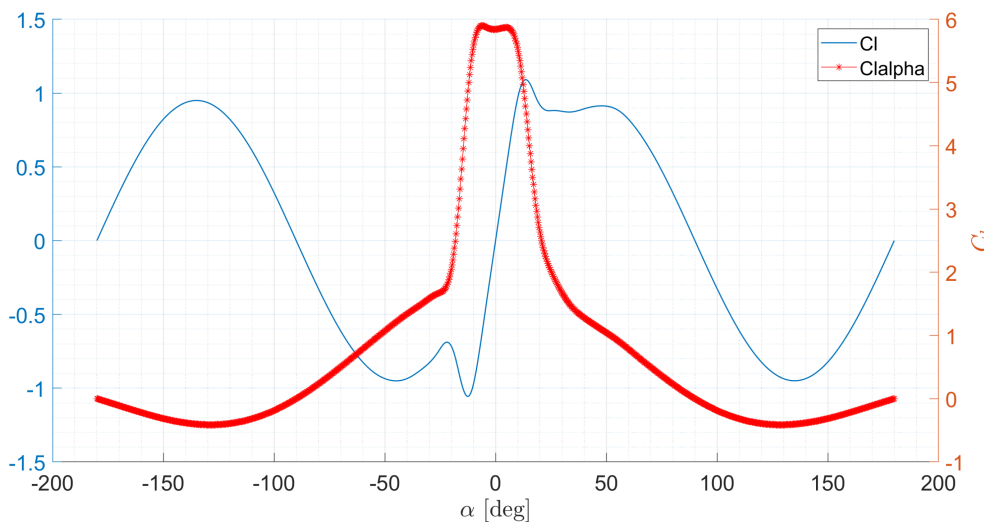


Figure 3.13:  $C_l$ - $\alpha$  NACA 64-208, XV-15

In the figure above two curves are represented: that of the  $Cl$  and that of the  $Cl_\alpha$ . In the definition of aerodynamic contributions, the  $Cl$ , in the mathematical treatment is expressed as:

$$Cl = Cl_\alpha(\alpha - \alpha_0) \quad (3.22)$$

The  $Cl_\alpha$  therefore, instead of representing the real derivative and therefore the slope of the curve, consists in a gain of  $Cl$  with respect to the incidence of zero lift (in this case,  $\alpha_0 = -1^\circ$ ). Its trend is the one described by the dotted curve; while the other curve represents the trend of the  $Cl$ . In the latter, is possible to distinguish the classic linear tract around reduced incidences, followed by the stall; and then, because of Hoerner' assumptions (hypothesis of flat plate), the curve assumes the trend defined by the functions:

$$\begin{aligned} Cl_+ &= k_{Cl+} \sin(\alpha) \cos(\alpha) \\ Cl_- &= k_{Cl-} \sin(\alpha) \cos(\alpha) \end{aligned} \quad (3.23)$$

Where  $Cl_+$  and  $Cl_-$  are respectively the functions that describe the previous and the next traits to the linear tract. While  $k_+$  and  $k_-$  are chosen according to the type of profile analyzed. In this case it is used:

$$k_{Cl+} = k_{Cl-} = 1.9 \quad (3.24)$$

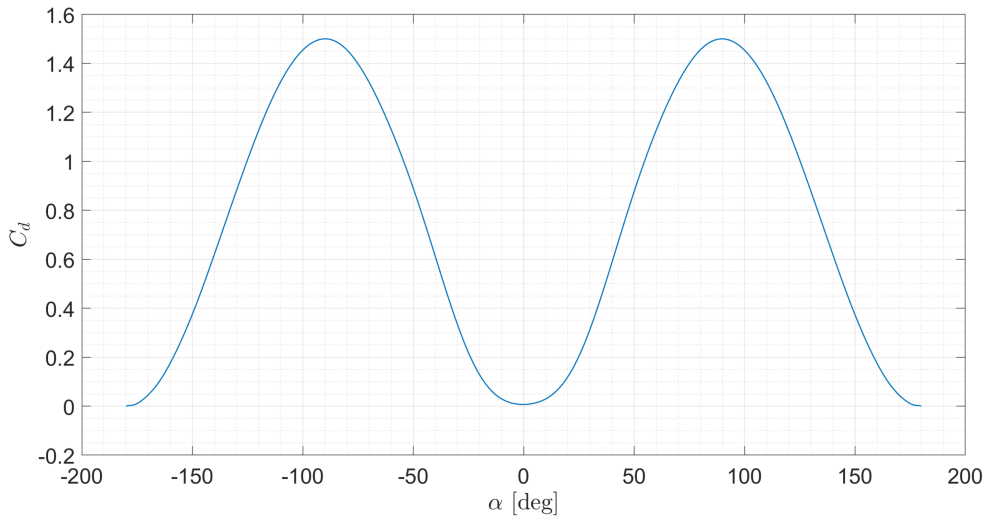


Figure 3.14:  $C_d$ - $\alpha$  NACA 64-208, XV-15

Instead, for the trend of  $C_d$ , represented in the figure above, the classic parabolic trait in the values of reduced incidences is notable. Once out of this field of incidence, it is evident that there is a sudden increase in the  $C_d$  up to a maximum recorded at  $\alpha = 90^\circ$  where the profile exposes its maximum frontal section to the flow. The Hoerner' function used to describe the  $C_d$  trend is:

$$\begin{aligned} Cd_+ &= k_{Cd+} \sin(\alpha)^2 \\ Cd_- &= k_{Cd-} \sin(\alpha)^2 \end{aligned} \quad (3.25)$$

Where, in that case:

$$k_{Cd+} = k_{Cd-} = 1.5 \quad (3.26)$$

### 3.3.2 UH-60 Aerodynamics

As far as the aerodynamics of the other aircraft used to validate the model is concerned; the UH-60, own the SC 1095 as blade's characteristic profile, for which  $\alpha_0 = -1.125^\circ$ . It shows the following shape:

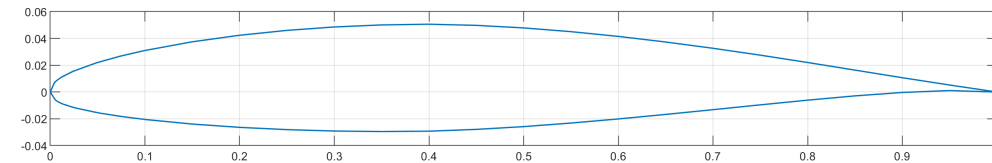


Figure 3.15: SC 1095, UH-60 aerodynamic profile

In that case the following performances are obtained:

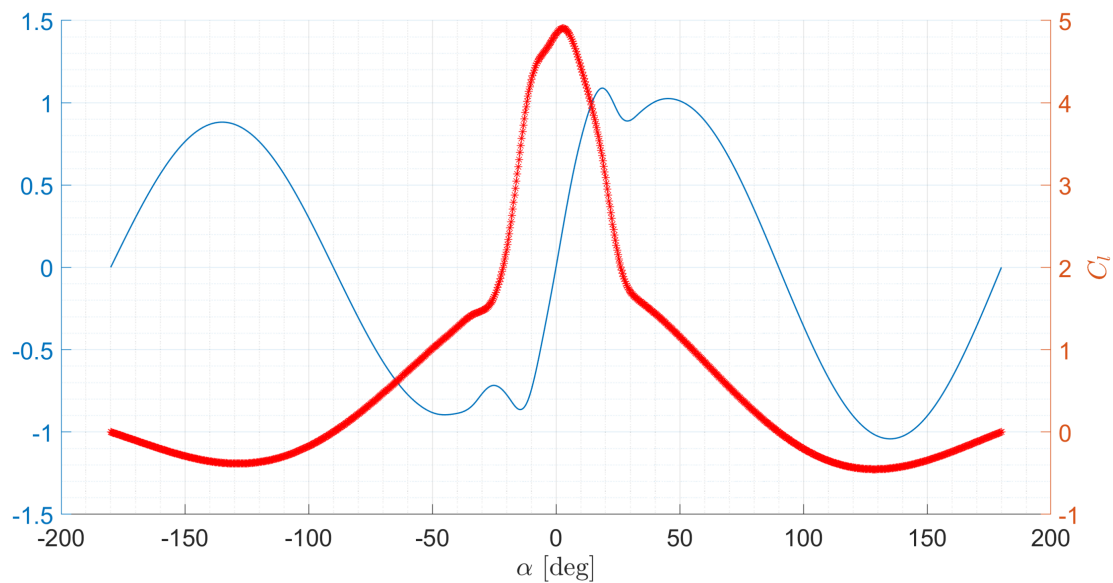


Figure 3.16:  $Cl-\alpha$  SC-1095, UH-60

Where:

$$\begin{aligned} k_{Cl+} &= 3 \\ k_{Cl-} &= 2.5 \end{aligned} \quad (3.27)$$

Instead, for the drag coefficient,  $Cd$ , the following trend is found:

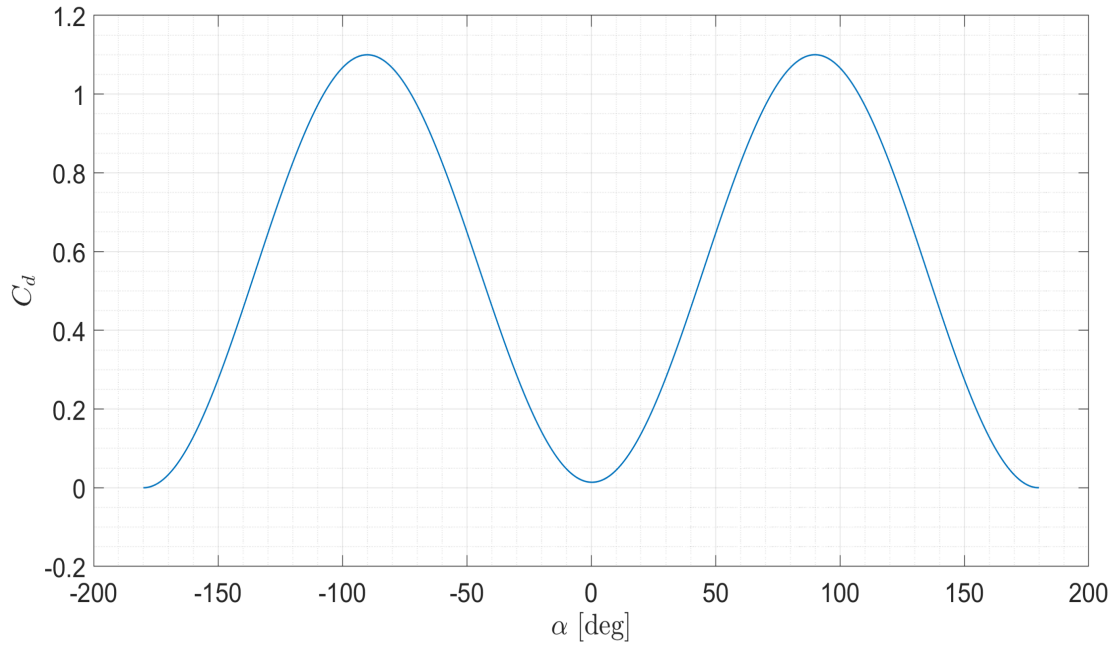


Figure 3.17:  $C_d$ - $\alpha$  SC-1095, UH-60

Where:

$$k_{C_{d+}} = k_{C_{d-}} = 1.1 \quad (3.28)$$

### 3.4 Tip loss and Mach correction Factors

To complete the discussion on lift and drag coefficients the effects of losses at the tip and the effects due to Mach number must also be considered. To simplify the treatment and not slowing down the code, it is decided to use general polynomial laws considered valid for each type of aerodynamic profile and for each type of blade. These laws are simply represented by corrective factors, which, depending on the radial position of the station analyzed or on the Mach acting on that station, apply a corrective coefficient to the parameter in question.

From the figure below is possible to see the first meaningful correction that takes place within the model to all those aerodynamic forces integrated and evaluated along the blade. These, in fact, approaching toward the tip of the blade are affected by the effects of extremities of all the lifting surfaces. In the final sections, therefore, it is necessary to take into account these phenomena. To describe these losses, multiplicative factors are used; these varies along the opening of the blade with the trends represented in the following images. Every curve is represented in a dimensionless form so that it can be applied to each type of blade. It is notable that at the tip of the blade the multiplicative tip loss coefficient is zero. In fact, at the tip of the blade where the loss effects are truly intense, all the aerodynamic forces are brought around zero, as reported in Ref. [18].

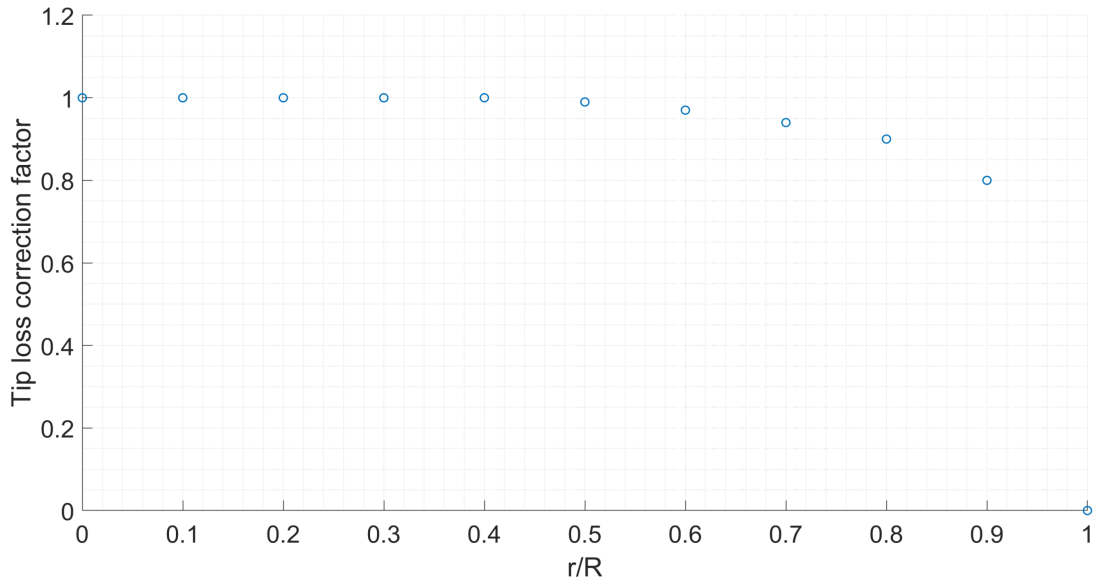


Figure 3.18: Tip Loss Factor Law

From the following figures, instead, it is possible to observe the trend of the correction factors with Mach. In fact, it is known that when this parameter changes, the lifting and drag coefficient changes considerably. Also, a reference dimensionless curve is used, which represent a generic correction in accordance with the trends found in Ref. [20].

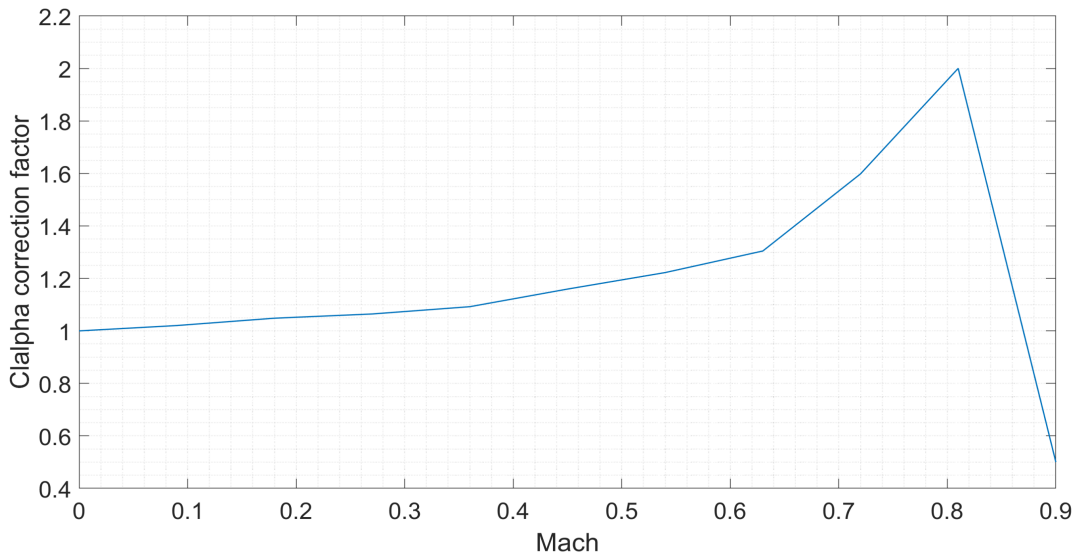


Figure 3.19:  $Cl_\alpha$  Mach correction factor

As far as the drag coefficient is concerned, the correction represented by the following graph is used. In fact, it undergoes a sudden increase for Mach numbers higher than the Drag Rise value. As it is possible to notice from the trend the

$Cd_0$  is unaltered until the equal Mach number is inferior to 0.70-0.72, in accord to Ref. [20].

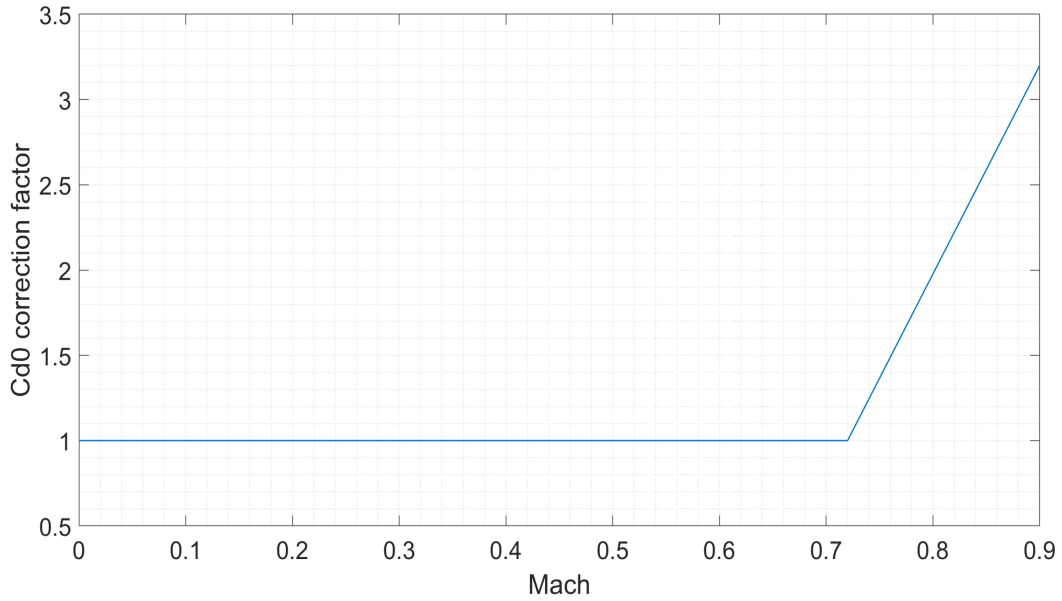


Figure 3.20:  $Cd_0$  correction factor

### 3.5 Multiblade trasformation

To obtain the angles on which the whole disk is oriented, useful for defining the rotation matrix indicated in Fig. 2.9 , it is necessary to define the coefficients of the Fourier transform truncated at the first order. As announced before, this development is defined as:

$$\beta(\psi) = \beta_0 + \beta_{1s}\sin(\psi) + \beta_{1c}\cos(\psi) \quad (3.29)$$

In order to find the Fourier coefficients in question, the following equations need to be solved:

$$\begin{aligned} \beta_0 &= \frac{1}{\pi} \int_{-\pi}^{\pi} \beta(\psi) d\psi \\ \beta_{1s} &= \frac{1}{\pi} \int_{-\pi}^{\pi} \beta(\psi) \cos(\psi) d\psi \\ \beta_{1c} &= \frac{1}{\pi} \int_{-\pi}^{\pi} \beta(\psi) \sin(\psi) d\psi \end{aligned} \quad (3.30)$$

These formulations in the discrete become:

$$\begin{aligned}\beta_0 &= \frac{1}{Tn_b} \sum_{i=1}^N \beta_i \Delta T \\ \beta_{1s} &= \frac{2}{Tn_b} \sum_{i=1}^N \beta_i \sin(\psi_i) \Delta T \\ \beta_{1c} &= \frac{2}{Tn_b} \sum_{i=1}^N \beta_i \cos(\psi_i) \Delta T\end{aligned}\quad (3.31)$$

Where N is the number of points evaluated for each blade in a round time. For example at a sample time of  $f = 1\text{KHz}$ , with a round angular speed of  $589\text{rpm} = 61.68\text{rad/s}$  is found that:

$$\begin{aligned}t_{\text{round}} &= \frac{2\pi}{\Omega} = 0.1019\text{s} \\ N &= t_{\text{round}} f = 101.9\end{aligned}\quad (3.32)$$

### 3.5.1 Simulink<sup>®</sup> implementation

To implement this scheme on Simulink<sup>®</sup> a vector of the maximum size predefined previously is created, that accumulates the values of betas along the round. Naturally, this vector at the end of each lap is overwritten for the next calculation. The structure implemented is the following:

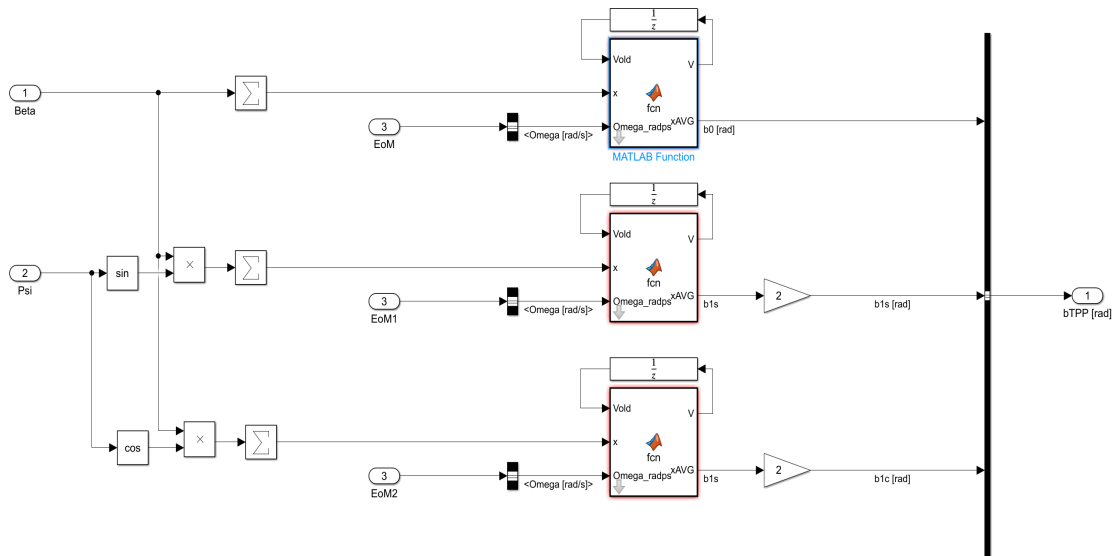


Figure 3.21: Multiblade transformation Simulink<sup>®</sup> structure

Above it is shown in detail how the delay continuously sum up the contribution of each blade. What is more, in the Matlab<sup>®</sup> function is contained the operation of overwriting for each element of the vector:

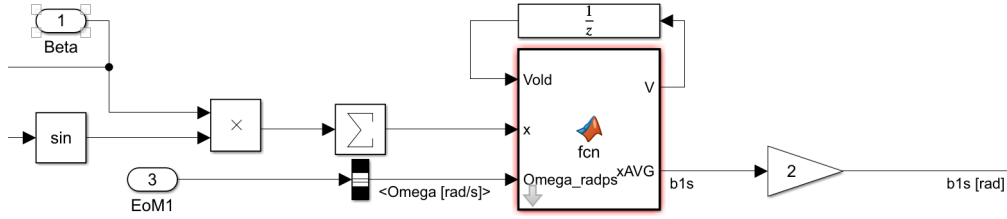


Figure 3.22: Multiblade transformation Simulink<sup>®</sup> structure detail

In this case,  $N=128$  as the maximum size of the vector is adopted, that for  $\Omega = 589rpm$  and for a sampling frequency of  $200Hz$  (the one chosen to adopt, being satisfactory with Tustin as demonstrated above). Moreover, in order to face higher rotational speeds like those of the turboprop, it is sufficient to increase the maximum size in the initialization file.

### 3.5.2 Results

Once the coefficients are found, it is possible to verify the functionality of the implementation by comparing the real trend of the flapping dynamics of the blade with the one extracted from the approximation of Fourier of Eq. (3.29). During this test both XV-15 rotors, left and right, are analyzed. The flight conditions chosen to conduct this particular test is the following:

$$\begin{aligned}
 \Omega &= 589 \quad [rpm] \\
 u_h &= 30 \quad [m/s] \\
 v_h &= w_h = p_h = q_h = r_h = 0 \\
 \dot{u}_h &= \dot{v}_h = \dot{w}_h = \dot{q}_h = \dot{p}_h = \dot{r}_h = 0 \\
 \rho &= 1.225 \quad [kg/m^3] \\
 T &= 288.15 \quad [k]
 \end{aligned} \tag{3.33}$$

And the following controls are applied:

$$\begin{aligned}
 \theta_0 &= 6 \quad [deg] \\
 A1 &= 0 \quad [deg] \\
 B1 &= 4 \quad [deg]
 \end{aligned} \tag{3.34}$$

For this test the single rotor as isolated is considered, in a similar way to what is done in a test rig by providing him with inputs and monitoring its outputs. In particular, it is interesting to monitor the trend of the flapping angle for any blade, and then comparing it with the trend proposed by Fourier, in order to be able to understand if the average angles on the lap are correct and reliable.

Therefore, the following results are found:

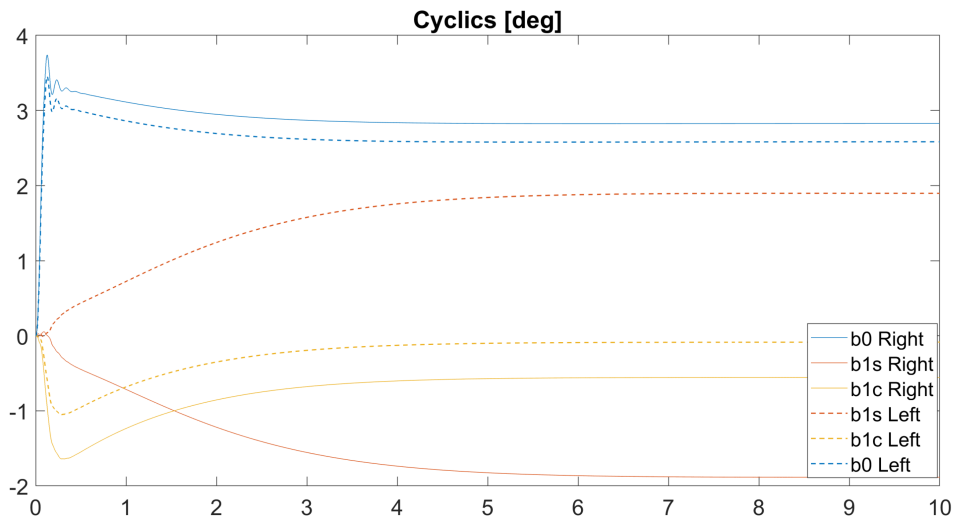


Figure 3.23: Multiblade transformation coefficients

From figure above is possible to see the parameters obtained with the Fourier approximation for both rotors of XV-15.

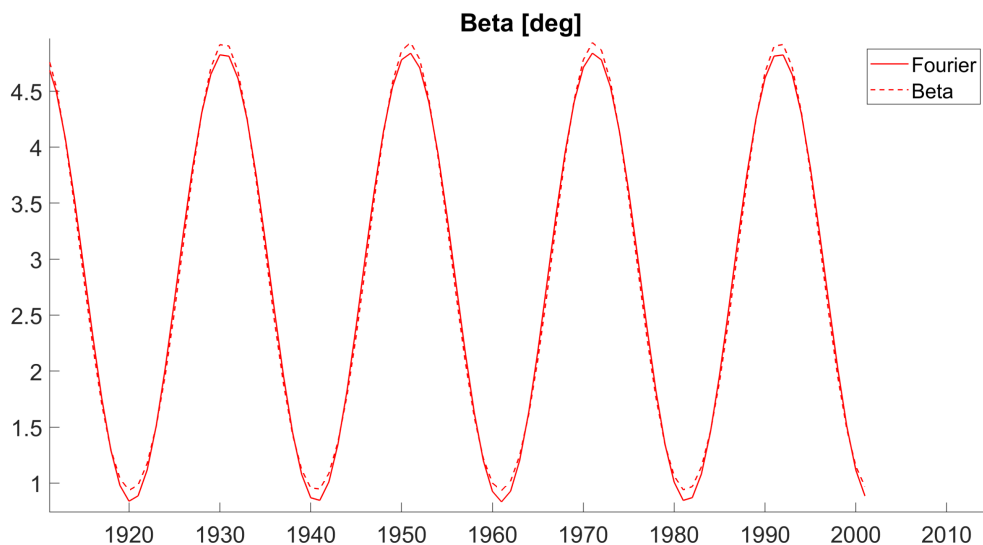


Figure 3.24: Multiblade transformation comparison

Instead, from the previous figure is possible to notice how the trends of the Fourier transform of Eq. (3.29) and the real flapping are practically superimposed. This proves that the transform coefficients are correctly obtained, and therefore, they can now be adopted for the disk orientation required in the rotor model implementation.

# Chapter 4

## Results and Validation

### 4.1 XV-15 test and validation

#### 4.1.1 Rotor inputs

In order to use the rotor model, it is necessary to insert in the initialization file not only the aerodynamic data relative to the characteristic profile of the blade, shown in the aerodynamic section, but also all those values useful to define the mathematical model, in accord to Ref. [6] and [7]. In particular, for this aircraft the following twist law is adopted:

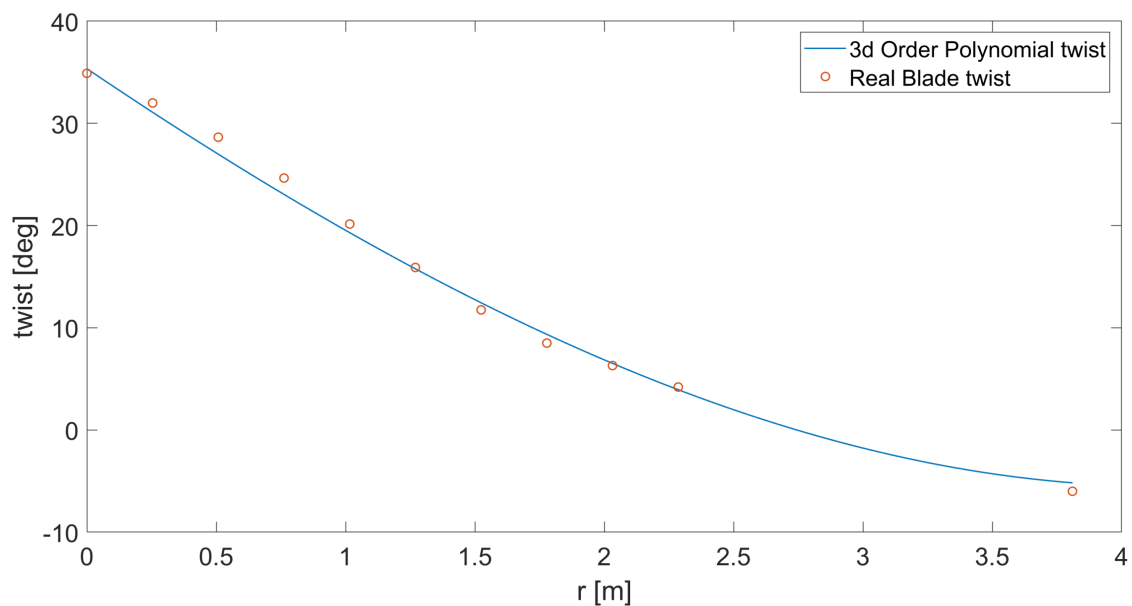


Figure 4.1: XV-15 Blade twist

Where the polynomial coefficients are:

$$\begin{aligned}
 t_3 &= 0.0084 \quad [rad/r^3]; \\
 t_2 &= -0.0136 \quad [rad/r^2]; \\
 t_1 &= -0.2608 \quad [rad/r]; \\
 t_0 &= 0.7260 \quad [rad];
 \end{aligned}
 \tag{4.1}$$

Instead, for the taper law, a constant value is considered for the entire blade, in fact, for tilt-rotors, it is truly common not to find a tapering. Therefore:

$$\begin{aligned}
 c_3 &= c_2 = c_1 = 0.0; \\
 c_0 &= 0.3556 \quad [m];
 \end{aligned}
 \tag{4.2}$$

While the remaining parameters useful to define the XV-15's rotor are:

$$\begin{aligned}
 I_\beta &= 138.97 \quad [kgm^2] \\
 M_\beta &= 76.9 \quad [kgm] \\
 m_b &= 40.37 \quad [kg] \\
 n_b &= 3 \quad [n/d] \\
 r_{cg} &= M_\beta/m_b = 1.905 \quad [m] \\
 K_1 &= -\tan(\delta_3) = -0.2679 \quad [n/d] \\
 e &= 0 \quad [m] \\
 K_\beta &= 1.7504e + 04 \quad [Nm/rad] \\
 R &= 3.14 \quad [m]
 \end{aligned}
 \tag{4.3}$$

#### 4.1.2 Results and validation



Figure 4.2: XV-15 rotor in Langley test center

In this case, the reference data set is derived from a series of experimental tests conducted at the NASA Langley Research Center on several prop-rotor designs, as reported by Harris in [12]. Precisely, the original layout of the XV-15 is considered, also in accordance with the reference data found in [6] and used for the development of the overall tilt-rotor simulation model. Among what provided in [12], all reference data are selected at equal Mach Number measured at the Blades' tip ( $M_{tip}$ ), in environmental conditions referred to sea level on a standard day. As shown below, both coefficients of thrust and power predicted by the model match the reference data for the hover condition with a rather meaningful degree of fidelity. To validate the model, the characteristic parameters of each rotor are studied. In particular, it is analyzed how the traction coefficient, the power coefficient and the figure of merit vary with the collective, in order to realize a complete comparison with the data provided by NASA.

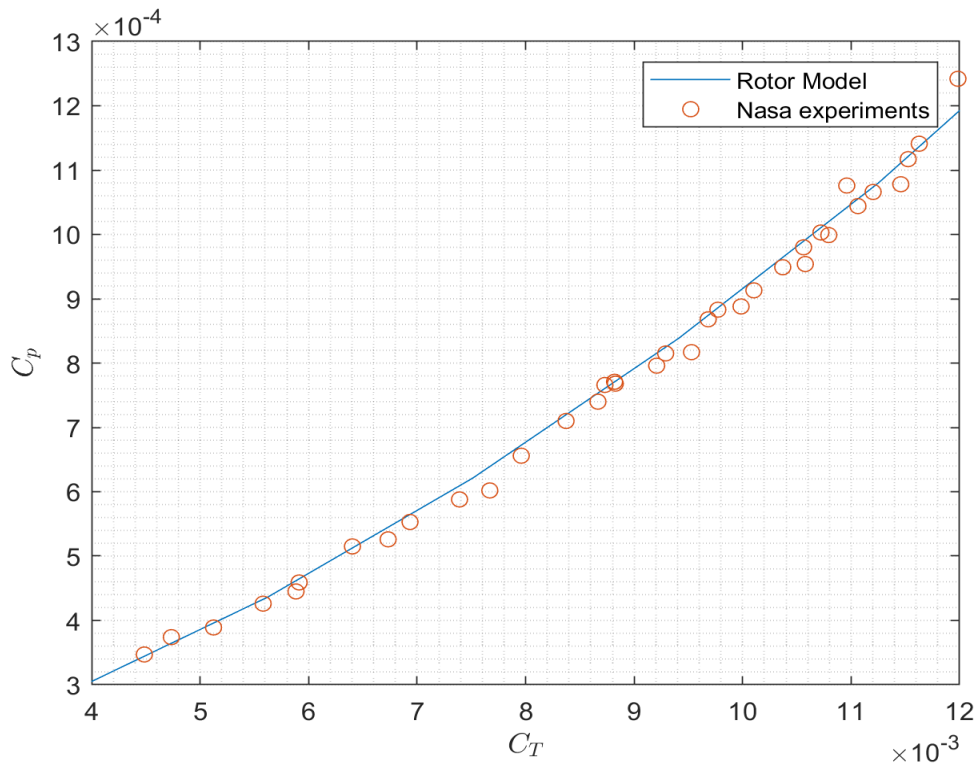


Figure 4.3: XV-15 rotor  $C_p$ - $C_t$  curve in Hover conditions

From the figure above, it can be seen that the power levels are satisfactorily respected by the rotor model as the traction coefficient increases. In fact, it is shown how the continuous line, that represents the results returned by the rotor model, rather faithfully superimposes its trend to the one of the experimental data represented by the circular points. This is closely related to the aerodynamic values entered in the initialization file, treated and shown previously in the aerodynamic section. In fact, the power coefficient is nothing more than a value

connected to drag (and therefore the  $C_d$ ) acting on each section of the blade. Instead, the traction coefficient is closely linked to the lifting capacity coefficient ( $Cl$ ). Since each blade is divided into a substantial number of stations (15 in that particular case), and each of them can be subject to a truly variable aerodynamic incidence depending its azimuth position and on the flight condition, it can be easily understood that it is extremely important to define precisely and consistently the trends of the aerodynamic coefficients with the incidence. Otherwise, it would not be possible to obtain a result faithful to reality.

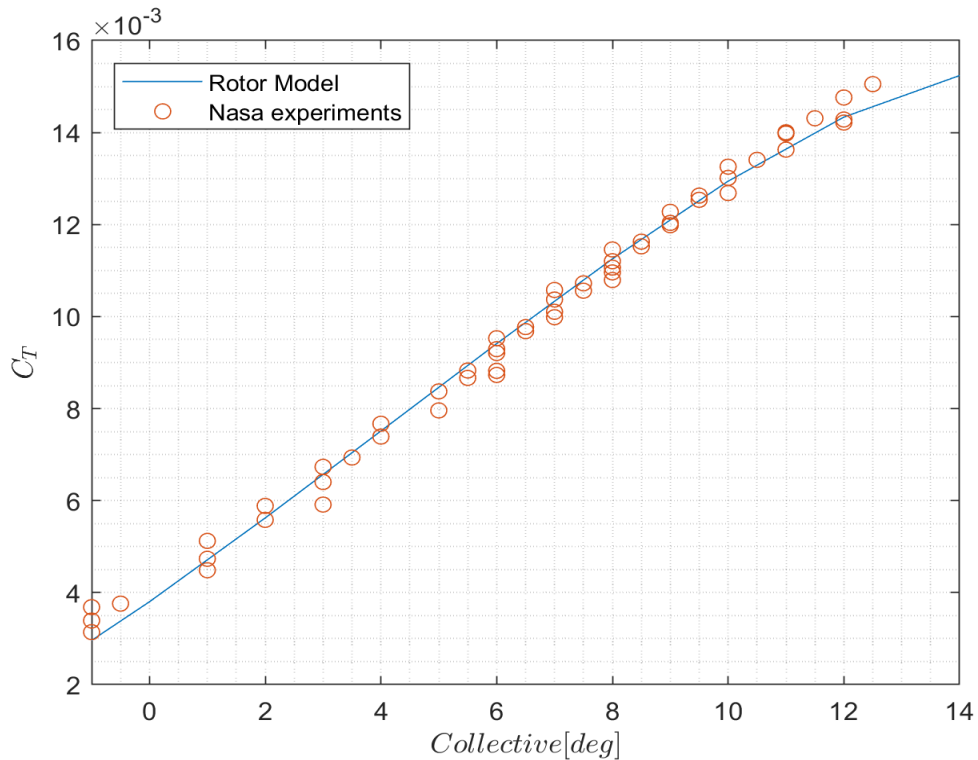


Figure 4.4: XV-15 Ct-Collective curves in Hover conditions

From the figure above it is possible to see another meaningful response of the rotor, that is the variation of the traction coefficient with the collective.

Again, it is shown how the trend predicted by the rotor model follows the experimental results of NASA. This result, is truly important for the purpose of truthfulness of the model in question, in fact, if there was no such correspondence, a possible test pilot trying the flight simulator would find levels of traction truly different from those expected and it could be difficult for him to fly the machine, not to mention that the model would not be representative.

In the following image, instead, it is shown the trend of the figure of merit as a function of the collective scaled for the solidity of the rotor. The figure of merit is a number used to calculate the performance or the actual efficiency of a rotor, and is defined as:

$$FM = \frac{C_{p_{id}}}{C_p} \quad (4.4)$$

Where:

$$C_{p_{id}} = \sqrt{\frac{Ct^3}{2}} \quad (4.5)$$

The optimal Figure of Merit's value for a rotor should be equal to one, but this value is never achievable because both the aerodynamic resistances and other factors such as friction not allow it. However, a FM value between 0.75-0.80 is a satisfactory result, even if its overall value can be influenced by the aerodynamic flow coming from the anti-torque rotor where present. It seems paradoxical but a rotor is much more efficient in hover with a maximum take-off weight because the induced flow is greater.

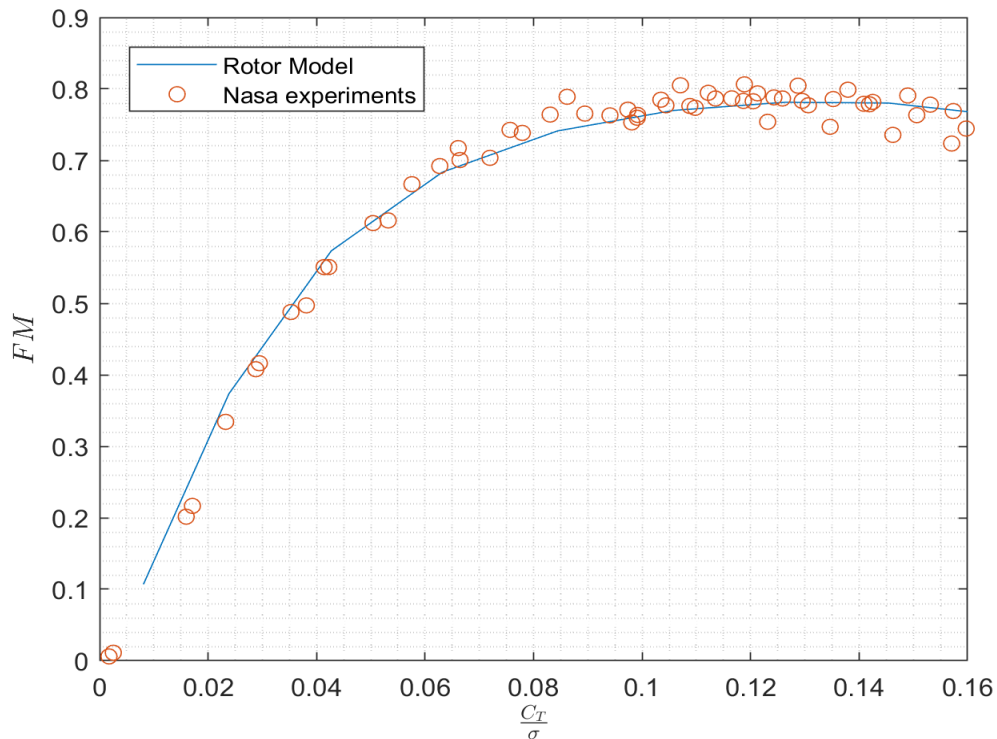


Figure 4.5: XV-15 rotor FM- $\frac{Ct}{\sigma}$  curve in Hover conditions

In this case, for the XV-15, FM values are considerably high, this is due to the fact that rotors of this type of aircraft, having speeds closer to those of the turboprop, but being considerably larger, maintains a higher efficiency than usual going up to values of 0.9 as shown below. What is more, from the figure above it is possible to notice how the trend found with the rotor model faithfully represents the experimental results again. This is another positive result which further validates the rotor model, at least for this phase of flight of the aircraft in question.

<i>RUN</i>	<i>V<sub>tip</sub>[fps]</i>	<i>M<sub>tip</sub></i>	<i>Coll[deg]</i>	<i>CT</i>	<i>CP</i>	<i>IdealCP</i>	<i>FM</i>	<i>CT/CP</i>
14.0000	768.4000	0.6904	8.0000	0.0110	0.0011	0.0008	0.7540	10.1900
14.0000	768.4000	0.6903	9.0000	0.0120	0.0012	0.0009	0.7470	9.6500
14.0000	768.0000	0.6899	10.0000	0.0130	0.0014	0.0010	0.7357	9.1200
14.0000	767.7000	0.6896	11.0000	0.0140	0.0016	0.0012	0.7236	8.6600
15.0000	768.7000	0.6904	2.0000	0.0056	0.0004	0.0003	0.6921	13.1000
15.0000	768.4000	0.6902	4.0000	0.0074	0.0006	0.0004	0.7641	12.5700
15.0000	768.4000	0.6901	6.0000	0.0092	0.0008	0.0006	0.7849	11.5700
15.0000	768.4000	0.6899	7.0000	0.0101	0.0009	0.0007	0.7866	11.0700
15.0000	768.4000	0.6898	8.0000	0.0111	0.0010	0.0008	0.7881	10.6000
15.0000	768.0000	0.6896	9.0000	0.0120	0.0012	0.0009	0.7858	10.1300
15.0000	769.0000	0.6903	-7.1000	-0.0003	0.0002	0.0000	0.0184	-1.4000
15.0000	769.0000	0.6903	-6.5000	0.0002	0.0002	0.0000	0.0112	1.0600
15.0000	769.0000	0.6903	-4.5000	0.0014	0.0002	0.0000	0.2015	7.5600
15.0000	769.0000	0.6903	-2.5000	0.0026	0.0002	0.0001	0.4162	11.5000
15.0000	769.0000	0.6900	-0.5000	0.0038	0.0003	0.0002	0.5508	12.7000
15.0000	769.4000	0.6904	3.5000	0.0069	0.0006	0.0004	0.7385	12.5400
15.0000	769.4000	0.6901	5.5000	0.0087	0.0007	0.0006	0.7710	11.7100
15.0000	769.0000	0.6899	6.5000	0.0097	0.0009	0.0007	0.7762	11.1600
15.0000	769.0000	0.6899	7.5000	0.0106	0.0010	0.0008	0.7832	10.7800
15.0000	769.0000	0.6898	8.5000	0.0115	0.0011	0.0009	0.7833	10.3200
15.0000	768.7000	0.6896	9.5000	0.0125	0.0013	0.0010	0.7792	9.8400
15.0000	769.7000	0.6904	-7.2000	-0.0003	0.0003	0.0000	0.0129	-1.0800
15.0000	769.7000	0.6904	-7.0000	-0.0004	0.0002	0.0000	0.0216	-1.5800
15.0000	769.7000	0.6904	-1.0000	0.0034	0.0003	0.0001	0.4971	12.0700
15.0000	769.4000	0.6904	1.0000	0.0047	0.0004	0.0002	0.6160	12.6600
15.0000	769.4000	0.6902	3.0000	0.0064	0.0005	0.0004	0.7036	12.4300
15.0000	769.4000	0.6899	5.0000	0.0084	0.0007	0.0005	0.7630	11.7900
15.0000	769.4000	0.6898	6.0000	0.0093	0.0008	0.0006	0.7770	11.4000
15.0000	769.0000	0.6896	7.0000	0.0104	0.0009	0.0007	0.7868	10.9300
15.0000	768.7000	0.6896	8.0000	0.0112	0.0011	0.0008	0.7866	10.5100
15.0000	770.0000	0.6904	5.5000	0.0088	0.0008	0.0006	0.7636	11.4900
15.0000	769.7000	0.6903	6.5000	0.0098	0.0009	0.0007	0.7736	11.0700
15.0000	769.7000	0.6902	7.5000	0.0107	0.0010	0.0008	0.7827	10.6900
15.0000	769.4000	0.6900	8.5000	0.0116	0.0011	0.0009	0.7771	10.1900
15.0000	769.4000	0.6900	9.5000	0.0126	0.0013	0.0010	0.7785	9.8000
15.0000	769.0000	0.6899	10.5000	0.0134	0.0014	0.0011	0.7633	9.3200
15.0000	769.0000	0.6899	11.5000	0.0143	0.0016	0.0012	0.7440	8.8000
15.0000	768.7000	0.6897	12.5000	0.0151	0.0018	0.0013	0.7171	8.2700
16.0000	771.3000	0.6903	8.0000	0.0108	0.0010	0.0008	0.7938	10.8000

Table 4.1: XV-15 Hover Flight test-Part 1, Ref. [12]

<i>RUN</i>	<i>V<sub>tip</sub>[fps]</i>	<i>M<sub>tip</sub></i>	<i>Coll[deg]</i>	<i>CT</i>	<i>CP</i>	<i>IdealCP</i>	<i>FM</i>	<i>CT/CP</i>
16.0000	771.0000	0.6899	10.0000	0.0127	0.0013	0.0010	0.7818	9.8200
16.0000	770.7000	0.6896	12.0000	0.0143	0.0016	0.0012	0.7428	8.7900
22.0000	762.8000	0.6902	9.0000	0.0123	0.0012	0.0010	0.7989	10.2000
22.0000	762.5000	0.6900	10.0000	0.0133	0.0014	0.0011	0.7908	9.7100
22.0000	762.1000	0.6899	11.0000	0.0140	0.0015	0.0012	0.7690	9.1900
22.0000	762.1000	0.6896	12.0000	0.0148	0.0017	0.0013	0.7420	8.6400
23.0000	764.8000	0.6903	2.0000	0.0059	0.0004	0.0003	0.7172	13.2200
23.0000	764.4000	0.6900	4.0000	0.0077	0.0006	0.0005	0.7890	12.7400
23.0000	764.1000	0.6899	6.0000	0.0095	0.0008	0.0007	0.8051	11.6600
23.0000	764.1000	0.6897	7.0000	0.0106	0.0010	0.0008	0.8064	11.0900
23.0000	764.1000	0.6896	8.0000	0.0115	0.0011	0.0009	0.8045	10.6300
23.0000	764.8000	0.6900	-7.0000	0.0002	0.0002	0.0000	0.0060	0.6900
23.0000	764.8000	0.6900	-5.0000	0.0015	0.0002	0.0000	0.2166	7.8500
23.0000	764.8000	0.6899	-3.0000	0.0026	0.0002	0.0001	0.4078	11.3900
23.0000	764.8000	0.6898	-1.0000	0.0037	0.0003	0.0002	0.5507	12.8300
23.0000	764.4000	0.6897	1.0000	0.0051	0.0004	0.0003	0.6667	13.1700
23.0000	764.4000	0.6896	3.0000	0.0067	0.0005	0.0004	0.7427	12.8000
25.0000	767.4000	0.6903	-3.0000	0.0021	0.0002	0.0001	0.3342	10.3900
25.0000	767.4000	0.6902	-1.0000	0.0031	0.0003	0.0001	0.4879	12.3100
25.0000	767.4000	0.6901	1.0000	0.0045	0.0003	0.0002	0.6123	12.9300
25.0000	767.1000	0.6900	3.0000	0.0059	0.0005	0.0003	0.7005	12.8800
25.0000	767.1000	0.6898	5.0000	0.0080	0.0007	0.0005	0.7655	12.1300
25.0000	767.1000	0.6897	6.0000	0.0087	0.0008	0.0006	0.7531	11.4000
25.0000	767.1000	0.6897	6.0000	0.0088	0.0008	0.0006	0.7597	11.4400
25.0000	766.7000	0.6896	7.0000	0.0100	0.0009	0.0007	0.7946	11.2500
25.0000	768.4000	0.6901	11.0000	0.0136	0.0014	0.0011	0.7780	9.4200
25.0000	758.2000	0.6900	12.0000	0.0142	0.0016	0.0012	0.7445	8.8300

Table 4.2: XV-15 Hover Flight test-Part 2, Ref. [12]

### 4.1.3 XV-15 Rotor Efficiency



Figure 4.6: Bell XV-15 in airplane mode

Since this type of aircraft is able to rotate the nacelles, turning into an aircraft mode similar to a real turboprop, it is appropriate to develop some tests on its efficiency. Therefore, by inserting in the rotor model an angle of nacelles ( $\beta_m$ ) equal to  $90^\circ$ , XV-15 switched to the airplane mode in order to monitor the trend of the rotor efficiency ( $\frac{C_{t\mu}}{C_p}$ ) as the flight speed and the collective varies. In particular, three particular conditions are evaluated.

Also, in the following figure it is shown that with varying the collective, the maximum efficiency point shifts towards higher advancing ratios, as is the case of traditional turboprops. Moreover, it is also interesting to notice that as the collective increases not only the curves move to the right, but the efficiency also undergoes a slight increase, so it is worthwhile, in airplane mode, to keep high values of collective. These two phenomena are due to the fact that elevated collectives guarantee a higher inflow at the same flight speed, therefore the incidences along the blade increase and consequently also the traction (more than the  $C_p$  as shown in Fig. 4.3) and therefore the efficiency.

It can also be noticed that the efficiencies for these type of rotors are quite elevated. In fact, compared to a traditional turboprop, where the efficiencies see their peak around 0.8 as shown below, the propellers of a tilt-rotor have a larger extension, this means that the losses of separation at the tip of the blade are reduced. Furthermore, the angular speeds of a tilt-rotor are higher than those of traditional helicopters, as previously announced, but lower than those of a real turboprop. This, allows to contain the effects due to the achievement of the crit-

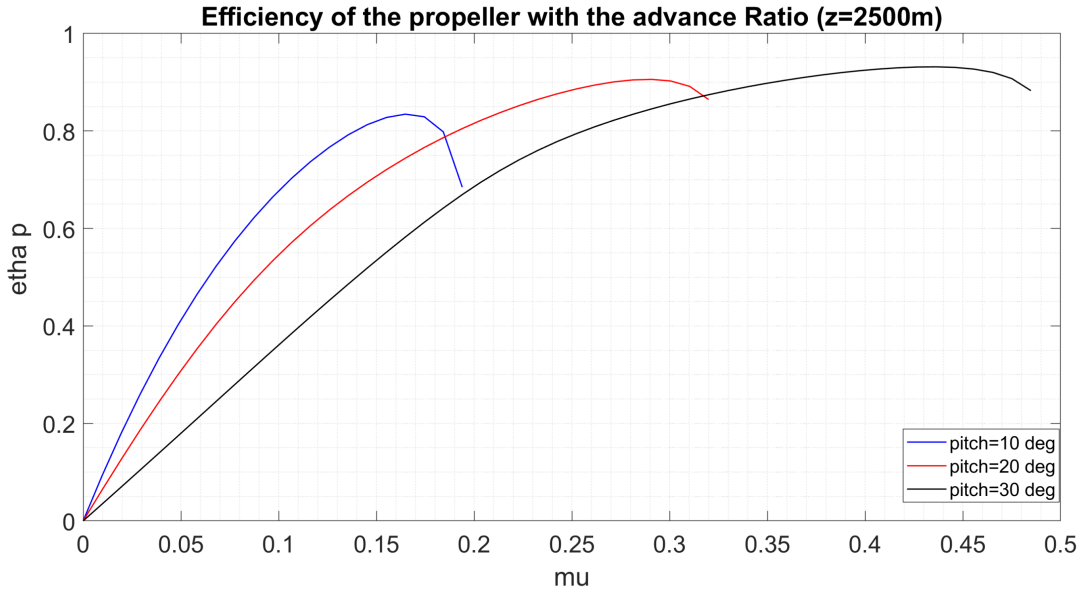


Figure 4.7: XV-15 rotor efficiencies

ical Mach at the blade's tip reducing once again the losses and increasing the efficiency in comparison with a standard turboprop. As proof of this, it is also possible to observe the data collected by Nasa, Ref. [15], about the typical efficiencies of tilt-rotor so far built, where:

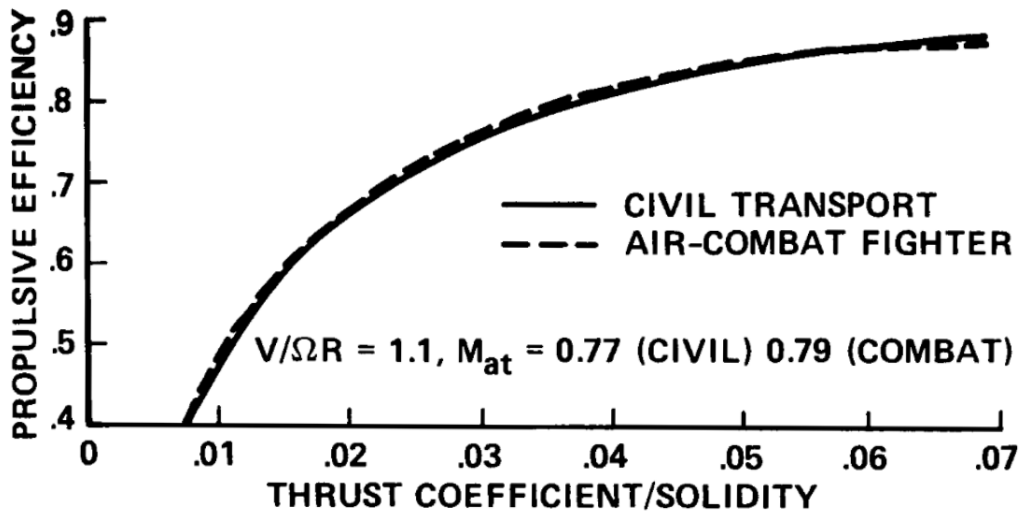


Figure 4.8: Tilt-rotors efficiencies

The graph above no longer has the advancing ratio ( $\mu$ ) on the axis of the abscissas but the traction coefficient scaled for its solidity. However, it can be clearly seen that even for experimental NASA data, for this type of aircraft there are considerable efficiencies. While, as previously mentioned, for conventional

turboprops the maximum efficiency are no higher than 0.8, as it is shown the following image.

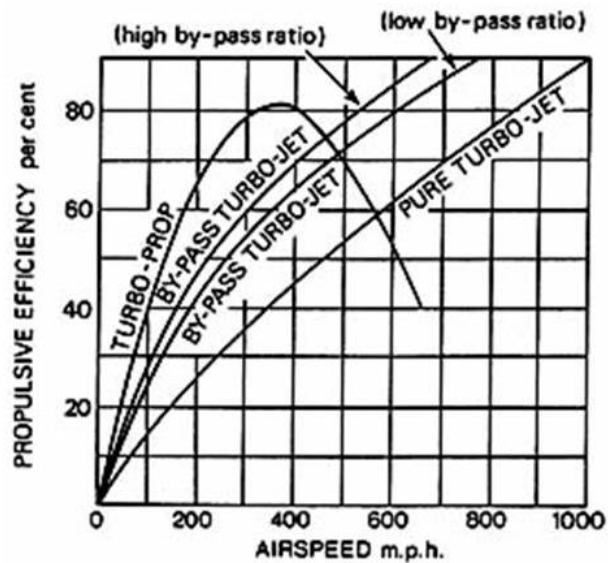


Figure 4.9: Turboprop efficiencies

## 4.2 XV-15's longitudinal cyclic response

In order to further validate the model, it is also verified whether the response to the cyclic commands is reliable or not. To realize this purpose, tests are carried out to vary the longitudinal cyclic (B1). The following test are performed:

- *Hover*
- *Advanced flight: 30 m/s*
- *Advanced flight: 30 m/s and side-slip angle (5 deg)*
- *Advanced flight: 40 m/s*
- *Advanced flight: 50 m/s*

The conditions for simulations in this case are:

- *Sea level Standard atmospheric conditions*
- *Coll = 6 deg*
- *LatCycl (A1) = 0 deg*
- *p = 0 rad/s*
- *q = 0 rad/s*

As reference for this validation, simplified formulas obtained from Bramwell are used, Ref. [2], which require the following additional rotor data for the treatment:

$$\begin{aligned}\epsilon &= 3e/(2R - 2e) = 0 \\ \sigma &= 0.0891 \\ lock(\gamma) &= \rho acR^4/I_\beta = 3.63\end{aligned}\quad (4.6)$$

Therefore, in the following graphs are represented the x-axis force  $X_h$  (H), the pitch moment (M) in the non-rotating reference system centered in the hub and the response of the rotor command in terms of flapping (b1c). As reported in Ref. [2] the Bramwell's formulation used are:

$$\begin{aligned}h_c &= -[1/4\mu\delta + a1Cl_\alpha(1/6\theta_0 + 3/8\lambda + 1/8\mu a_1) - \mu\theta_0\lambda a/4] \\ H &= \rho\Omega^2 R^2 A\sigma h_c \\ \bar{M} &\approx -\bar{X}hR + 0.5Sea_1\end{aligned}\quad (4.7)$$

Where:

$$\begin{aligned}S &= m_b r_{cg}^2 \Omega^2 \quad [Nm/rad] \\ \delta &= 0.007 - 0.0216\alpha_s + 1.1\alpha_s^2 \quad [n/d] \\ \lambda_d &= V/V_{tip} \sin(\alpha_s) - \lambda_0 \quad [n/d] \\ a_1 &= \frac{2\mu}{1 - \mu^2/2} (4/3\theta_0 - \lambda) - \frac{1 + 1.5\mu^2}{1 - \mu^2/2} B_1 - \frac{\frac{16q}{\gamma\Omega} - \frac{p}{\Omega}}{1 - \mu^2/2} \quad [rad] \\ A &= \pi R^2 \quad [m^2]\end{aligned}\quad (4.8)$$

As it is shown in results, the trends and orders of magnitude are respected in most cases. In addition, the responses in terms of H-load and flapping (b1c) are overlapping several times. In some graphs, however, a different pitch response and sometimes even longitudinal load (H) not superimposed can be observed. This could be due to the fact that among the approximations made by Bramwell there is the one of not twisted blade, an assumption that is not easily negligible in a case like this of XV-15, where the values of twist are remarkable, as shown in Fig. (4.1). Moreover, there could be also an inaccuracy in the value inserted of  $K_\beta$  in the rotor model, which affects the flaps and therefore the rotor loads. In addition, the Bramwell' model does not consider the 'tip loss factor', and the effects of Mach on the  $C_l$  and  $C_d$  coefficients. These, could also be meaningful effects, in fact, because of the high rotational speed of the blades (589 rpm),  $M_{tip}$  could reach high values, especially in advanced flight where the translational contribution of speed on the blade is notable. Therefore, also these contributions can be the cause of the various deviations in the graphs of the rotor model from the reference. For these reasons, the comparison with Bramwell is used purely as a reference for orders of magnitude and trends, and a perfect overlap of curves cannot be always expected.

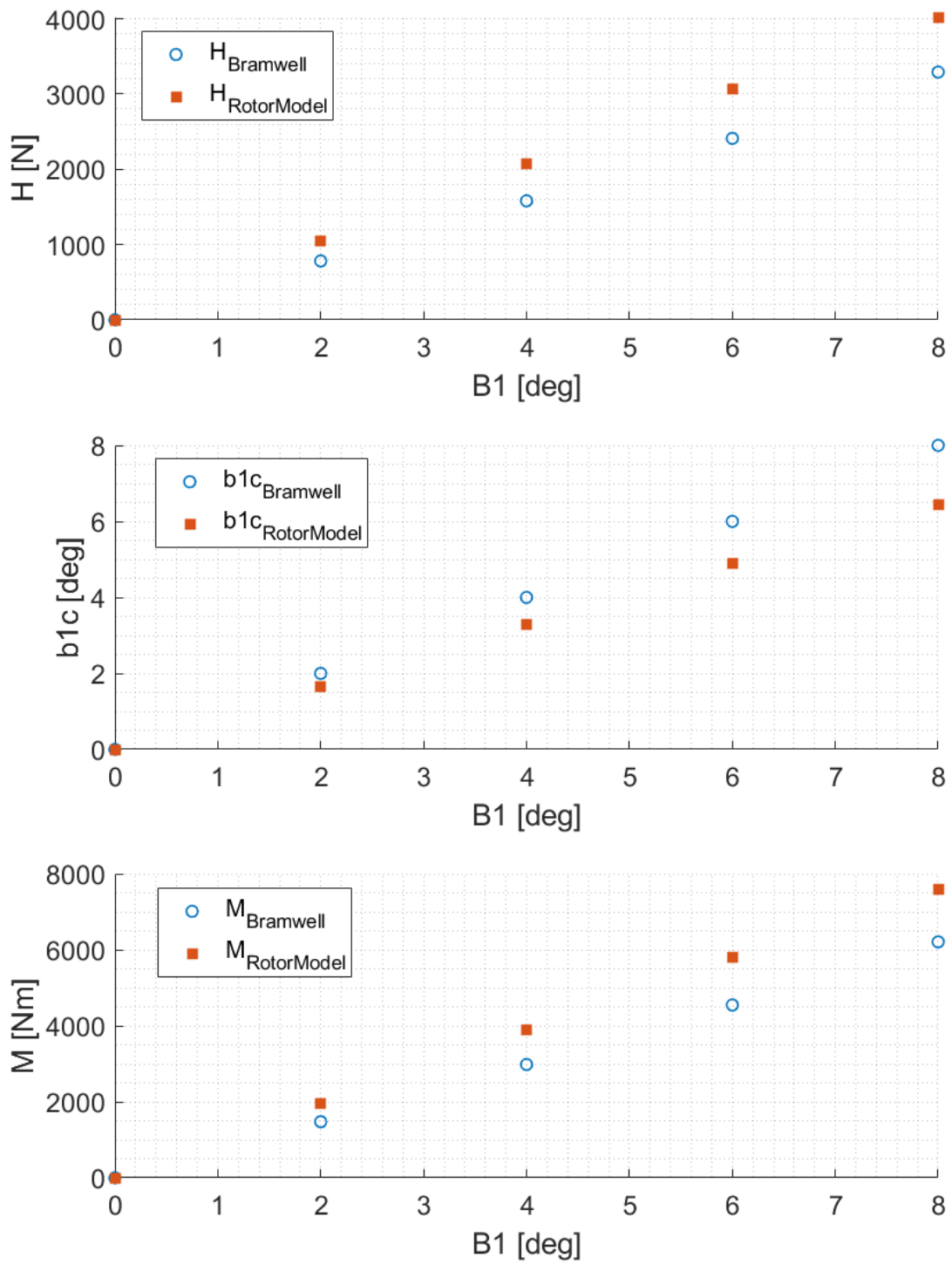


Figure 4.10: XV-15 Hover

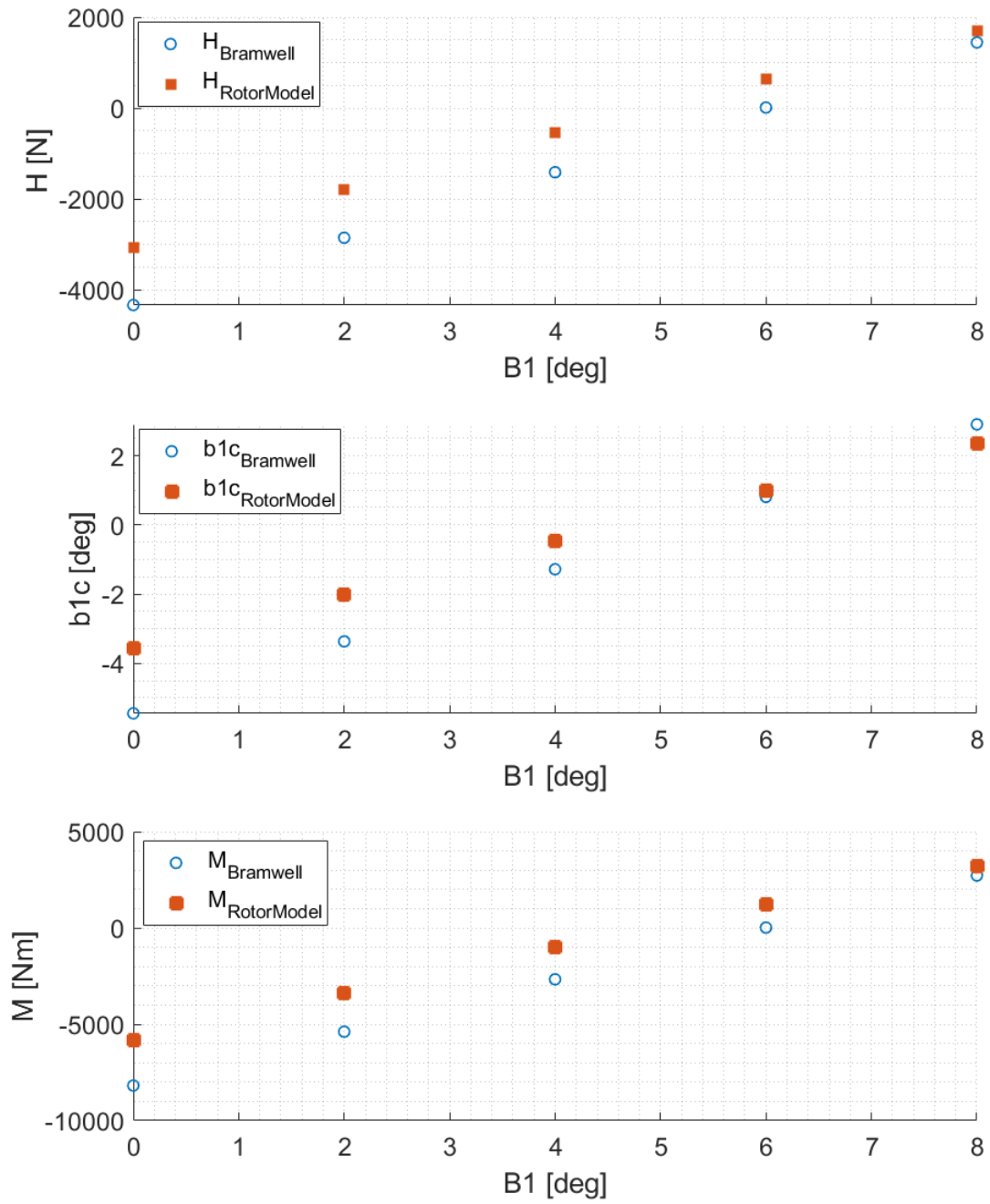


Figure 4.11: XV-15 in advanced flight  $u_h = 30 \text{ m/s}$

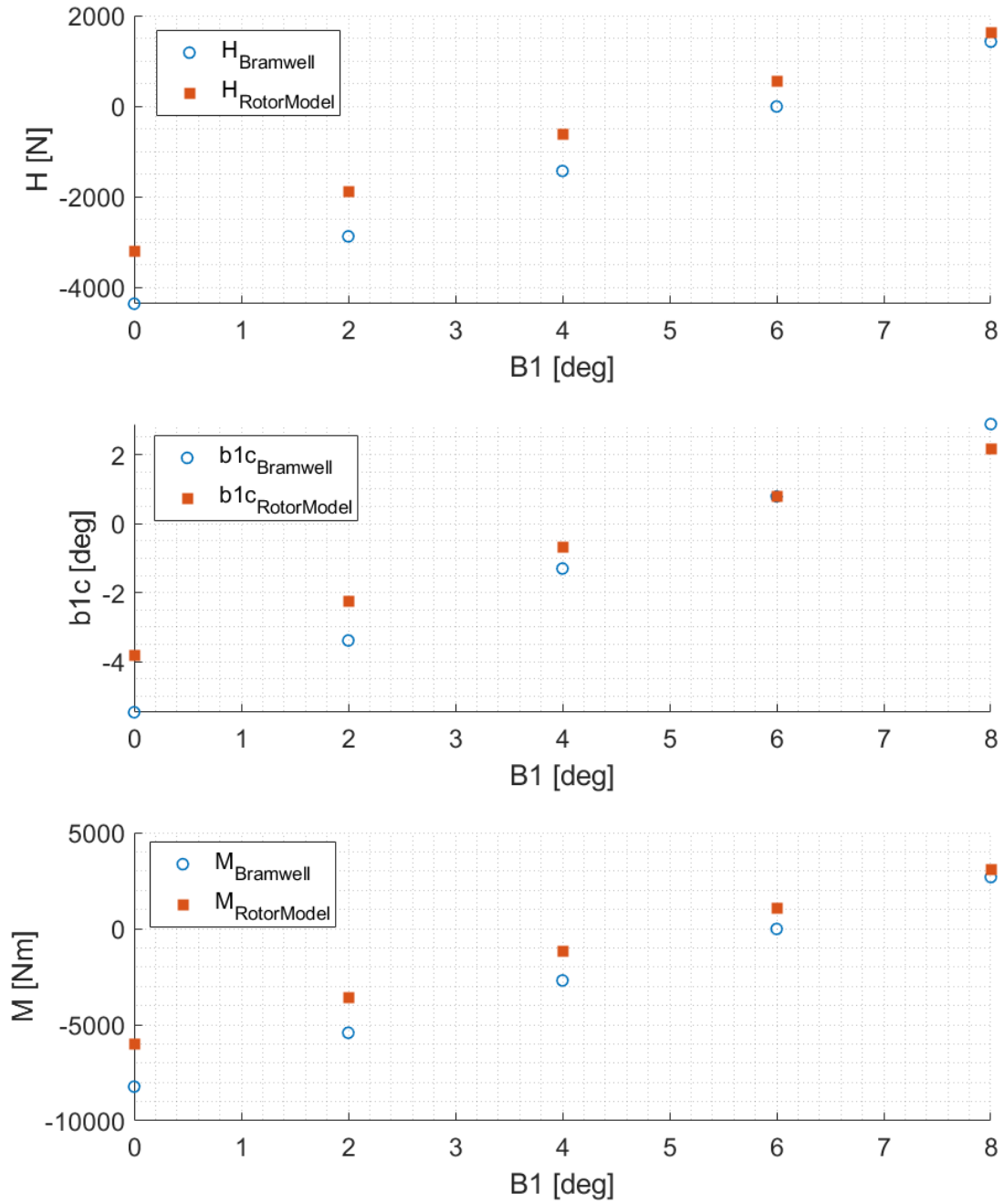


Figure 4.12: XV-15 in advanced flight  $u_h = 30m/s$ ,  $5deg$  of side-slip angle

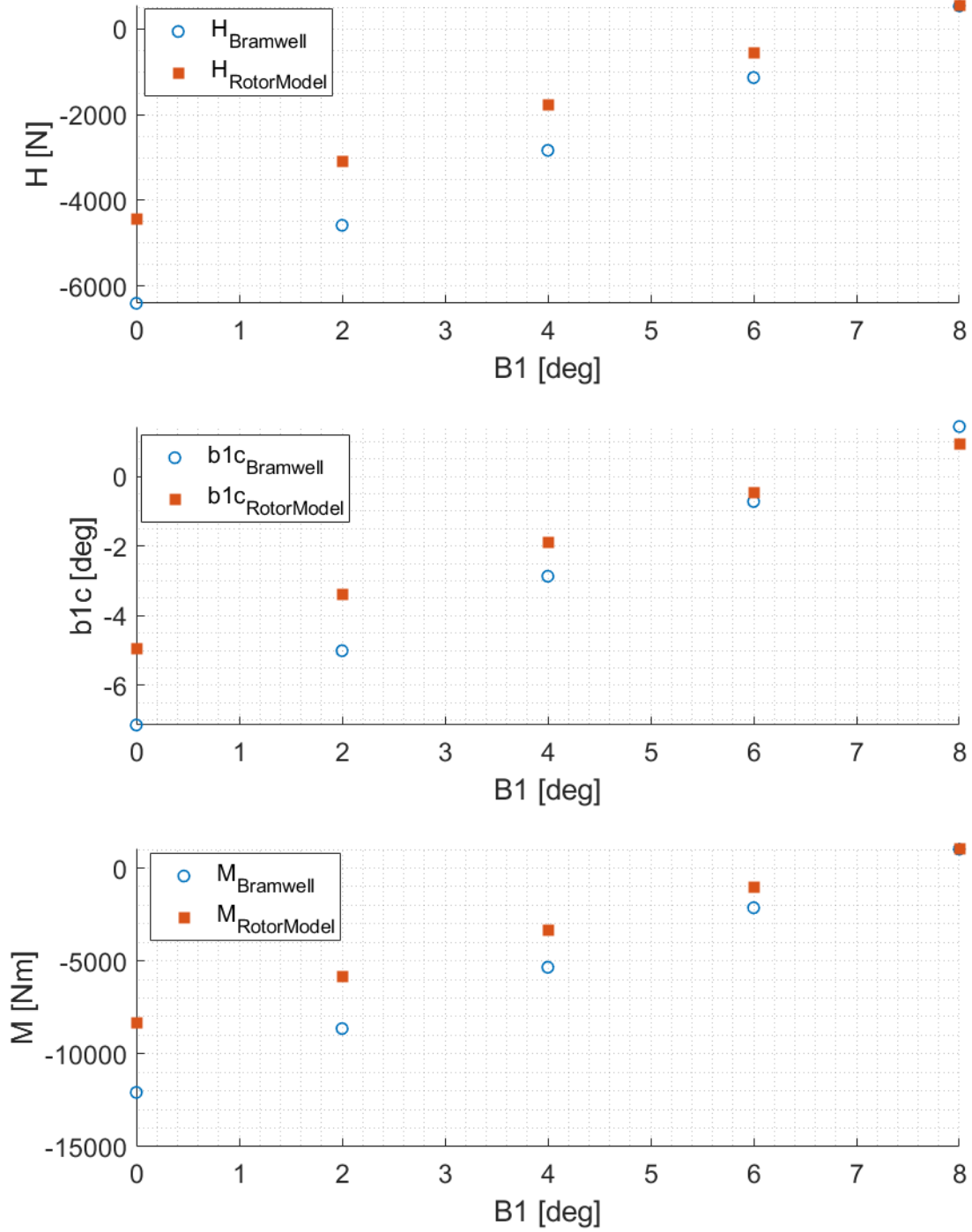


Figure 4.13: XV-15 in advanced flight  $u_h = 40m/s$

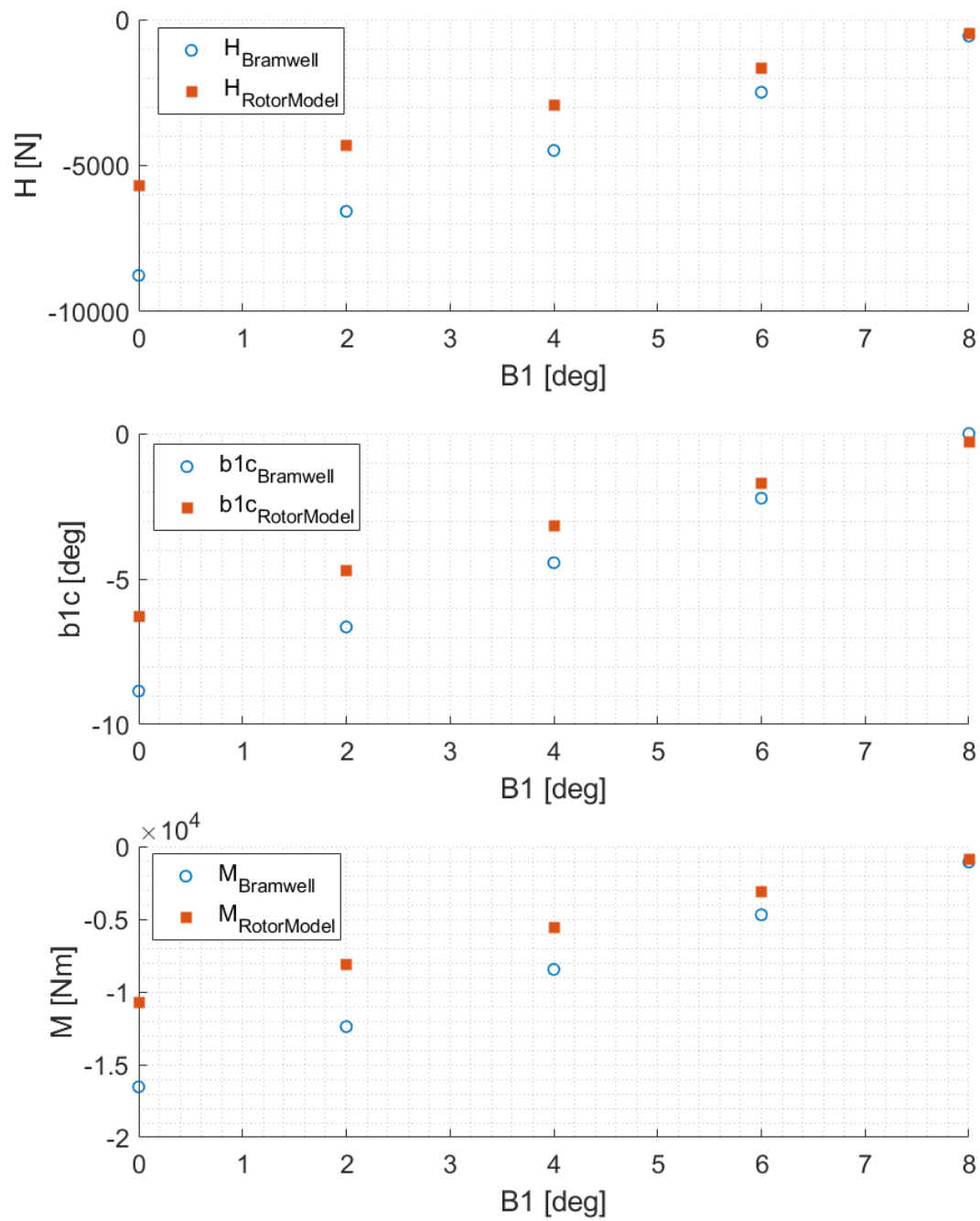
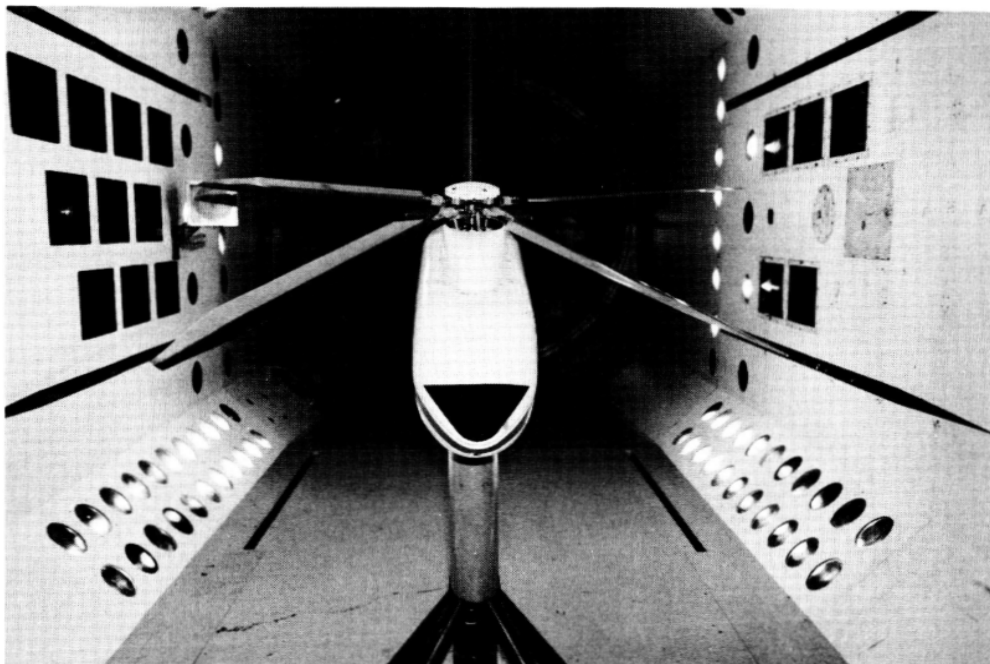


Figure 4.14: XV-15 in advanced flight  $u_h = 50\text{m/s}$

### 4.3 UH-60 test and validation

To enrich the validation, after demonstrating the satisfactory performance in simulating the rotor of the XV-15, a rotor of completely different scale is analyzed. In this case the model is scaled, due to the fact that the Langley wind tunnel is not large enough to accommodate a rotor of large size. But, a scaled model implies aerodynamic similarities as shown later. In fact, the real rotor of the UH-60 has the task of supporting what is a 'heavy' helicopter, requiring all its 8.177 meters in radius of the rotor, in accord to Ref. [10]. In addition, the speeds are considerably lower, in fact the nominal 258 rpm of the main rotor is less than half of what seen for the XV-15. Moreover, this type of aircraft, being fully articulated, has values of resistance at the blade flapping almost zero ideally, unlike the XV-15 which is characterized by a semi-rigid rotor. Then, the stiffness of the flap hinge in the reality is not zero because of the presence of mechanical dampers. For these reasons, several input parameters that are shown later vary considerably compared to the rotor previously analyzed. Therefore, the main objective of this second analysis is to validate the rotor model for the widest range of types and sizes. In fact, once the model is validated even for a rotor that is a extremely different from the previous one, it is reasonable to suppose that satisfactory results can be obtained even for those rotors that are equipped with intermediate parameters or similar to those analyzed.



L-85-12,990

Figure 4.15: UH-60 Black Hawk scaled rotor in Langley Wind Tunnel

### 4.3.1 Rotor inputs

Therefore, for this type of aircraft it is appropriate to create a new initialization file. First of all, the data regarding the aerodynamics of the correct profile seen previously in the relative section have to be insert. After that, the real twist law of the blade is again approximated with a third degree polynomial, as it is possible to see in the following figure:

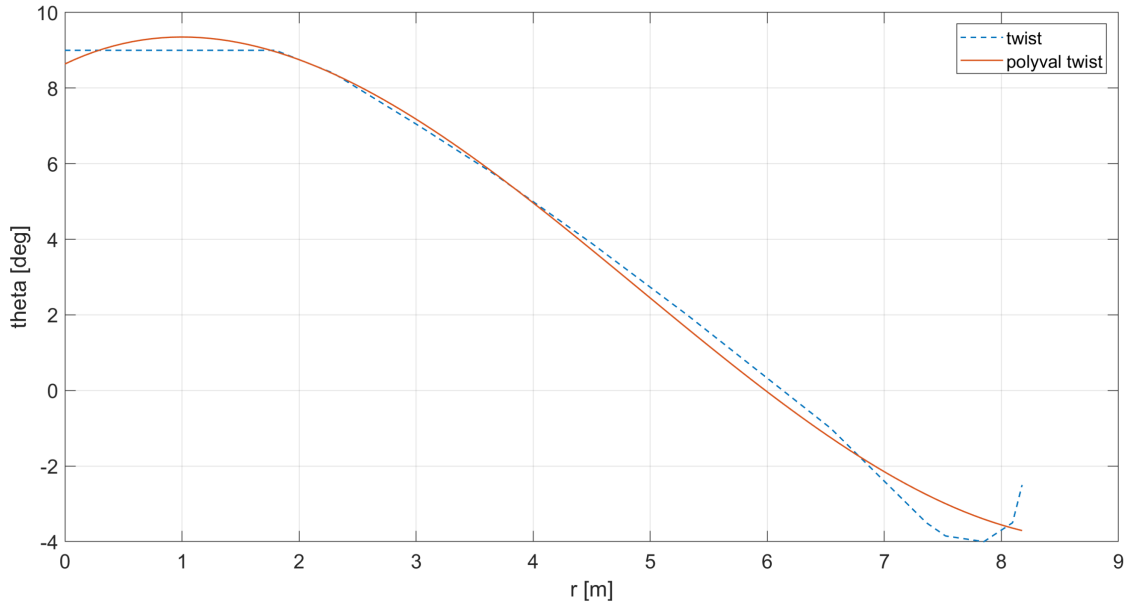


Figure 4.16: UH-60 Blade twist law

Where the polynomial coefficients are:

$$\begin{aligned}
 t_3 &= 0.001 \quad [rad/r^3]; \\
 t_2 &= -0.0144 \quad [rad/r^2]; \\
 t_1 &= -0.0259 \quad [rad/r]; \\
 t_0 &= 0.1508 \quad [rad];
 \end{aligned}
 \tag{4.9}$$

Instead, for the taper law of the blade, a constant value is considered for the entire blade, in fact, in this particular aircraft a constant chord distribution along the blade is chosen by designers. Therefore, the polynomial coefficients for the polynomial chord distribution are:

$$\begin{aligned}
 c_3 &= c_2 = c_1 = 0.0 \\
 c_0 &= 0.57 \quad [m];
 \end{aligned}
 \tag{4.10}$$

While the others parameters useful to define the rotor of the UH-60 are:

$$\begin{aligned}
I_\beta &= 2500 \quad [kgm^2] \\
M_\beta &= 380 \quad [kgm] \\
m_b &= 95 \quad [kg] \\
n_b &= 4 \quad [n/d] \\
r_{cg} &= M_\beta/m_b = 4 \quad [m] \\
K_1 &= -\tan(\delta_3) = 0 \quad [n/d] \\
e &= 0.368 \quad [m] \\
K_\beta &= 0 \quad [Nm/rad] \\
R &= 8.177 \quad [m] \\
\alpha_0 &= -1.25 \quad [deg]
\end{aligned} \tag{4.11}$$

### 4.3.2 Equivalence of the scaled model

For the UH-60 case, the reference data set are derived once again from experimental tests conducted at NASA Langley Research Center and reported in [21], where all data are acquired with equal  $M_{tip}$ . What reported in this paper is referred to tests conducted on a scaled rotor model (due to the reduced width of the wind tunnel) where all geometric and environmental factors are adapted to ensure the Reynolds numbers similarity and the validity of the comparison performed. As shown in the following steps, in order to achieve the aerodynamic equivalence between models of different sizes, the higher attention must be paid to all correlations. In fact, if only one parameter is inserted in an inconsistent way, there is the risk of obtaining incorrect results. Therefore, in order to grant the model scaling similarity, the following mathematical passages are done. Setting the test conditions at Langley, Virginia (Sea Level), and the rotational speed of the scaled model:

$$\begin{aligned}
\rho &= 1.225 \quad [kg/m^3] \\
a &= 340 \quad [m/s] \\
\Omega &= 68.06 \quad [rad/s]
\end{aligned} \tag{4.12}$$

As the  $M_{tip}$  parameter is fixed during the test, with  $M_{tip} = 0.65$ , the following relation can be written:

$$M_{tip} = \frac{\Omega R^*}{a} \tag{4.13}$$

And with this parameter is possible to find the equivalent extension of the blade that has to be insert in the initialization file:

$$R^* = \frac{M_{tip} a}{\Omega} = 3.247 \quad [m] \tag{4.14}$$

Once the new radial dimension characteristic is found, the blade chord is scaled for the same amount:

$$c^* = c \frac{R^*}{R} = 0.2263 \quad [m] \tag{4.15}$$

At this point, also other input parameters of the rotor should be corrected. The new mass of the blade is easy to obtained, in fact, the mass per unit of length is known and equal to 13.92 kg/m:

$$m_b^* = 37.74 \quad [kg] \quad (4.16)$$

To find the new flapping moment of inertia of the blade, the calculation is more complex. Therefore, the area of the scaled profile of the blade is calculated using the trapezoid method, knowing the position in space of those points which outline the shape of the profile, available on many airfoil tools. Once obtained the area, the blade is assimilated to a rectangular trapezoid whose moment of inertia of interest is formulated as follows:

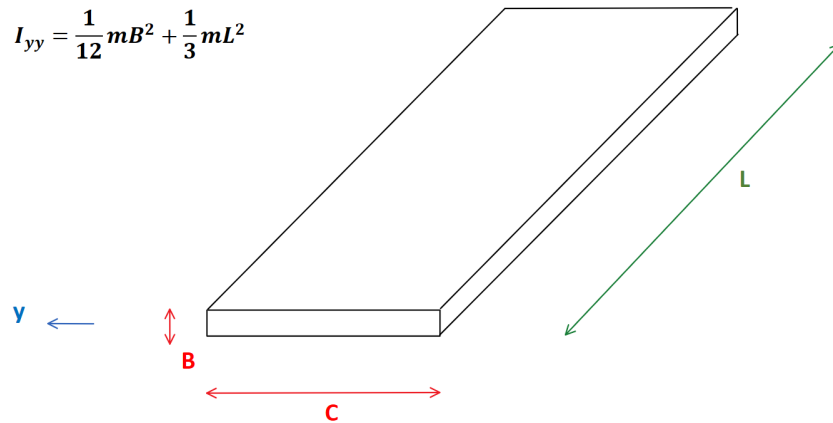


Figure 4.17: Blade's simplified scheme

Since the equivalent area is calculated with the trapezoids, it is now possible to obtain the size 'B', considering the long side of the section of the rectangle (C) equal to the chord ( $c^*$ ), and matching the areas. Since the prism extension (L) is equal to  $R^*$ , it is now possible to obtain the new moment of inertia:

$$I_\beta^* = 1000 \quad [kgm^2] \quad (4.17)$$

Also, considering the center of gravity of the scaled blade positioned in the same radial position as the percentage of the original blade is possible to find:

$$\begin{aligned} r_{cg}^* &= 1.5884 \quad [m] \\ M_\beta^* &= 59.9462 \quad [kgm] \end{aligned} \quad (4.18)$$

Even hinge offset is always considered to be 5% of the blade extension:

$$e = 0.05R^* = 0.1623 \quad [m] \quad (4.19)$$

### 4.3.3 Results and Validation in Hover

Once set the initial conditions, the following results for the Hover condition are found:

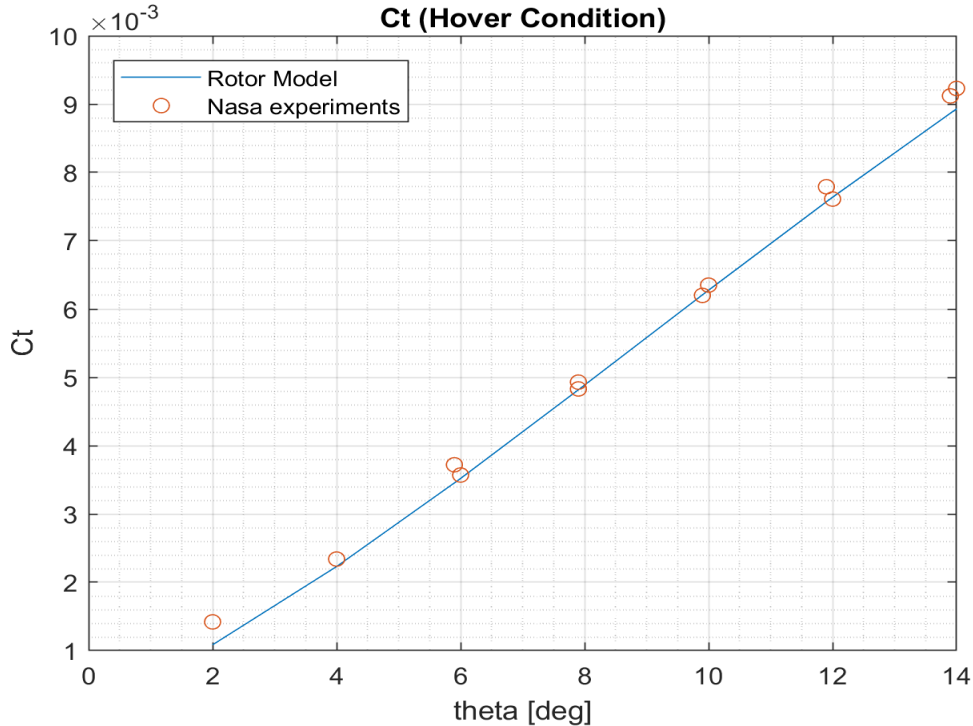


Figure 4.18: UH-60 Ct-Collective curve

Also in this case it can be seen how the trend of the traction coefficient, with the collective command, reflects the results obtained in the experimental tests. In fact, the continuous curve (of the rotor model) is perfectly superimposed on the experimental points. This first result, shows us again that the inserted aerodynamics, the law of twist, and the other parameters that affect the aerodynamics of the blade are inserted accurately. From following figure, it is shown that even the power levels with varying the traction coefficient, and therefore the collective, are respected. This means that also the aerodynamic curve of the drag coefficient is inserted in a faithful way, at least for all the incidences recorded in the Hover condition. Instead, the last figure shows the trend of the figure of merit with the traction coefficient scaled for the solidity of the rotor. Therefore, also for the UH-60 the trend returned by the model of the rotor is satisfactorily superimposed on the results obtained experimentally. Moreover, it is interesting to notice that the maximum value of figure of merit obtained is inferior to 0.8, and therefore lower than the values recorded for the XV-15. Moreover, as it is notable the rotor of the UH-60 is truly different from the tilt-rotor one analyzed before, and, in particular, analyzing this last trend, it results less efficient in its complex.

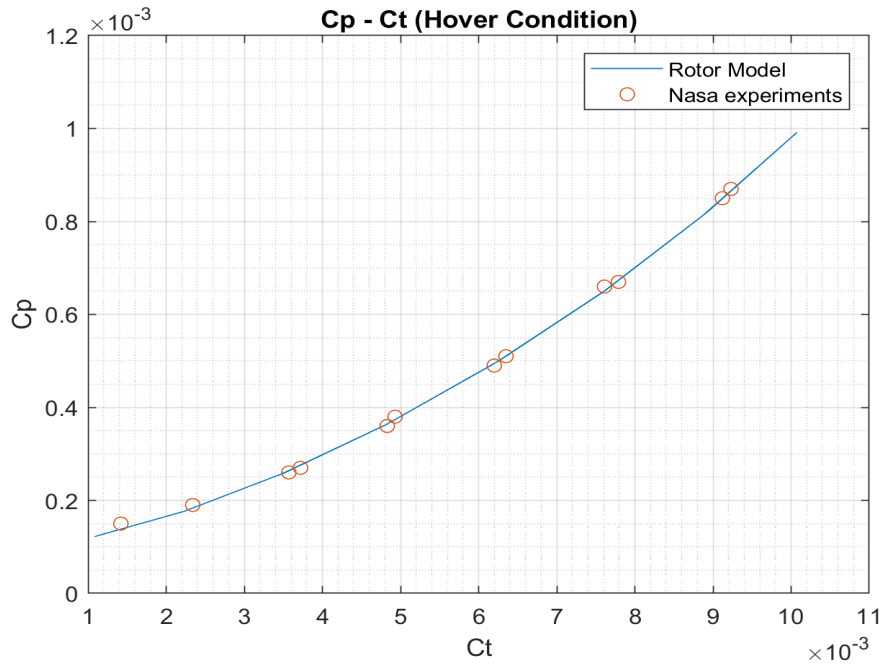


Figure 4.19: UH-60 Cp-Ct curve

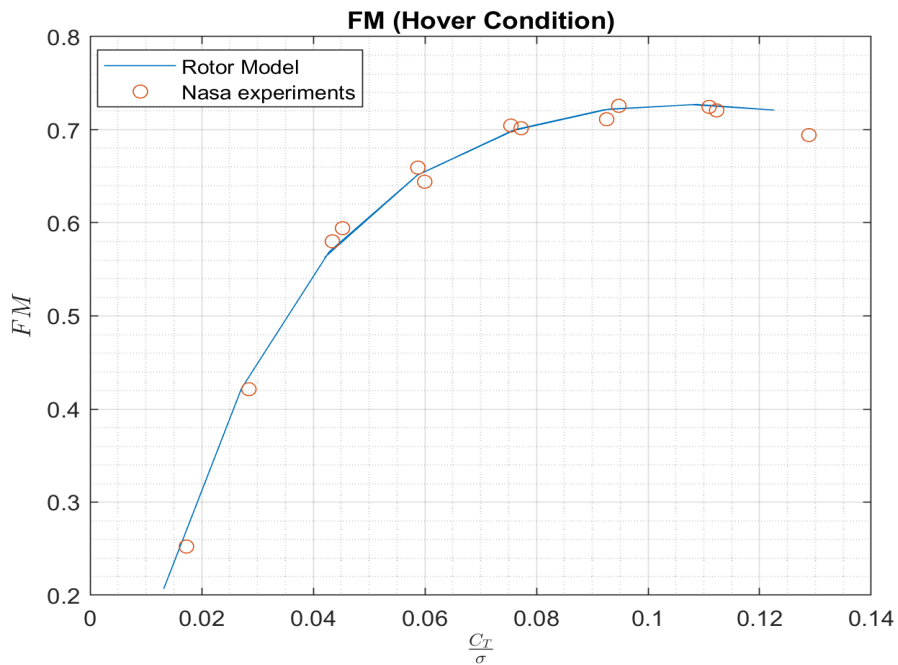


Figure 4.20: UH-60 FM- $\frac{C_t}{\sigma}$  curve

<i>Run</i>	<i>A1</i>	<i>B1</i>	$\theta_0$	<i>CT</i>	<i>CQ</i>
1292	-.3	-.1	2.0	.00142	.00015
1293	-.4	.1	4.0	.00234	.00019
1294	-.5	.1	6.0	.00357	.00026
1295	-.5	.2	7.9	.00483	.00036
1296	-.6	.3	9.9	.00620	.00049
1297	-.6	.1	12.0	.00761	.00066
1298	-.8	.3	13.9	.00912	.00085
1299	-.7	.0	15.9	.01059	.00111
1300	-.6	.3	14.0	.00923	.00087
1301	-.5	.4	11.9	.00779	.00067
1302	-.6	-.1	10.0	.00635	.00051
1303	-.6	.0	7.9	.00493	.00038
1304	-.5	.4	5.9	.00372	.00027

Table 4.3: UH-60 Hover Flight test, Ref. [21]

The rotor, for the UH-60' case, is also validated using an existing model (TDA) developed at the University of Meryland. The software in question is the result of a research made by Giorgio Guglieri, full professor in 'Flight Mechanics' at Politecnico di Torino. The software is already validated, and therefore constitutes a further reliable source of comparison for the model discussed here. In particular, the trend of the traction coefficient with the variation of the collective is visualized again, and in this case also, positive results are found, as shown in the following trend:

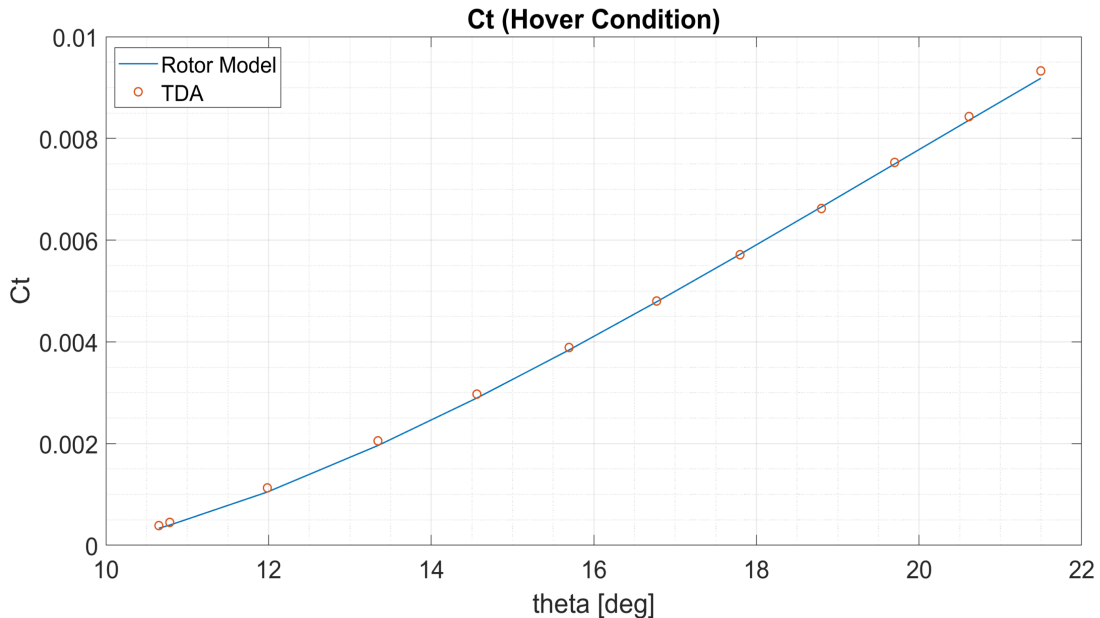


Figure 4.21: UH-60 Ct-Collective TDA Comparison

The tests performed in this case refer to a flight condition at 5250 ft altitude. From the figure above, therefore, is possible to observe how the two curves overlap in a more than satisfactory way, proving again that the model has the necessary potential to be useful for flight simulation.

<i>timeSim</i> [ms]	$\theta_0$ [deg]	$C_p$	$\lambda(TDA)$	Ct (TDA)
1.3	10.651	0.0	0.0	0.000387
67.9	10.785	0.00006	0.005477	0.000450
701	11.985	0.00072	0.01897	0.001128
1791	13.345	0.00164	0.02864	0.002053
2791	14.562	0.00255	0.03571	0.002972
3791	15.696	0.00346	0.04159	0.003889
4791	16.773	0.00438	0.04679	0.004803
5791	17.799	0.00529	0.05143	0.005714
6791	18.8	0.00620	0.05567	0.006622
7791	19.7	0.00711	0.05962	0.007528
8791	20.615	0.00803	0.06336	0.008430
9791	21.498	0.00894	0.06685	0.009328

Table 4.4: UH-60 TDA Test Results

## 4.4 UH-60 in Advanced Flight

Once the Hover condition is analyzed, it is also necessary to evaluate the behaviour of the rotor model in advanced flight, in fact, the Hover condition is only one of the many possible flight modes for this type of aircraft.

Therefore, it is necessary to obtain meaningful answers also during the phase of translated flight, in order to make the simulation model as complete and reliable as possible. For these reasons, the power coefficient with varying of the advancing ratio for the UH-60 are analyzed. To realize this, experimental data collected in Ref. [21] are used. Again, these data are obtained with the same model of the rotor reduced in size. The data obtained from NASA experiments are not satisfactory numerous as far as the advanced flight phase of flight of the UH-60 is concerned. In particular, the conditions analyzed are:

$u_h[m/s]$	$w_h[m/s]$	$\theta_0[deg]$	$A1[deg]$	$B1[deg]$	$\alpha_s[deg]$
34.695	0	7.90	4.00	2.10	0.00
46.722	0	10.30	3.40	2.70	3.30
58.955	0	8.10	3.90	4.10	-0.10
80.955	0	16.30	4.50	6.40	8.80

Table 4.5: UH-60 Advanced Flight test input, Ref. [21]

Where  $\alpha_s$  is derived as  $u_h$ ,  $w_h$  and  $b1s$  are known, from the simple relationship:

$$\alpha_s = b1s + atan\left(\frac{-w_h}{u_h}\right) \quad (4.20)$$

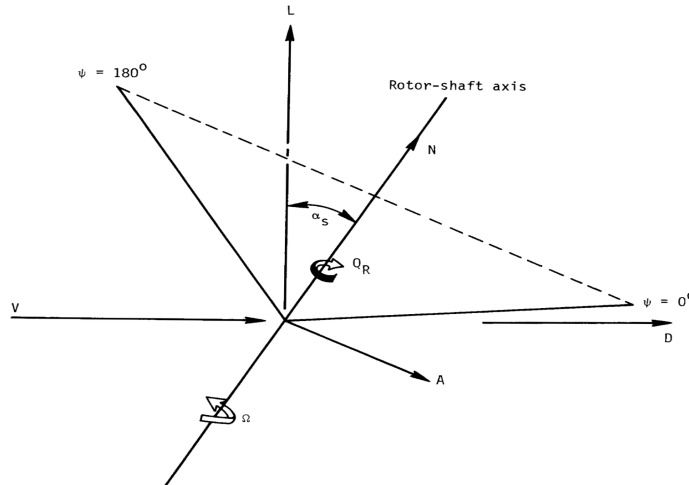


Figure 4.22: Disk inclination  $\alpha_s$

Therefore, in the following figure, is shown in the trends of the power coefficient ( $C_p$ ) as a function of the advancing ratio, found by the experimental data and by the rotor model. The curves aren't perfectly superimposed in that case, but the trend is analogous. In addition, the percentage error is acceptable. This first result shows how the power regimes are respected even during advanced flight. Therefore, once again, this proves that the aerodynamic data, concerning the drag coefficient ( $C_d$ ), are entered accurately because of the strict correlation between  $C_d$  and  $C_p$  mentioned before. Furthermore, this result leads to think that if the power levels required by the aircraft are well described by the model in question, the rotor model may be useful not only for the purpose of flight simulation, but also during the planning of a mission and for other design/testing phases such as the estimation of consumption and of the traction levels of a new rotor concept.

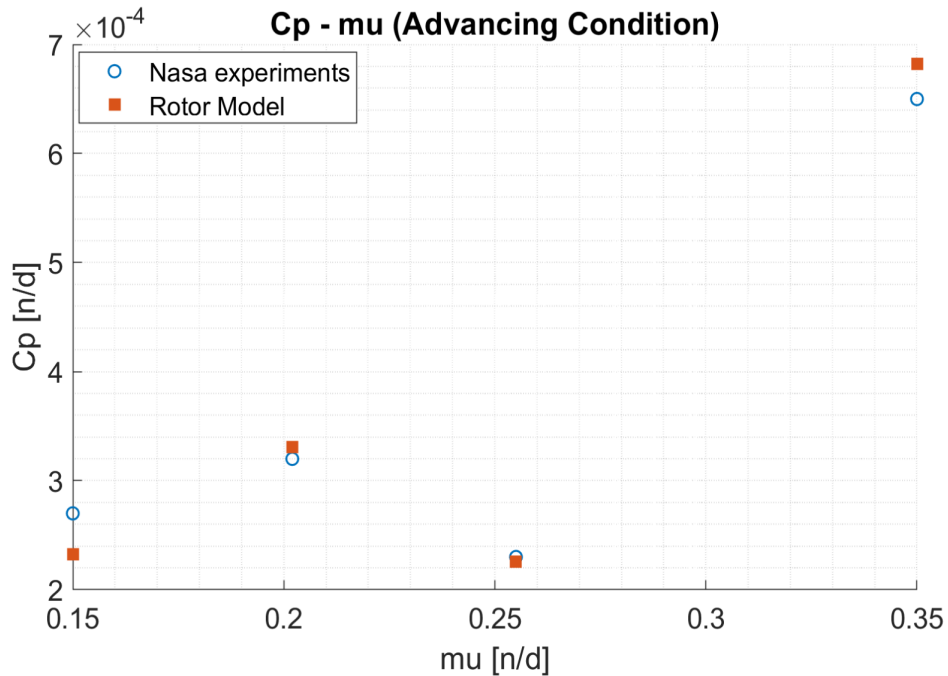


Figure 4.23: UH-60  $C_{p\text{ow}}-\mu$  curve

[n/d]	Test1	Test2	Test3	Test4
mu	0.150	0.202	0.255	0.350
CL	0.00654	0.00653	0.00652	0.00652
CD	0.00	0.31e-3	0.03e-3	0.84e-3
Cp	0.27e-3	0.32e-3	0.23e-3	0.65e-3

Table 4.6: UH-60 Advanced Flight test results

## 4.5 UH-60's longitudinal cyclic response

As seen above for the XV-15 also for the UH-60' case is necessary to evaluate the result in terms of loads in response to a cyclic command in order to further enrich the validation. In that case, the flight condition analyzed are:

- *Advanced flight: 40 m/s*
- *Advanced flight: 50 m/s and side-slip angle (5 deg)*
- *Advanced flight: 60 m/s*

And the simulation condition adopted are:

- *Sea level Standard atmospheric conditions*
- *Coll = 9 deg*
- *LatCycl (A1) = 0 deg*
- *p = 0 rad/s*
- *q = 0 rad/s*

Again, the following additional useful rotor data are needed:

$$\begin{aligned}
 \epsilon &= 3e/(2R - 2e) = 0.0707 \\
 \sigma &= 0.0888 \\
 lock(\gamma) &= \rho acR^4/I_\beta = 5.3922 \\
 S &= m_b r_{cg}^2 \Omega^2 = 2.5517e + 05 \quad [Nm/rad]
 \end{aligned}
 \tag{4.21}$$

As already shown above, the Bramwell's formulations used for the comparison are, [2]:

$$\begin{aligned}
 h_c &= -[1/4\mu\delta + a1Cl_\alpha(1/6\theta_0 + 3/8\lambda + 1/8\mu a_1) - \mu\theta_0\lambda a/4] \\
 H &= \rho\Omega^2 R^2 A\sigma h_c \\
 \bar{M} &\approx -\bar{X}hR + 0.5Sea_1
 \end{aligned}
 \tag{4.22}$$

Moreover, for the validation of the moment (M), since the arm connecting the center of gravity of the helicopter and the hub is not known, it is decided to consider the rotor isolated as in the test rig by centering the center of gravity on the rotor. Therefore, the pitch moment shown in this case is only represented by the second component in the definition of the Eq. (4.22) unlike the XV-15 where  $e = 0$ , and only the effect of the first term exist. In the XV-15, in fact, the distance between the center of gravity and the hub is known from Ref. [7].

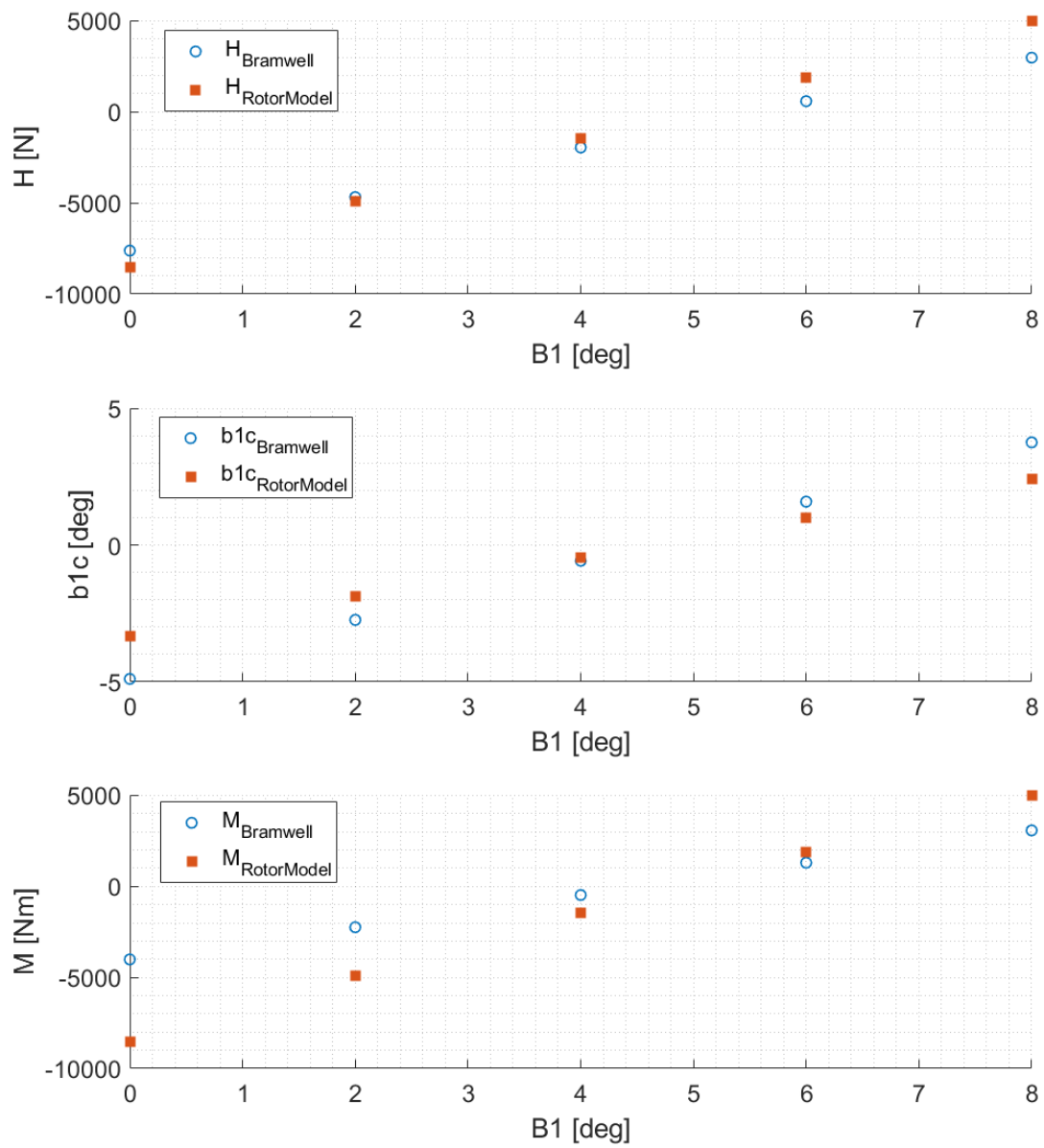


Figure 4.24: UH-60 in advanced flight  $u_h = 40m/s$

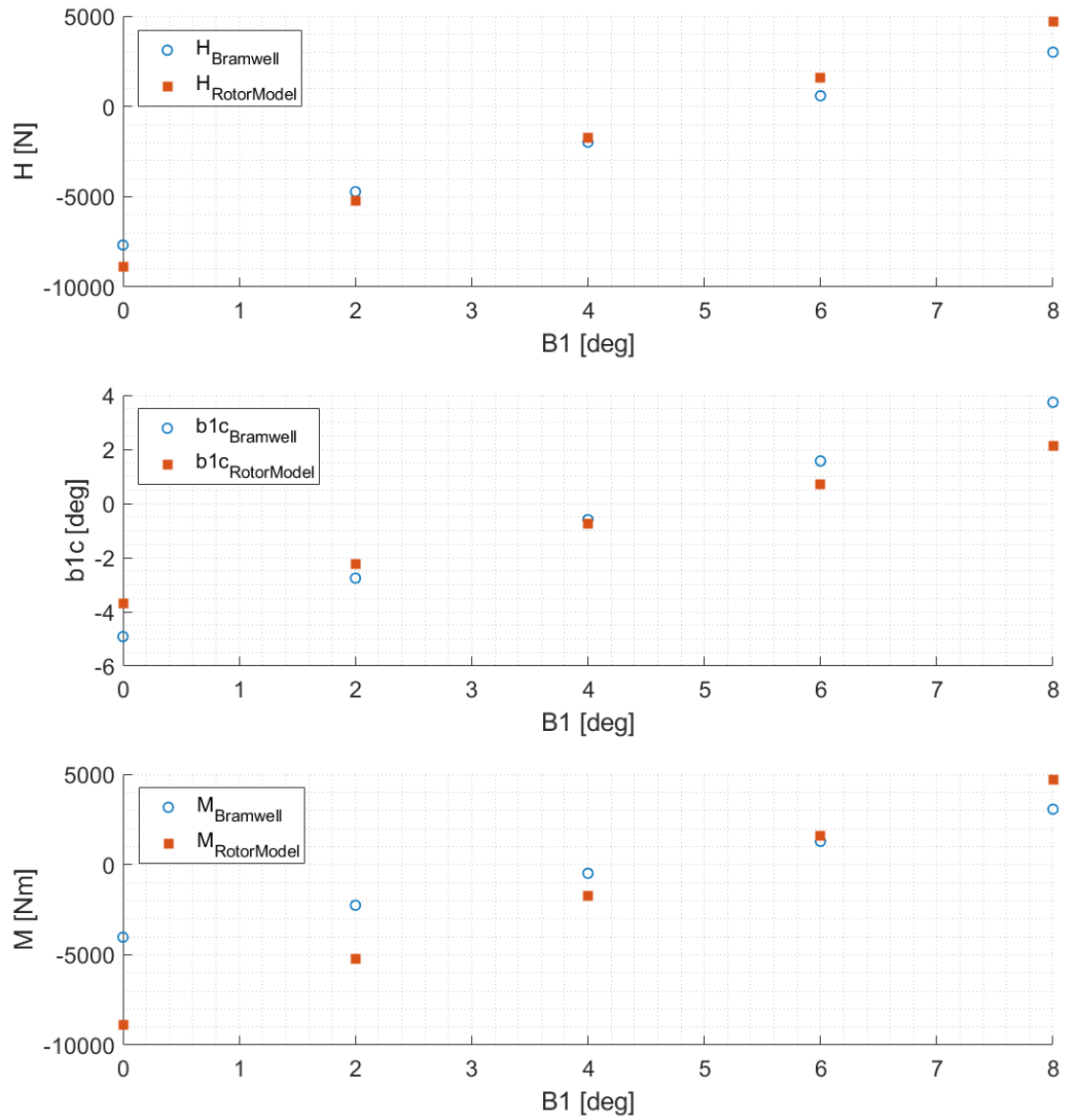


Figure 4.25: UH-60 in advanced flight  $u_h = 40m/s$ ,  $5deg$  of side-slip angle

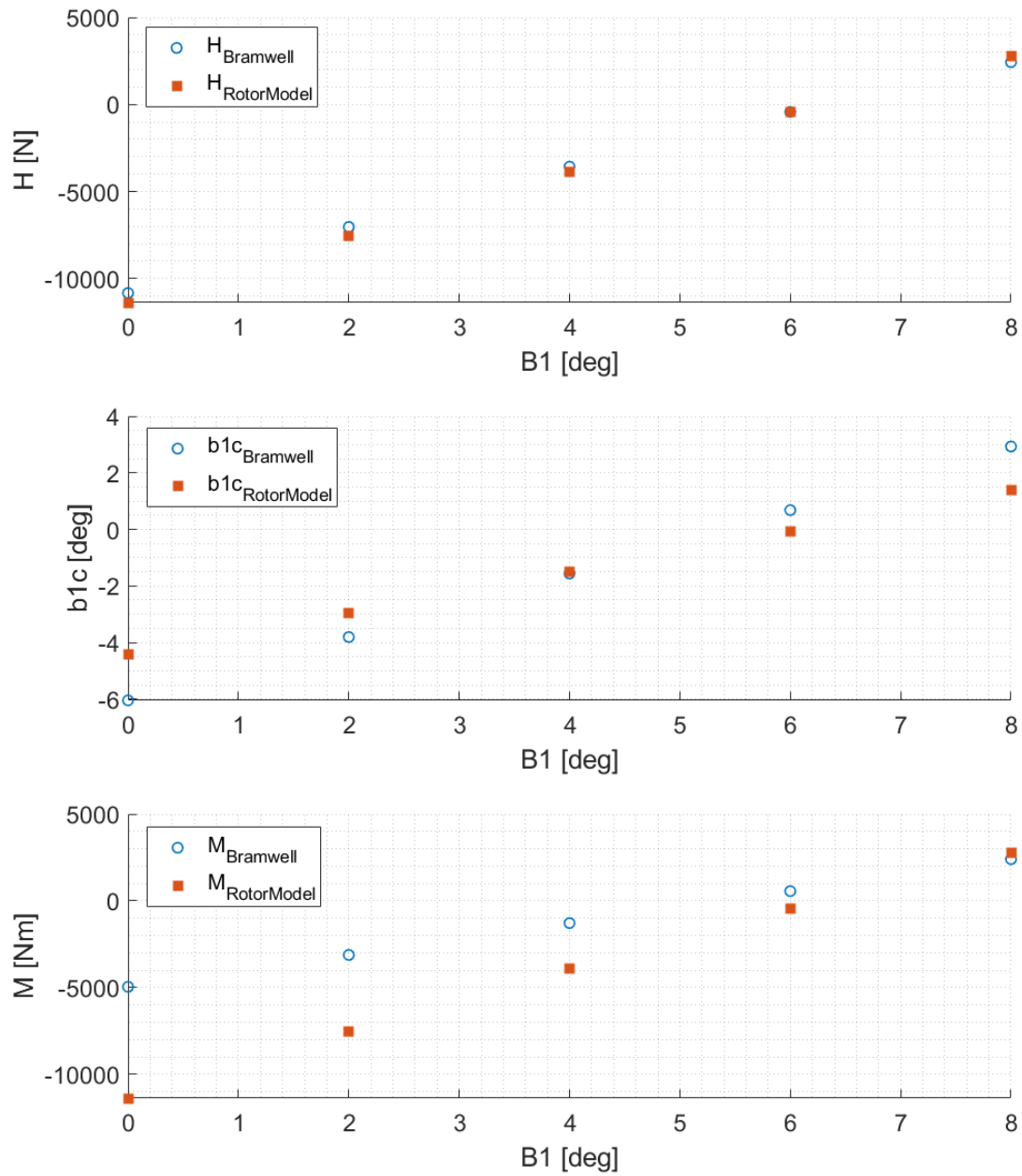


Figure 4.26: UH-60 in advanced flight  $u_h = 50m/s$

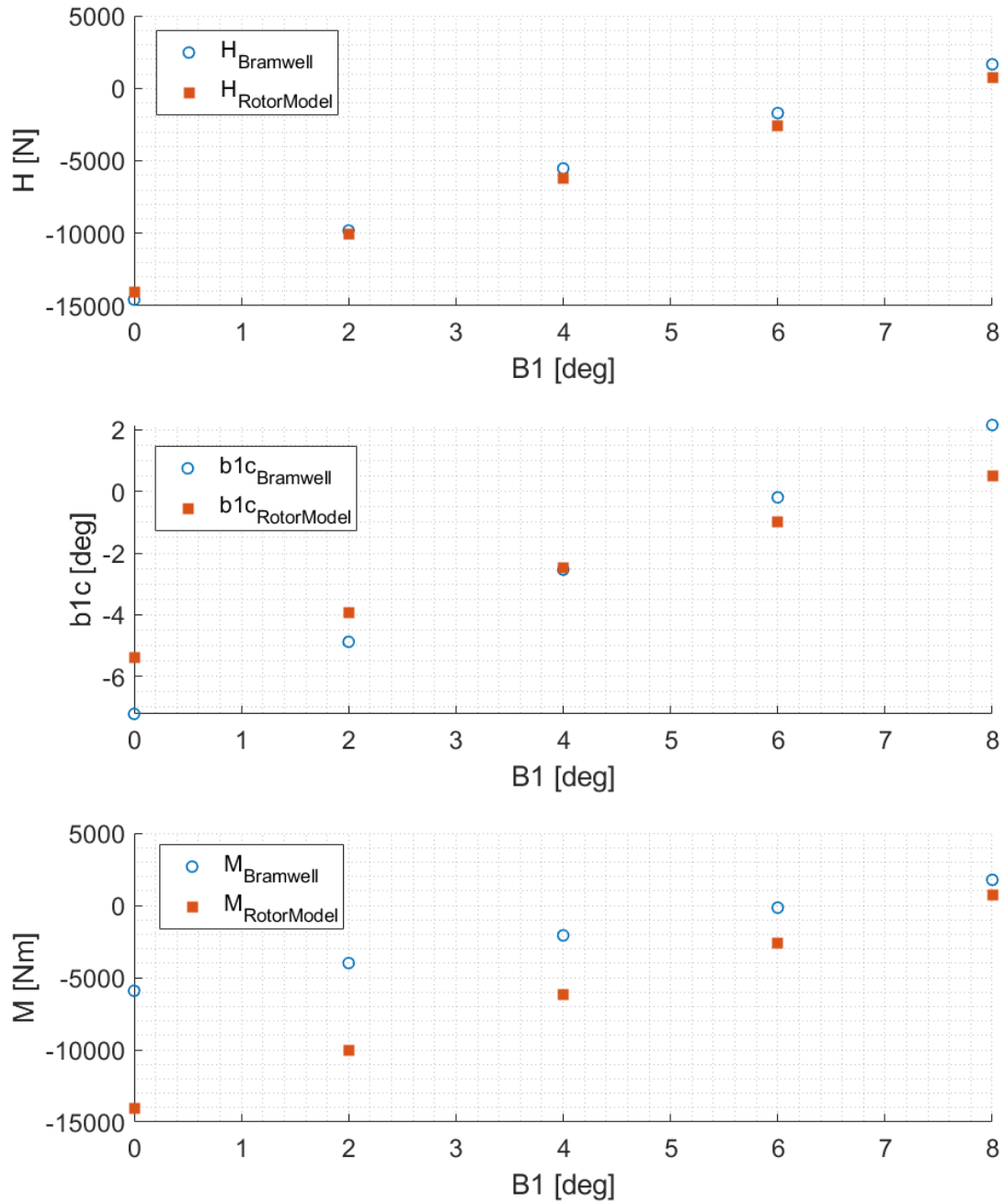


Figure 4.27: UH-60 in advanced flight  $u_h = 60m/s$

## 4.6 XV-15 Flight simulator testing

### 4.6.1 Introduction to the simulator

Once validated, the rotor model and the XV-15 simulation model already implemented are combined in order to meet the requirement for which it is created, real-time flight simulation. To get an overview, the overall model of a flight simulator has the function of processing all those data regarding the aircraft (rotor, aerodynamics, landing gears, inertia,..) and the surrounding environment (wind, flow density, pressure, temperature,..) in order to extract the overall forces and moments acting on the structure. In this way, for each temporal instant in which the discrete domain is divided (lower than the human eye's minimum perception), the speeds and accelerations of the aircraft are evaluated. Therefore, through the calculation of the Euler angles it is possible to represent on the screen, by means of an advanced graphic interface, the position, the speeds and all the data visualized by a pilot in a real cockpit. Thanks to the state-of-the-art flight simulator available to the University of ZHAW (Winterthur, Switzerland), several flight tests were carried out with the help of helicopter pilots with hundreds of hours of flight time. This, gave us a further and meaningful contribution for the validation of the rotor model and the entire flight simulator model. In fact, the aim is to have a feedback from the pilot on how much the aircraft is similar to the real version with respect to handling qualities. This was realized through appropriate tests that are presented in the following graph.



Figure 4.28: ZHAW flight simulator cockpit

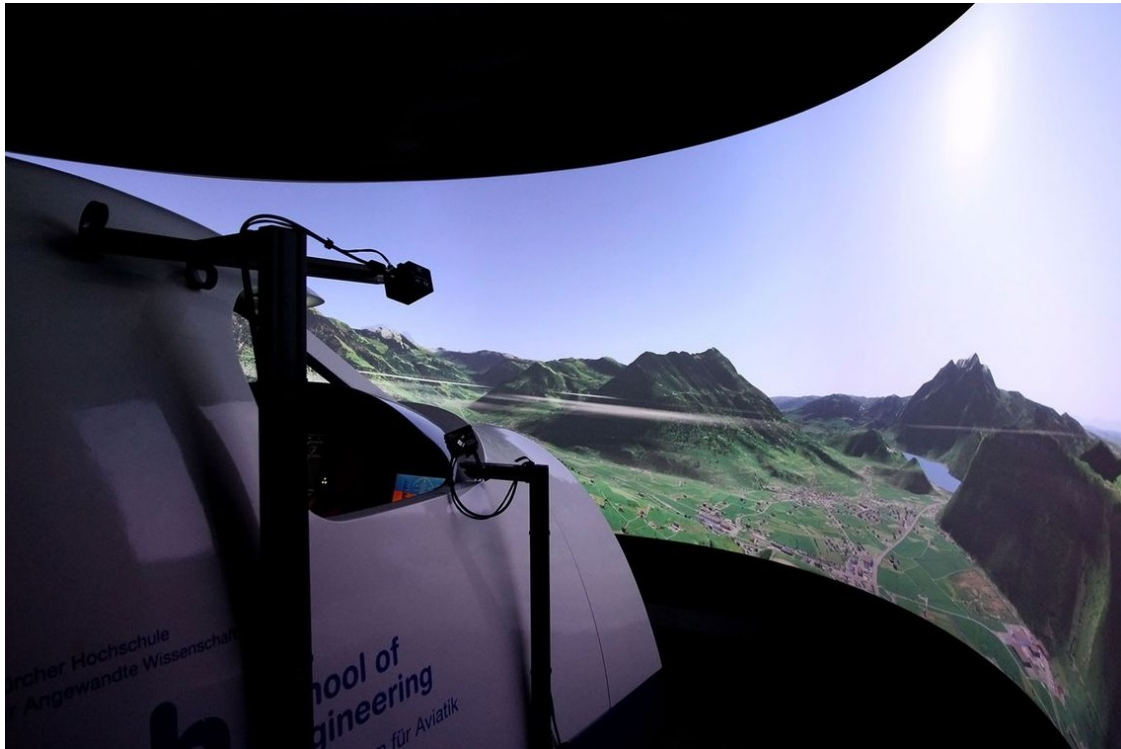


Figure 4.29: ZHAW flight simulator graphic

The whole system is designed and integrated by the ZAV's personnel and by the students of ZHAW and it is being improved constantly since 2011. This Simulator is now used for educational activities, research as well as for industrial purposes together with partner companies (Pilatus Aircraft Ltd. used of the ReDSim for the development of PC-24). As shown in the images, the cockpit of the simulator is equipped with configurable displays, created for applications on fixed-wing aircraft. However, it is also possible to use it for helicopter flight simulation, in fact, the right seat is actually used for flying in this second mode through the installation of the cyclic control stick and the introduction of the collective for the helicopter control. In addition, this particular simulator is equipped with a control handling system. In order to make the flight mission as truthful as possible, there are three graphic projectors working on a curved screen, as shown in the figure above. This, in order provide the pilot a better perception of the depth and three-dimensionality of the image, making the flight mission as real as possible. In addition, the maps that are loaded into memory and on which the aircraft can move, are real area of Switzerland, and shows not only runways and landing ones, but also with landmarks such as: mountains, antennas, houses and trees that are truly useful to carry out different validation maneuvers such as hover, vertical and horizontal repositioning, as well as the classic take-off and landing, as it is shown below.

## 4.7 XV-15 flight simulator test in helicopter mode

The first flight test was performed in order to carry out the maneuvers already mentioned above; the aim is to verify as fully as possible the operation of the XV-15 in helicopter mode. Therefore, thanks to the collaboration of the experienced pilot Davide Buscetti, the following maneuvers are carried out. The flight time of this test is approximately around 20 minutes, during which the pilot has the time to become familiar with the aircraft by repeating the different maneuvers several times. This, allows the pilot to make a concrete judgment on the flight quality of the aircraft. All operations with their respective time instants and any pilot comments are recorded as follows.

### 4.7.1 Flight test time sequences

All the flight phases described below are listed in chronological order with the simulation time at which the event is recorded next to them. In addition, as anticipated, where the pilot released a comment, it is reported faithfully.

Flight simulation time sequences:

1. *Centering on the track on the ground (timeSim: around 40 sec)*
2. *Take-Off (timeSim: around 70 sec)*
3. *Uniformly accelerated flight up to 60 kts -> the pilot records stable flight above 50 kts (timeSim: from 70 sec to 140 sec)*
4. *180 degree turn (timeSim: around 150 sec)*
5. *Speed reduction up to 30 kts -> the pilot still records stable flight (timeSim: from 160 sec to 180 sec)*
6. *Speed reduction up to 15 kts -> the pilot works more with pedal to keep the aircraft stable (timeSim: from 180 sec to 241 sec)*
7. *Attempt to hover -> strong pitch oscillation -> Hover failed, the pilot gives collective and takes speed to stabilize the aircraft (timeSim: from 270 sec to 300 sec)*
8. *180 degree turn and 2nd Hover approach (timeSim: from 330 sec to 380 sec)*
9. *Speed reduction for 2nd hover attempt (timeSim: from 380 sec to 410 sec)*
10. *Hover succeeded (timeSim: from 410 sec to 420 sec)*
11. *Acceleration and fast 180 deg turn (timeSim: around 450 sec)*
12. *Speed reduction and 3rd hover approach (timeSim: from 460 sec to 500 sec)*

13. *Hover succeeded (timeSim: around 520 sec)*
14. *Acceleration and 180 deg turn (timeSim: around 570 sec)*
15. *Speed reduction for 4th Hover-> the pilot notes that the pitch control and pedal have to be improved (timeSim: around 580 sec)*
16. *Hover failed (timeSim: around 630 sec)*
17. *Acceleration and uniform straight flight at 50 kts (timeSim: from 650 sec to 670 sec)*
18. *Turning at 180 deg (timeSim: around 680 sec)*
19. *Speed reduction (timeSim: from 709 sec to 780 sec)*
20. *Hover succeeded (timeSim: around 783 sec)*
21. *Hover again (timeSim: around 811 sec)*
22. *Repositioning near antenna (timeSim: from 840 sec to 860 sec)*
23. *Slow cross repositioning (timeSim: around 890 sec)*
24. *Approach over the 'X' and hover succeeded over (timeSim: from 927 sec to 965 sec)*
25. *Repositioning near the antenna and hover succeeded-> the pilot works constantly with the pitch control to hold the Hover (timeSim: from 980 sec to 1014 sec)*
26. *Light pitch oscillation (timeSim: from 1059 sec to 1108 sec)*
27. *Horizontal repositioning on the track (timeSim: from 1147 sec to 1178 sec)*
28. *Horizontal repositioning (timeSim: from 1214 sec to 1232 sec)*
29. *Landing near the 'X' (timeSim: around 1316 sec)*

As can be seen from the sequence described above, the flight test ended without fatal failures. However, the aircraft is not fully stable as can be deduced from some failed maneuver attempts. Therefore, what follows is a detailed analysis of the results collected during the test, realized in order to understand what is the nature of the instabilities in question and what is their entity. Moreover, the main purpose remains that of verifying if the simulation model is faithful representing or not to the reality; also for this reason a more in-depth analysis of the data is required. This is especially possible thanks to the experience of the pilot.

## 4.7.2 First overview of results

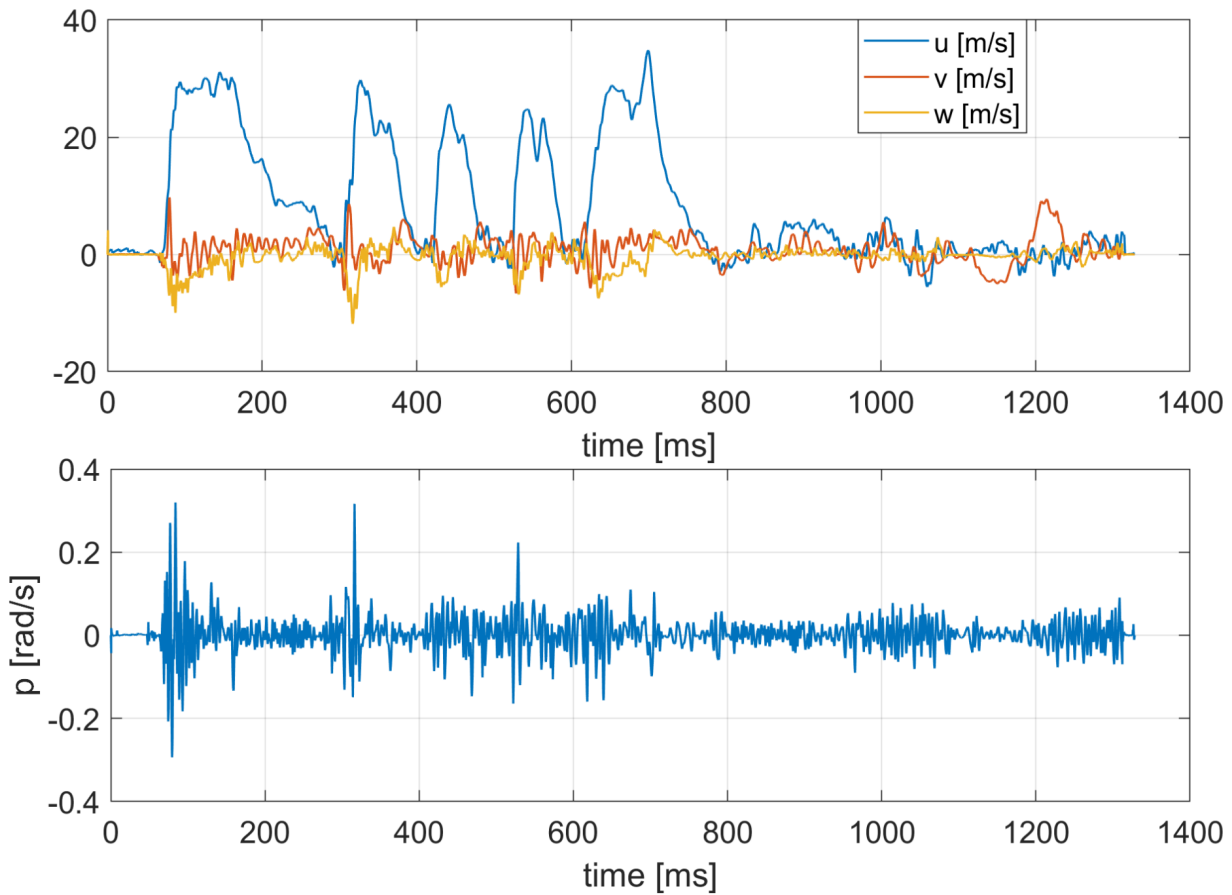


Figure 4.30: Translational speeds and roll rate

The figure above shows the trends of the translational speeds and the angular rate around the rolling axis ( $p$ ) during the whole test. In particular, from the areas where the axial velocity ( $u$ ) is constant, it can be seen that the pilot is conducting the aircraft or in a 180 deg turn at a constant speed or in uniform straight flight after an acceleration. What is more, the areas where a peak in the ' $p$ ' rate is recorded indicate the phases where the pilot is making a turn. In this particular test, only 180 deg turns are realized in order to approach several times the track and the references to test in detail the hover and the repositioning maneuvers. In addition, it is notable that the translational velocity ' $v$ ' oscillates and the vertical rate ' $w$ ' are  $\ll u$ .

From the figure below, in fact, it is possible to notice the pitch instability shown by the aircraft at low speeds just mentioned. In particular, from the graphs in question, it is evident how the phases where the aircraft approaches the condition of hover ( $u \rightarrow 0$ ) correspond precisely to a significant increase in oscillations in terms of angular rate around the pitch axis ( $q$ ).

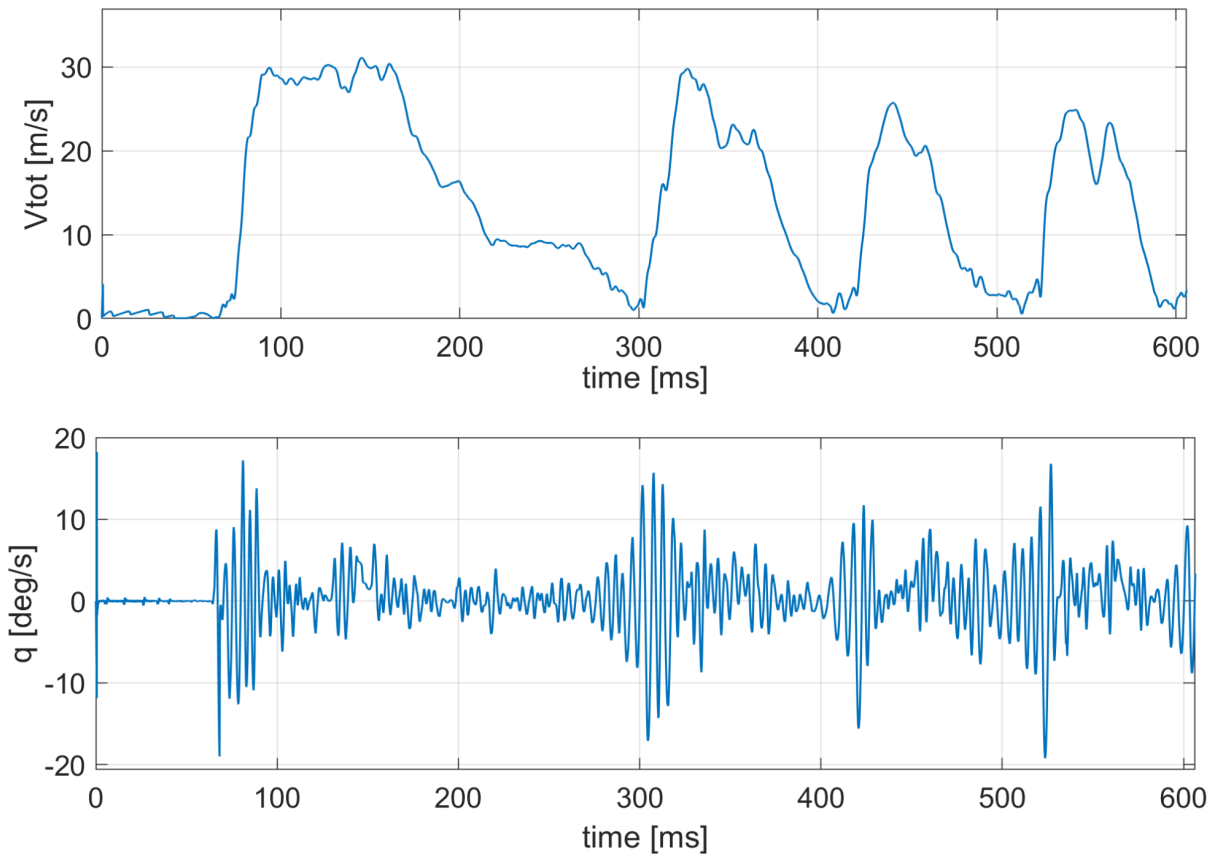


Figure 4.31: Flight test results: translational speeds and pitch rate

These oscillations are so strong that they do not allow the pilot to reach Hover conditions until after a few attempts. In fact, it is difficult for him to stop the phenomenon by compensating only with the longitudinal cyclic. This happens because of the high inertia of the aircraft along this axis; that, at low rates is problematic to control especially considering that it is not possible to increase the collective to have a more effective the longitudinal cyclic command without leaving the hover condition. However, when the amplitude of the oscillations becomes too meaningful, rising the collective and thus moving away from the condition of Hover is the only possible solution for the pilot to regain control of the aircraft. Therefore, several 180 deg turns are made to approach again the references and try to bring the aircraft into hover through a new, slow and gradual deceleration until this flight condition is satisfactorily achieved.

### 4.7.3 Take-off

The first meaningful maneuver that deserves an in-depth analysis is the take-off. In this case, the pilot doesn't choose to take-off through the classic vertical take-off maneuver that sees the helicopter only ascending from the point of departure. However, the type of take-off applied is called 'rolling take-off'. To realize it, the pilot acts on the longitudinal cyclic and on the lateral control simultaneously in order to give an axial speed to the aircraft along the runway. This allows the aircraft to take advantage from the load-lifting effect of the wings as well as the traction of the two rotors to facilitate the take-off maneuver.

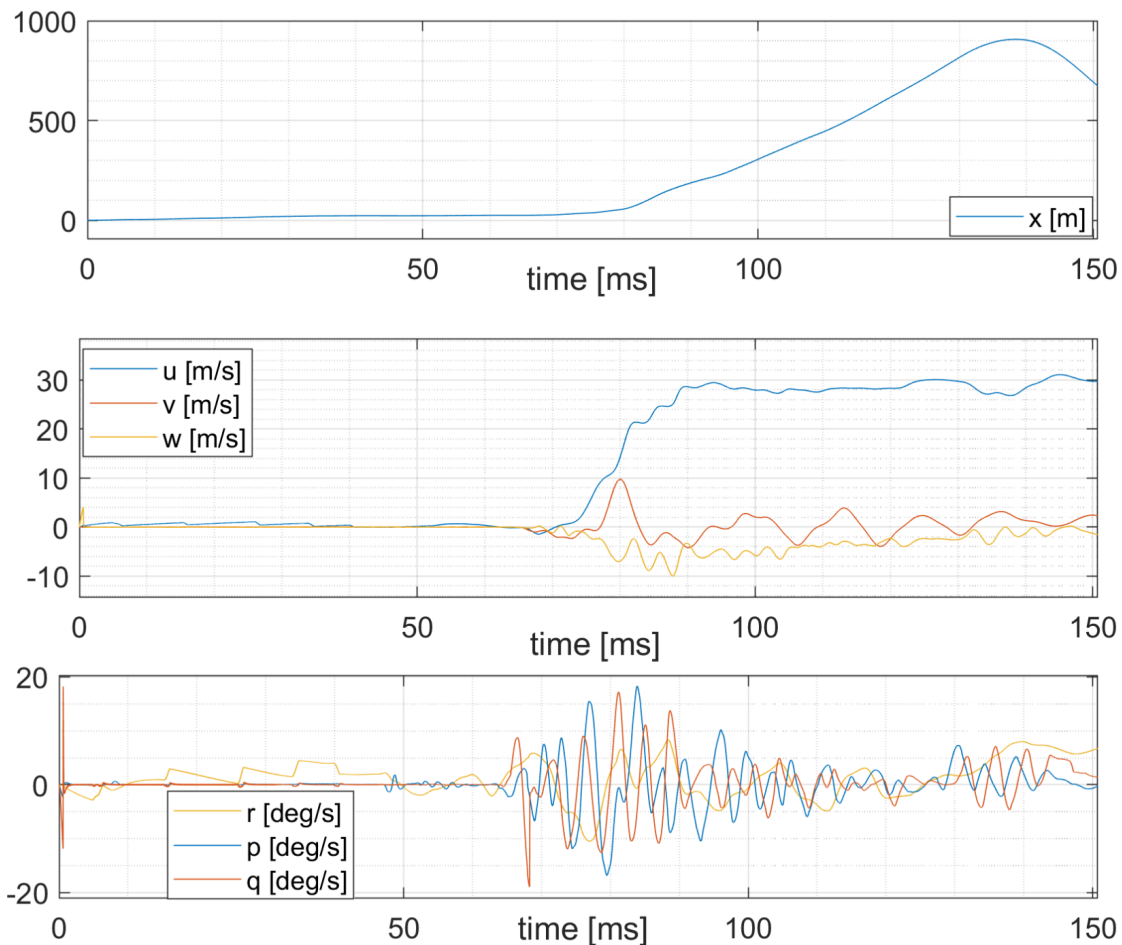


Figure 4.32: Speeds and position during take-off

The figure above shows how the rolling take-off phase, which begins around the 70th second, generates oscillations in the angular rates of roll and pitch ( $p$  and  $q$ ) in order to increase the axial speed ( $u$ ) and then the wing effect of the aircraft. In fact, it is possible to see how the latter speed grows considerably during the take-off phase. This acquired axial velocity is translated into a component  $x$  variation of the position vector as shown in the 1st curve.

#### 4.7.4 Hover condition

Analyzing the time range between the 951 sec and the 980 sec, it is notable how Hover's attempt is satisfactory. In fact, enlarging the trends is found that:

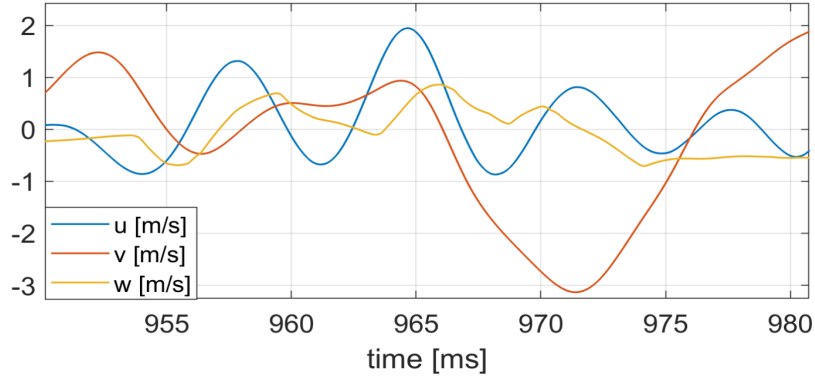


Figure 4.33: Translational speeds in hover

Therefore, from the figure above it can be seen how in this range of time all the three translational rates are truly law, except for an oscillation of the 'v' rate which starts around the 965 sec. Naturally, it is not possible to see the flat speed curves coinciding with the null value. However, this can be considered a positive result. As proof of this, the following figure shows how the vector position remains almost unchanged in this time range:

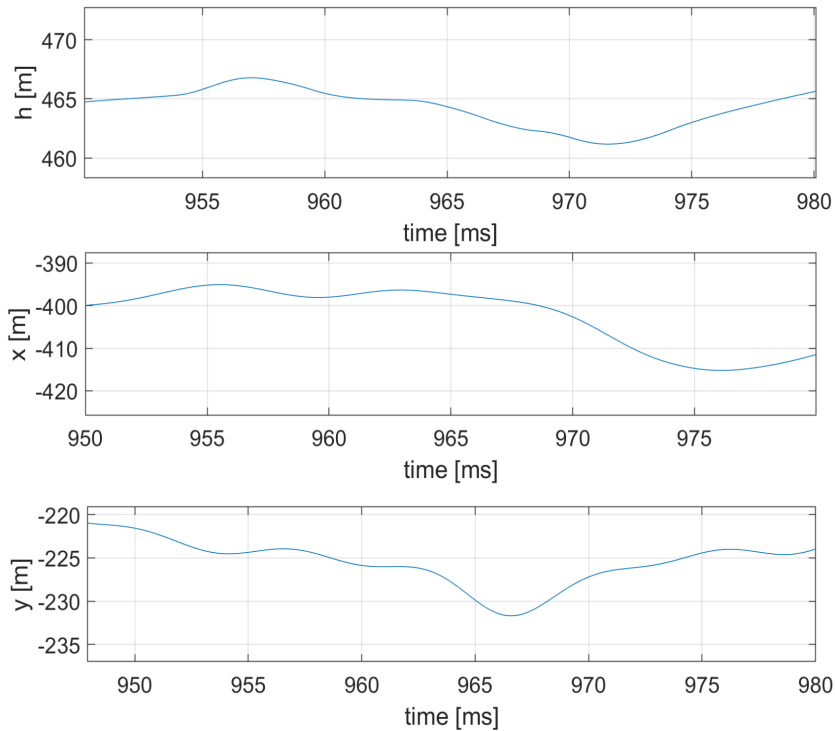


Figure 4.34: Vector position's components in hover

However, as previously announced, not all attempts of hovering during the test are successful. From the following image, in fact, are shown the rotational and translational speeds related to a period of time of the test during which the pilot is forced to escape from the hover condition because of a meaningful instability in the pitch axis that is unmanageable for him.

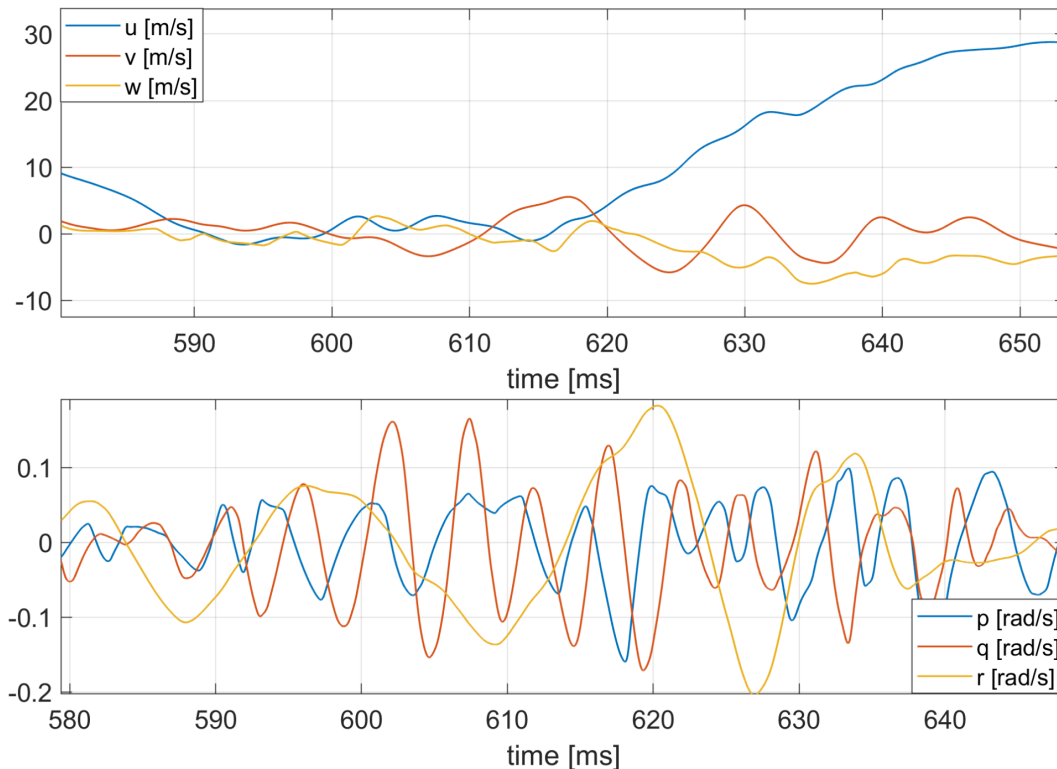


Figure 4.35: Pitch instability in hover

As a proof of this, from the figure above it is clear that during the hover attempt the amplitude of the oscillations in terms of pitch angular speed ( $q$ ) increases considerably, until the pilot, in order not to lose totally the control of the aircraft, is forced to rise the collective and evade in a translated flight maneuver. In fact, it is shown how, once out of the hover condition, in the range of time where the axial speed ( $u$ ) increases, the oscillations in question are brought back to lower values. However, it should be noticed that this instability is not necessarily due to an error during the implementation or in the mathematical model. In fact, aircraft of this type with such high moments of inertia enter in the category of the most difficult machines to pilot, especially without an stability augmentation (with which the model is not yet equipped). This is why the use of tilt-rotors is not yet widespread in the civil aeronautic, as well as for their high structural and constructive complication. Therefore, according to the pilot, who is specialized in helicopter flight, the model could represent the real aircraft in a satisfactory way despite this problem.

To see even more of this pitch instability, the Euler angle are shown in the following image.

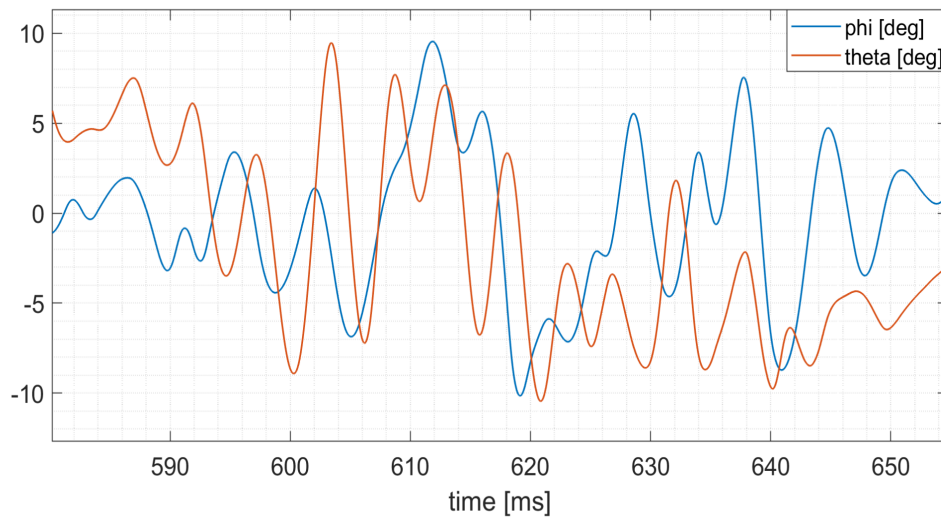


Figure 4.36: Euler angles during pitch instability in Hover

How it is notable, the oscillation in terms of pitching and rolling Euler angles (theta and phi) are quite intense, and they extend until the amplitude value of 10 deg.

#### 4.7.5 Straight and level flight

Another meaningful phase of flight where the handling qualities of the aircraft are tested is the uniform straight flight. In fact, it is essential for any aircraft to be able to flight through long phases of the mission in this mode. Therefore, it is clear how important is the validation of the aircraft's response to external commands and disturbances even during this maneuver. Again, below, the behaviour of the translational and rotational speeds during this phase are first analyzed.

In the following graph is possible to see that the uniform straight flight phase begins around the 80th sec. It is interesting to notice how, during the acceleration phase before reaching the desired condition, the stability of the aircraft grows steadily. In fact, at low speed, high oscillations in the angular rates ( $p, q$  and  $r$ ) are notable, which are gradually dumped as the axial velocity ( $u$ ) increases. Also, it can be seen that the machine at high speed is more stable than at low rates, as expected. This, is due to the fact that with increasing of speed all the aerodynamic control surfaces of the tilt-rotor (ailerons, rudder, tail,...) becomes more and more effective. Following the curves of the angular rates for all the duration of maneuver, shows how there is a peak (around the 150th second) where appears a slight instability, understandable as 180-degree turn match. Once completed the uniform straight flight phase, a deceleration is performed in order to approach the hover and the repositioning maneuver. It is evident that the deceleration is truly gradual. In fact, the slope of the curve is considerably

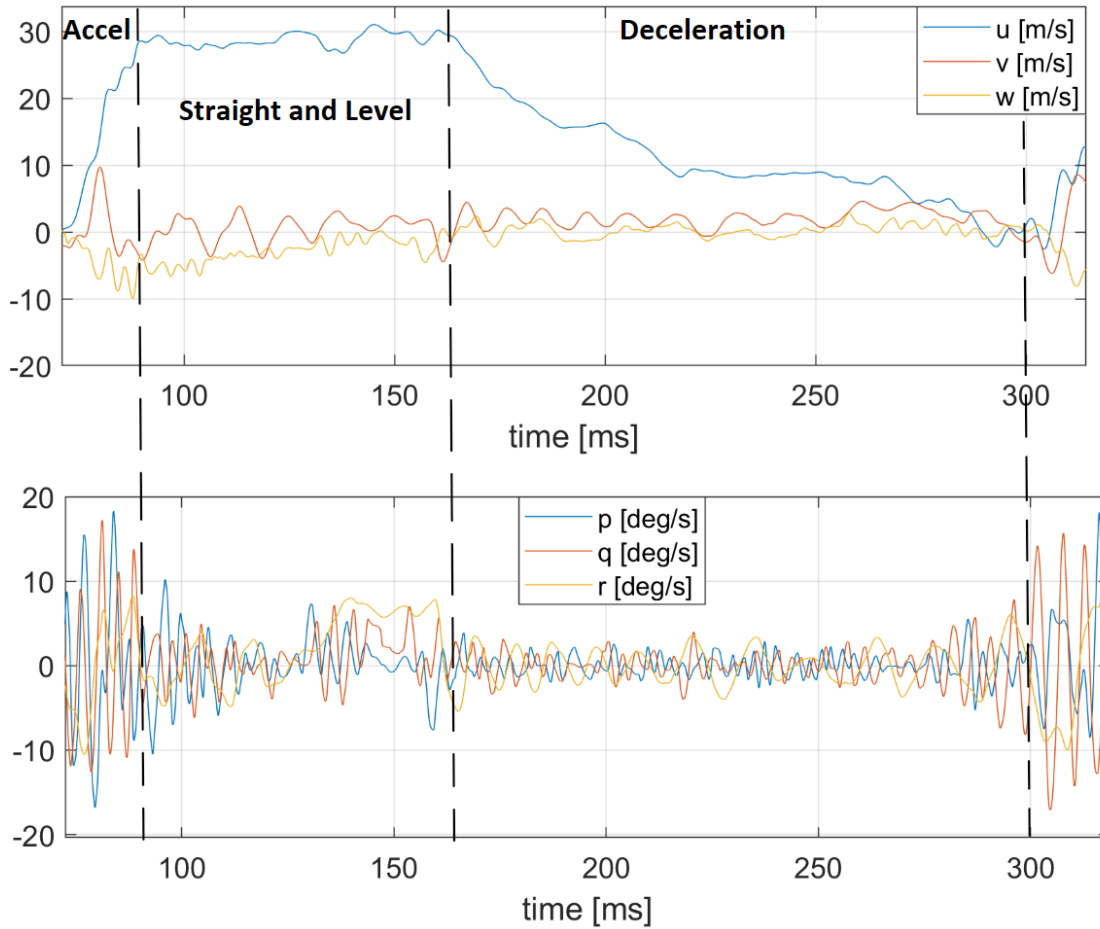


Figure 4.37: Translational and rotational speeds in uniform straight flight

lower compared to the acceleration phase. This long approach executed by the pilot is successful because it allows him to conduct the aircraft up to low speed without losing the stability gained previously, allowing him to approach in the best possible way the subsequent phases of flight.

From the curves of the Euler angles represented below, for the same temporal interval of the mission, it can be seen how the straight and level flight phase is conducted in a stable way except for that period of time mentioned above where a short but intense peak in the attitude angle around the pitch axis (theta) is notable; that occurs during the turn as witnessed by the variation of the roll angle (phi) in the same range of time, Fig. 4.38. Moreover, as previously announced, during the acceleration phase, it is notable a damping of the oscillations not only of the angular rates, but consequently of the Euler angles also, which constantly decrease their amplitude. While, during the remaining part of the maneuver it is shown how the angles of trim are maintained at values around zero, oscillating with reduced and controlled amplitudes even in the phase of deceleration and approach to the following maneuvers. Finally, it can be noted, that once reached the condition of hover (around 300 second), the amplitude of the oscillations

starts growing again. In fact, visualizing the data shown in the previous section of 'First overview of results', is possible to see how this straight flight phase is followed by the first attempt of hover, ended with negative result. This is because the pilot, at the beginning of the test, is not yet completely aware of the pitch instability of the aircraft, and therefore he has to deal with strong oscillations for his authority on the command at those speed. Therefore, he is forced to increase the power and evade in a new phase of translated flight to avoid losing completely control of the aircraft.

#### 4.7.6 180-degree turn

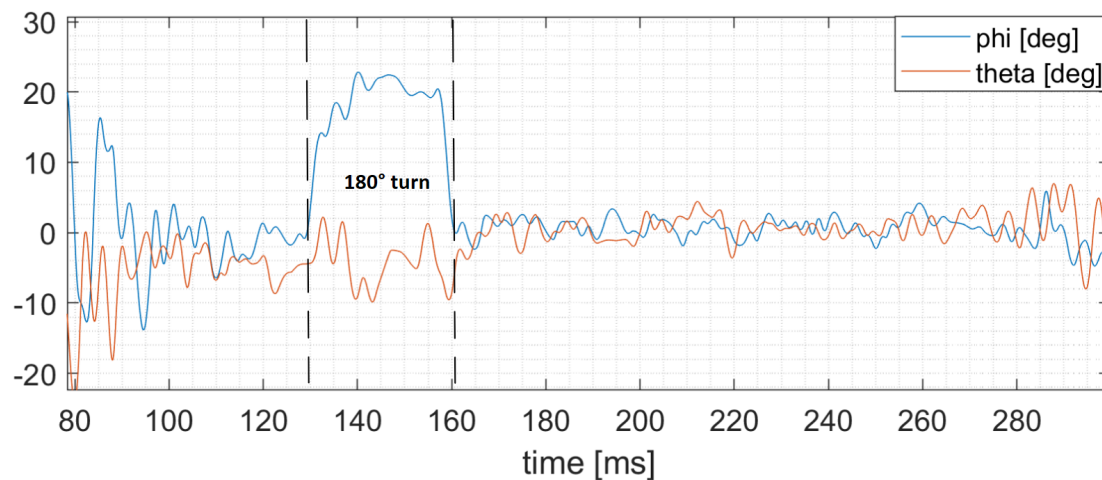


Figure 4.38: Euler angles curves in uniform straight flight

It is also interesting to analyze in detail, the first turn performed with a positive result. As previously announced, it is carried out during the first phase of uniform straight flight (around 150 sec), to approach again the runway where there are the various references useful for subsequent maneuvers. Below are shown the trends of the translational and rotational rates with the angles of Euler recorded during the maneuver.

From the quantities represented in the graphs is possible to see how the turn is executed at constant speed, in fact, there is no considerable variation in the axial speed ( $u$ ) except for some slight oscillation. Moreover, it is interesting to observe the trends of the angular rates. Here, it is shown how the roll speed increases while the aircraft is changing its initial attitude toward the correct angle as the curve of Euler angle 'phi' testifies. In addition, a slight instability on the pitch axis arises again, but it is well managed by the pilot in this case. Instead, once the turn attitude is reached, the angular roll speed ( $p$ ) is dumped and set at a constant value, reducing completely its oscillations. Naturally, later there is an increase in the yaw rate ( $r$ ), which also greatly reduces its oscillations during the maneuver. During this range of time, as expected, the roll angle (phi) is almost constant. At the end of the turn (around 160th second), when the aircraft returns

to its initial attitude, it is shown how the angular speeds are dumped and they return to oscillating around the zero value in view of the deceleration and of the approach to the following maneuvers.

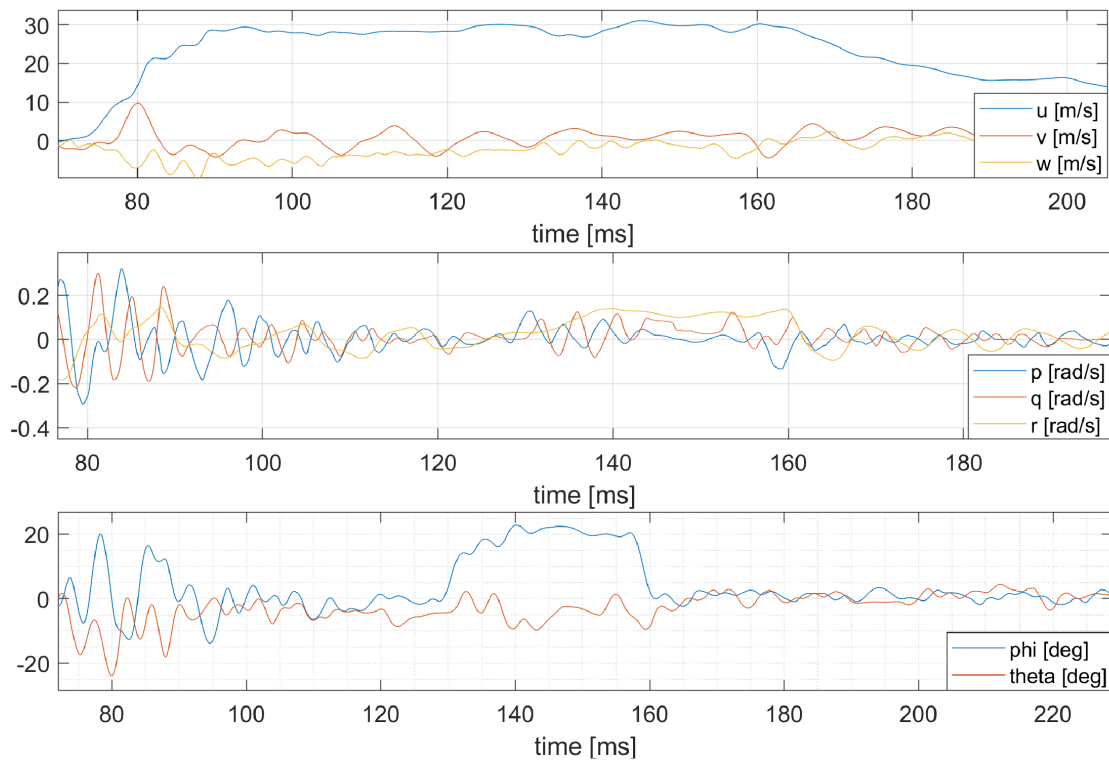


Figure 4.39: Euler angles and speed rates during 180-deg turn

#### 4.7.7 Lateral repositioning

Another maneuver performed evaluated, is the horizontal repositioning. It consists in a translation of the aircraft at a constant altitude between two precise reference points. Therefore, the following figure shows the results of this maneuver in terms of translational and rotational speeds again. In particular, in the trends two consecutive horizontal repositioning maneuvers in opposite directions are notable. It can be seen that while the two translational speeds ' $u$ ' and ' $w$ ' tend to be zero, the horizontal speed assumes meaningful values due to the fact that the aircraft is mainly moving along  $y$ -axis. Therefore, once the desired point is reached (around the 1180th second), a repositioning maneuver along the positive  $y$ -axis begins, which also ends successfully (around the 1240th second). As proof of the stability of the maneuver, can be noticed that the trends of the angular rates although still oscillating, they maintain values sufficiently small. This maneuver is particularly meaningful, as it is essential for the pilot to understand if is able or not to conduct the aircraft in a stable manner and along a well-defined trajectory even at low speeds. This could be especially important in those missions where the flight and landing spaces are tight.

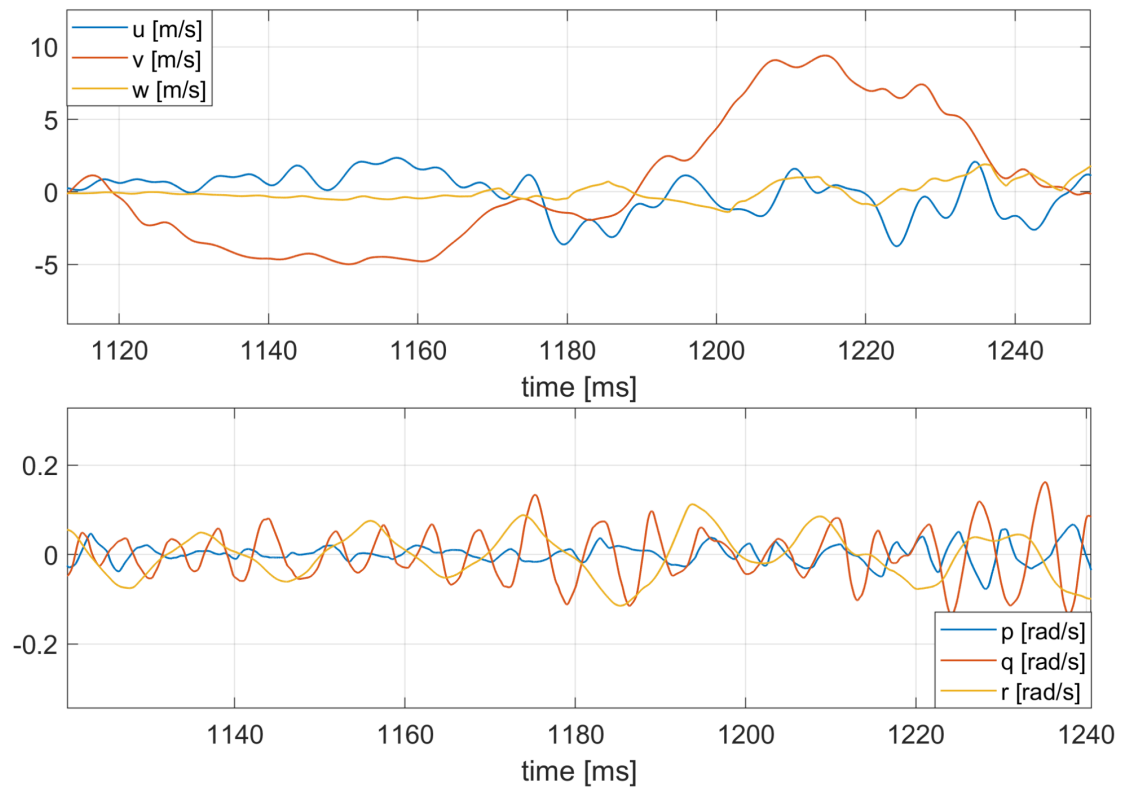


Figure 4.40: Horizontal positioning's translational speeds and rotational rates

It is also interesting to understand how the XV-15 and other tilt-rotors act on the lateral position. In fact, having the lateral cyclic blocked, they use a difference between the collectives of the two rotors thus creating a delta between the two thrust and therefore a rolling moment.

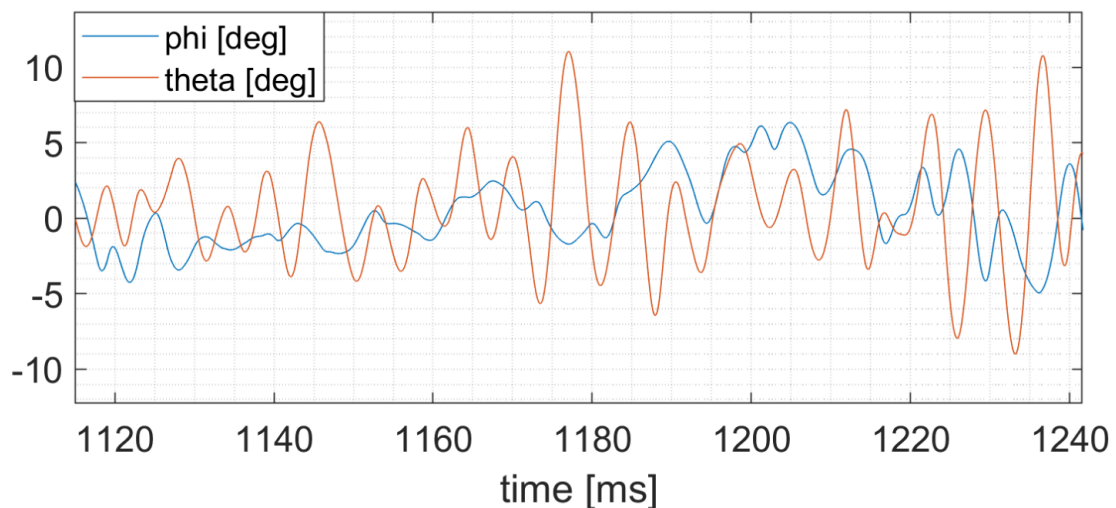


Figure 4.41: Euler angles during horizontal positioning

To better visualize this phenomenon, the figure above shows the trend of the

Euler angle around the rolling axis ( $\phi$ ). It is evident that during the repositioning phase, the latter is maintained at mean values other than zero and then reversed when starts the second phase. Naturally, for each of the two relocation there is a periodic trend of the sign of the angle in question, this is because to stop the aircraft at the desired point of arrival the pilot provides a command in the opposite direction to the initial one. Instead, the other Euler angle in the figure ( $\theta$ ) shows how, in this case the pitch instability is still present, but well kept under control by the pilot throughout the maneuver. In fact, the trends prove that the amplitude is well controlled, except for the change of direction where there is a slight increase in the phenomenon.

#### 4.7.8 Longitudinal repositioning

Another maneuver performed to evaluate with the pilot the flight qualities of the model, is the longitudinal repositioning. Again, it consists in a translation of the aircraft at a constant altitude between two precise reference points, but along the x-axis of the aircraft in that case. Therefore, the following figure shows the results of this maneuver again in terms of translational speeds and the variation of the x-coordinate.

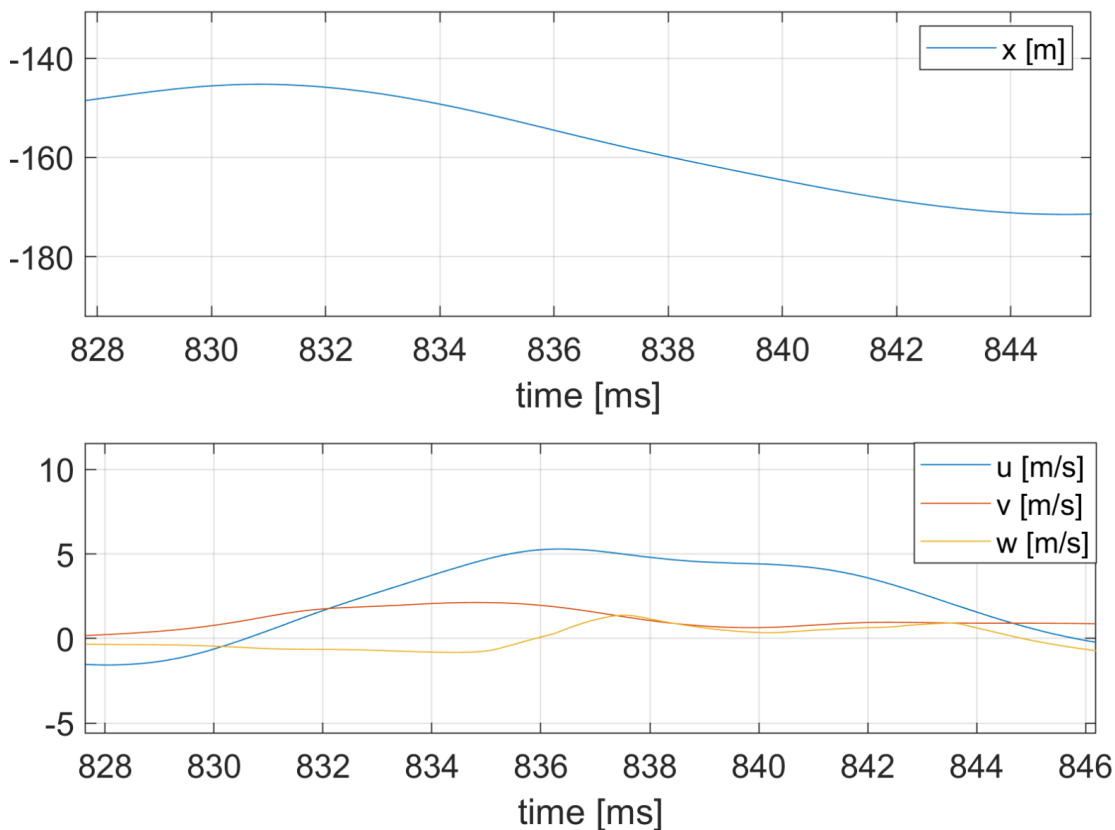


Figure 4.42: Translational speeds and x-position during longitudinal positioning

Unlike the horizontal positioning maneuver, in this case, it is possible for the pilot to act directly on the longitudinal cyclic without having to play on any differential between the two rotors. Therefore, from the figure above it is possible to see how the speeds tending to the zero value in this maneuver are 'v' and 'w'. While, it is possible to notice that the axial velocity 'u', undergoes first an increase, and then it decreases due to a deceleration in order to end the maneuver with a hover near the reference landmark. The trend of the maneuver can also be followed in the curve of the component x of the vector position represented above. The graph shows how an increase in the axial speed 'u' corresponds to a reduction in component 'x' (positive oriented towards the tail of the aircraft). After that, the reduction of speed to settle the arrival point, manifests itself in a change of slope in the course of the same x-component until it settles at a constant value once reached the phase of hover next to the reference.

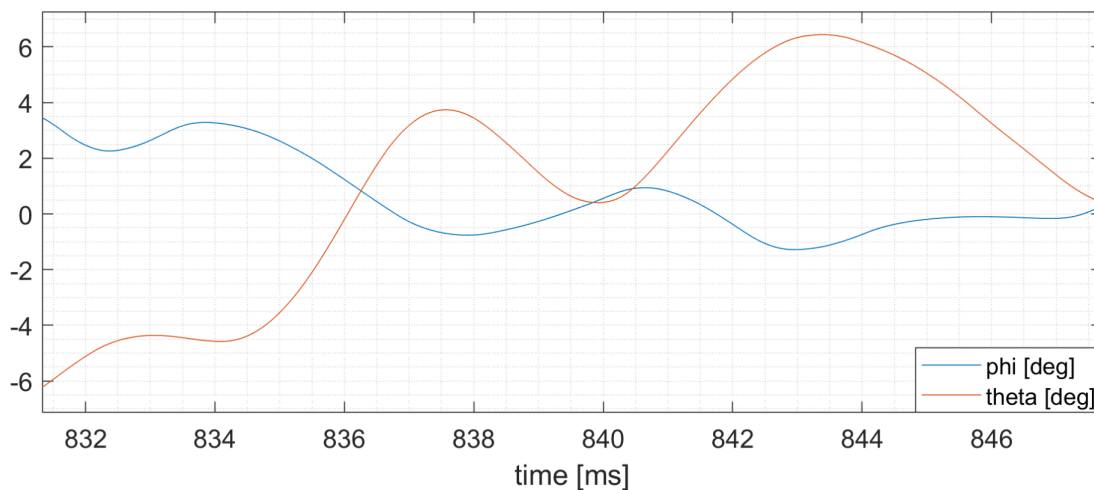


Figure 4.43: Euler angles during longitudinal positioning

Also, for this maneuver it can be seen how the longitudinal cyclic control translates into a change of attitude of the aircraft. Specifically, during the longitudinal translation, it is shown an increase in the pitch angle (theta), which then decreases during the deceleration phase. The pitch oscillations seen above are substantially more stable in this maneuver. Instead, the fact that the values of the angle in question start from negative values is because the center of gravity of the aircraft is located more towards the tail with respect to the traction axis in this case. Therefore, a negative pitch moment is created during the advancement phase. Moreover, from the angle of roll (phi) represented in the same graph is shown how the maneuver results stable, in fact, it is maintained around zero. To conclude, it is remarkable that even this maneuver is stable and successful, although the pilot must always compensate a lot on the pitch axis to stabilize the aircraft, as is possible to read in the comments listed before in the time sequence.

### 4.7.9 Landing

The mission ends with a landing near the reference (antenna) after the repositioning and hover maneuvers. In the following image, the trends of the translational and angular rates, together with the Euler angles recorded during this maneuver, are analyzed again in detail.

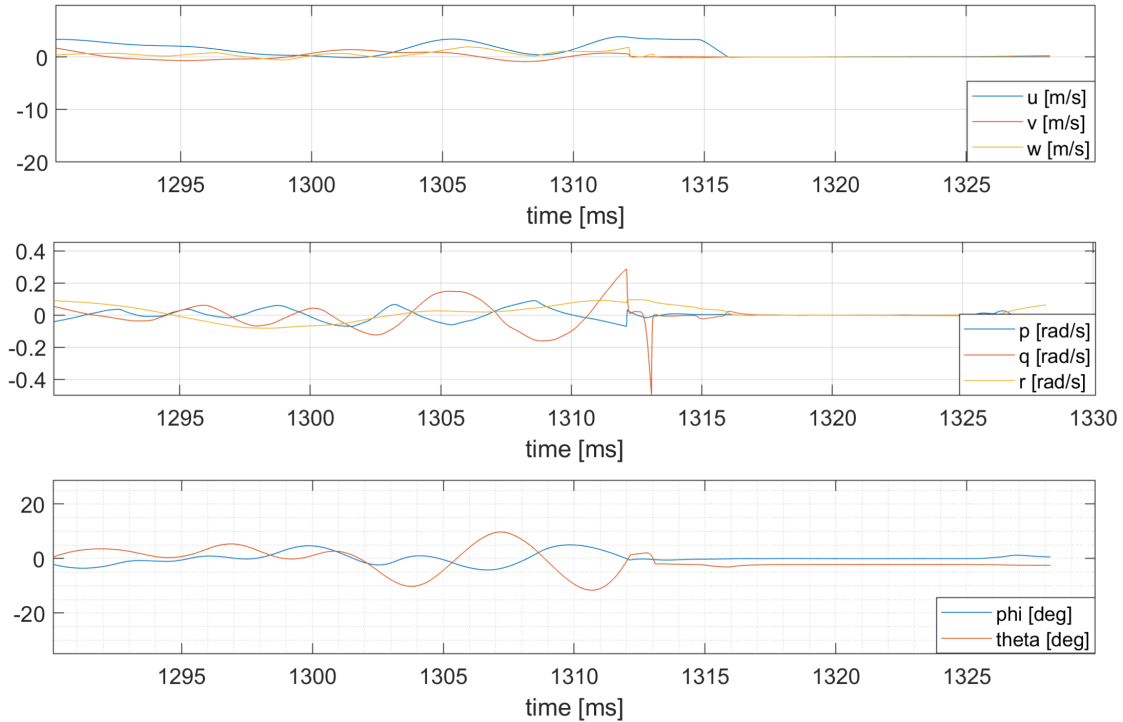


Figure 4.44: Euler angles and speeds during landing

From the trends of the translational speeds it can be seen that the moment of the 'touch-down' is easily recognizable, in fact, the slight and rapid oscillation in the curve of the rate of climb 'w' testifies it. This particular step is created by the slight rebound of the aircraft in contact with the ground, which consequently causes a reversal of the sign in the speed considered. At the same time it is possible to see how, in the trend of the angular rate 'p' there is an intense oscillation. In fact, as it is shown in the trend of Euler angle, 'theta', the pilot finds himself approaching the landing with a considerable instability in the pitch axis, and he tries to alleviate through the use of the longitudinal cyclic. In addition, in the moment of contact with the ground there is a strong negative peak in the roll rate. Finally, it is interesting to note that at the end of the maneuver, when the aircraft is completely stopped, the pitch angle (theta) is set at negative values. This inclination of the bow towards the ground is due to the fact that in this aircraft the front carriage is lower than the rear ones for construction reasons. In the last instant of recording all the curves assume a flat course because the aircraft is completely stopped and the test comes to the end.

## Chapter 5

# Conclusions, developments and applications

In conclusion, it is analyzed the rotor model developed in this thesis work from a general point of view. As can be seen from the mathematical treatment, the model is built to be as simple and efficient as possible. To realize it, several approximations are made. In fact, for the moment, as shown before, a 'almost-stationary' aerodynamics is used, the 'tip loss factor' and the Mach correction laws are still simplified. However, for each of these assumptions, the validity and the law impact on the results is verified with care. In addition, it is also possible to implement the contribution related to  $\dot{\Omega}$ , which as seen above, at the moment isn't considered yet in the mathematical treatment. Moreover, to optimize the model even more in the near future, it would be possible to insert some development, as the inclusion of more unstable aerodynamic terms, as well as a more elaborate 'tip loss factor' model, such as the one proposed by Glauert for instance. Moreover, through the right experimental data it would be possible to correct with Mach the coefficients of the profile adopted,  $C_{l_\alpha}$  and  $C_d$ , by means of a law no longer generic. A further development that it would be interesting to undertake, with the experimental data available, is the inclusion of complete aerodynamic polar for the aerodynamic profile, without having to resort to the approximations made by Hoerner anymore. What is more, with the increase of the computational capacities of the processors, in the future it should be possible to increase also the order of the polynomials that describe the twist and the distribution of the chord along the blade. Therefore, it would also be possible to increase the number of points in which each blade is divided for the numerical integration with the trapezoid method of aerodynamic loads, refining the results even more. Moreover, it is possible to insert the lag hinge, resolving this dynamic parallel to the flapping one, in order to obtain even more precise results and highlight phenomena such as 'ground resonance' that otherwise do not appear. In addition, it could also be interesting to introduce the aeroelastic effects of the blade, which in reality, in some circumstances, generate significant contributions to the local blade element and therefore to the loads generated by the rotor. These improvements could be done always provided that the real-time

requirement is met.

From a practical point of view, the processed rotor model returns satisfactory responses as shown in the validation chapter. In fact, the loads extracted in response to flight commands and external conditions are faithful to experimental ones in most cases. These positive results allowed us to start with confidence the flight simulator tests with the professional pilot. It shall also be remarked that, before these test could be performed on the simulator, a lot of time was spent on the integration between the new rotor model and the already existing XV-15 model, in order to match all the outputs desired by the latter and the inputs required by the new model.

The data extracted from the tests at the ZHAW University Simulator (RedSim) are the proof that this implementation phase is carried out with care. In fact, from these tests, where it was possible to perform the different maneuvers listed above in the 'XV-15 flight simulator test in helicopter mode' section, the simulation model of the aircraft revealed to be 'manageable' according to the pilot opinion. Naturally, the different failed hover attempts and the remarkable instability recorded along the pitch axis still leave much space for further investigation and analysis of the model's functionality. In addition, further tests are planned for the XV-15 in airplane mode with the associated maneuvers in this new condition. In fact, for reasons of time, the validation of the high advance flight rotor model (in airplane mode) is still rather lacking. In fact, at the moment, only the efficiencies of the propeller are verified with the variation of the advancing ratio as shown in Fig. 4.7. This is also due to the choice made together with all the collaborators to realize first of all a simulation model able to faithfully represent the helicopter and tilt-rotor in this mode and then extend it in the future, through a solid validation, also to the next mode. This last potential, together with the remarkable fidelity to real time and to experimental data, make this work different from many already present in literature. The peculiarity of the real time achieved by the model is due to the discretization method adopted in the resolution of the flapping dynamics (Tustin), which allowed us to make meaningful steps forward. For these reasons, it is believed that the model, represent an interesting contribution to research and flight simulation, and can therefore be adopted in numerous analyses of existing and future aircraft. In addition, the model is implemented with a view to make it easy and quick switching from one aircraft simulation to another. In fact, through a special interface, represented by a Matlab<sup>®</sup> script, it is possible to insert all the data belonging to the rotor (number of blade, extension, aerodynamic data...), after which, the model adapts all its calculations and therefore the results accordingly. This possibility of parameter's management allowed us to perform a large number of tests in a short time. Therefore, the model could also be interesting for those who need to realize a large number of test on their prototypes in a short period of time obtaining reliable results anyway.

# Bibliography

- [1] F. Barra. “Development of a tilt-rotor model for real-time flight simulation”. In: *Proc. 15th PEGASUS Student Conference (Glasgow, U.K., April 2019)*. 2019.
- [2] A. R. S. Bramwell, G. Done, and D. Balmford. *Bramwell’s Helicopter Dynamics*. Butterworth-Heinemann, 2001.
- [3] R. T. N. Chen, ed. *A Simplified Rotor System Mathematical Model for Piloted Flight Dynamics Simulation*. NASA TM-78575. 1979.
- [4] R. T. N. Chen, ed. *Effects of Primary Rotor Parameters on Flapping Dynamics*. NASA TP-1431. 1980.
- [5] D. A. Peters D. M. Pitt. “Theoretical prediction of dynamic-inflow derivatives”. In: Sixth European rotorcraft and powered lift aircraft forum. 1980.
- [6] S. W. Ferguson. “A Mathematical Model For Real Time Flight Simulation of a Tilt Rotor Aircraft”. In: NASA CR-166536. 2017.
- [7] S. W. Ferguson. “Development and Validation of a Simulation for a Generic Tilt-Rotor aircraft”. In: NASA CR-166537. 1988.
- [8] G. F. Franklin, J. D. Powell, and M. L. Workman. *Digital Control of Dynamic Systems*. ADDISON-WESLEY, 1998.
- [9] G. Guglieri, M. Porta, and A. Quinci. *Meccanica del volo dell’elicottero. Appunti delle lezioni*. Esculapio editore, 2018.
- [10] T. R. Norman H. Yeo. “Rotor Performance of a UH-60 Rotor System in the NASA Ames 80- by 120-Foot Wind Tunnel”. In: American Helicopter Society 58th Annual Forum. 2002.
- [11] R. K Haffle and M. A. Mních, eds. *Minimum-Complexity Simulation Math model*. NASA CR-177476. 1988.
- [12] F. D. Harris. “Hover Performance of Isolated Proprotors and Propellers—Experimental Data”. In: NASA CR-219486. 1988.
- [13] S.F. Hoerner. *Fluid Dynamic Lift*. S.F. Edts, 1975.
- [14] W. Johnson. *Helicopter Theory*. Dover Publications, Inc, 1980.
- [15] W. Johnson, B. H. Lau, and J. V. Bowles. “Calculated Performance, Stability, and Maneuverability of High-Speed Tilting-Prop-Rotor Aircraft”. In: NASA TM-88349. 1986.

- [16] K. M. Kleinhesselink. *"Stability and Control Modeling of Tiltrotor Aircraft"*, *MS Thesis*. University of Maryland, 2007.
- [17] P. Mazzoldi, M. Nigro, and C. Voci. *Fisica Volume I*. EdiSeS, 2001.
- [18] D. C. Maniaci S. Schmitz. "Analytical Method to Determine a Tip Loss Factor for Highly-Loaded Wind Turbines". In: SciTech. 2016.
- [19] M. D. Takahashi. "A Flight-Dynamic Helicopter Mathematical Model with a Single Flap-Lag-Torsion Main Rotor". In: NASA TM-102267. 1990.
- [20] J. Totah. "A Critical Assessment of UH-60 Main Rotor Blade Airfoil Data". In: NASA TM-103985. 1993.
- [21] T. W. Yeager, R. M. Wayne, and L. W. Wilbur. "Wind-Tunnel evaluation of an advance main-rotor blade design for a utility-class helicopter". In: NASA TM-89129. 1987.
- [22] F. Zöllner. *Leonardo Da Vinci: I. The Complete Paintings*. Mek, 2017.